Dissertation zur Erlangung des Doktorgrades
der Fakultät für Chemie und Pharmazie
der Ludwig-Maximilians-Universität München

Enhancing endosomal escape of siRNA through chemical electron transfer

Fengrong Zhang
aus Dingbian, Shaanxi, China

2024

Erklärung

Diese Dissertation wurde im Sinne von § 7 der Promotionsordnung vom 28. November 2011 von Herrn Prof. Dr. Ernst Wagner betreut.

Eidesstattliche Versicherung

Diese Dissertation wurde eigenständig und ohne unerlaubte Hilfe erarbeitet.

München, 31.05.2024

…….....

Fengrong Zhang

Dissertation eingereicht am 03.06.2024

1. Gutachter: **Prof. Dr. Ernst Wagner**

2. Gutachter: **Prof. Dr. Wolfgang Frieß**

Mündliche Prüfung am 04.07.2024

君子有九思：视思明，听思聪，色思温，貌思恭，言思忠，事思敬，疑思问，忿思难，见得思义

— 孔子

Table of Contents

1 Introduction

1.1 Lipid-based nanoparticles for RNAi therapy

RNA interference (RNAi) is a biological defense mechanism against exogenous gene invasion, discovered by pioneering studies in the 1990s [1,2]. The process involves the formation of an RNA-induced silencing complex, which targets and binds to message RNA, selectively downregulating gene expression at the post-transcriptional level (**Figure 1**) [3,4]. Around ten years later, it was first demonstrated that double-stranded RNA with 21 and 22 nucleotides could induce RNA silencing in mammalian cells without eliciting nonspecific interferon responses [5]. In 2002, researchers first demonstrated the feasibility of *in vivo* gene silencing facilitated by small interfering RNA (siRNA) [6]. Andrew Fire and Craig C. Mello were awarded the 2006 Nobel Prize in Physiology or Medicine for their excellent work on RNAi. The siRNAs were rapidly developed into interference tools for many disease treatments (*e.g.,* cancer [7,8] and genetic disorders [9,10]) in multiple biological areas, as they hold the ability to inhibit gene sequences through a base sequence alone efficiently.

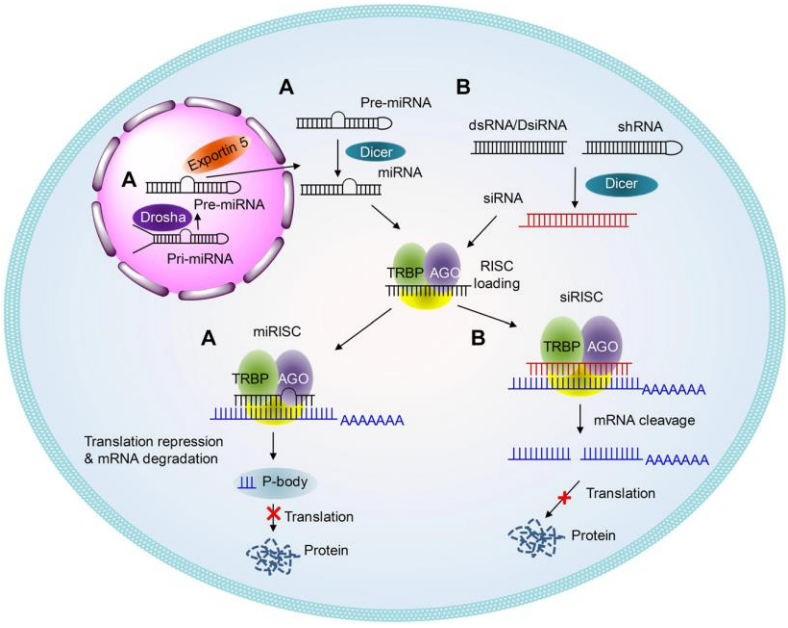

Figure 1. MicroRNA and siRNA working mechanisms. Reprinted with permission [3]. Copyright 2020, Springer Nature.

Despite achieving groundbreaking progress, the clinical application of siRNA therapeutics was initially hindered by various issues, including toxicity, off-target effects, inefficient delivery, and poor stability. The first clinical trial used unmodified siRNA, which induced severe immune-related toxicity and achieved unsatisfactory RNAi effects [11,12]. Naked, unmodified siRNAs at high concentrations can scarcely Toll-like receptor 3 or serine/threonine protein kinase capture, subsequently triggering systemic immune responses [13–15]. Additionally, base mismatching occasionally arises in siRNA sequences, causing binding to off-target RNAs. This interaction may lead to translational suppression or degradation of the off-target RNAs. Moreover, naked siRNAs are prone to rapid degradation by endogenous ribonucleases and phosphatases in the bloodstream after intravenous injection (with a half-life of around 15 min in serum) [16,17]. These issues can be addressed through chemical modification of the siRNA backbone and nucleotides, sequence selection of antisense strands, formulation of RNAi triggers, and so on [4]. Especially, the delivery of large, negatively charged siRNAs to mammalian cells is greatly enhanced through fusing with molecules capable of penetrating cell lipid bilayers or encapsulating siRNAs into lipid-based nanoparticles, including liposomes, lipid nanoparticles (LNPs), lipid−polymer hybrid nanoparticles, and lipid calcium phosphate nanoparticles.

Lipid-based nanoparticles, typically consist of three essential components: cationic/ionizable lipids, poly(ethylene glycol) (PEG) lipids, and helper lipids. Cationic lipids, such as 1,2-dioleoyl-3-trimethylammonium propane (DOTAP), can form stable lipoplexes with anionic nucleic acids by electrostatic interaction, neutralize the anionic nucleic acid molecules and facilitate endocytosis [18,19]. Ionizable lipids provide a pH-specific response, which makes them positively charged at endosomal pH, facilitating the escape of gene sequences from endosomes to the cytoplasm and promoting membrane destabilization [20]. Neutral helper lipids, including fusogenic lipids and cholesterol. For fusogenic lipids, such as 1,2-di-(9Z-octadecenoyl)-*sn*-glycero-3-phosphoethanolam and 1,2-dioctadecanoyl-*sn*-glycero-3-phosphocholine (DSPC), they are also widely used to promote endosomal membrane destabilization and aid in endosomal escape through membrane fusion [21]. Furthermore, phospholipids composition and properties influence lipid-based nanoparticles stability and permeability. By selecting specific phospholipids

with desired characteristics, researchers can tailor formulations to achieve optimal stability and drug release kinetics. As another important helper lipid, cholesterol can insert the phospholipid layer, modulate the fluidity of the lipid bilayer, prevent leakage of encapsulated substances, and improve the rigidity of liposomes [22,23].

After tremendous efforts, the first RNAi-based therapeutic medicine, Patisiran (Onpattro), was approved by the United States Food and Drug Administration (FDA) in 2018 to treat hereditary transthyretin amyloidosis. This approval represents a significant milestone in the advancement of siRNA therapeutics. Up to now, four more siRNA drugs have been approved for clinical application, including Givosiran (Givlaari), Lumasiran (Oxlumo), Inclisiran (Leqvio), and Vutrisiran (Amvutta) (**Table 1**).

Table 1. siRNA drugs approved by FDA as of 2023. Reprinted with permission [24]. Copyright 2023, Springer Nature.

Drug/ Trade name	Date of Approval	siRNA Carrier	Routes of administration	Indication and usage	Target organ	Target gene
Patisiran/ Onpattro	August 10, 2018	Lipid nanoparticles	intravenous	Adult patients with hereditary transthyretin mediated (hATTR) amyloidosis	Liver	transthyretin (TTR)
Givosiran/ Givlaari	November 20, 2019	GalNAc-conjugation	subcutaneous	Adult patients with acute hepatic porphyria (AHP)	Liver	aminolevulinate synthase 1 (ALAS1)
Lumasiran/ Oxlumo	November 23, 2020	GalNAc-conjugation	subcutaneous	Adult and pediatric patients with primary hyperoxaluria type 1 (PH1)	Liver	hydroxy acid oxidase 1 (HAO1)
Inclisiran/ Leqvio	December 21, 2021	GalNAc-conjugation	subcutaneous	Adult patients with heterozygous familial hypercholesterolemia or clinical atherosclerotic cardiovascular disease.	Liver	proprotein convertase subtilisin/kexin type 9 (PCSK9)
Vutrisiran/ amvuttra	June 13, 2022	GalNAc-conjugation	subcutaneous	Adult patients with hereditary transthyretin mediated (hATTR) amyloidosis	Liver	transthyretin (TTR)

1.1.1 Liposomes

In the mid-1960s, Bangham discovered that phospholipids with excellent biocompatibility could spontaneously form closed bilayer structures through hydration, later called liposomes [25]. Liposomes contain an aqueous cavity enclosed by one or more lipid bilayers; they are ideal candidates for drug delivery due to their ability to fuse with

mammalian cell membranes and encapsulate various drugs with varying hydrophilicity and hydrophobicity. Therefore, delivering large, negatively charged, hydrophilic siRNA with non-viral liposomes has become an increasingly attractive strategy for successful RNAi therapy. Liposomes exhibit several superiorities in intracellular delivery of siRNA: 1) effectively avoiding fast degradation of the loaded nucleic acid; 2) selectively accumulating in pathological tissues (such as tumor and thrombus) through enhanced permeability and retention effect and/or active targeting utilizing antibodies, aptamers, proteins, peptides, or ligands; 3) endowing high loading efficacy through pH gradient adjustment; 4) low immunogenicity phospholipids consist of hydrocarbon tail and phosphoric acid-based head, which can be degraded by phospholipase. Recent researches on liposome-based siRNA delivery systems mainly focus on exploring the influence of surface characterization, lipid composition, drug-to-lipid ratio, and excipients on intracellular delivery efficiency [21].

Liposomes offer a clinically adaptable platform for delivering siRNA to treat diseases requiring localized therapy, such as pachyonychia congenital, solid tumors, respiratory virus infections, and age-related macular degeneration. In 2009, Arbutus Biopharma Corporation carried out the first clinical trial of siRNA liposomes to evaluate liposome safety, tolerability, pharmacokinetics, and pharmacodynamics in subjects with high cholesterol [26]. Six years later, MD Anderson Cancer Center started the first study of the efficacy of liposomal siRNA-mediated treatment in phase I clinical trials of advanced or recurrent solid tumors. This study used 1,2-dioleoyl-*sn*-glycero-3-phosphatidylcholine-encapsulated siRNA targets ephrin type-A receptor 2. Corresponding results will be published in 2025.

1.1.2 LNPs

The first FDA-approved RNAi therapeutic was achieved with the help of LNPs. Unlike liposomes, typical LNPs only possess a single lipid outer layer encapsulating an electron-dense core, where ionizable lipids aggregate into inverted micelles surrounding the RNA molecules. Ionizable lipids containing secondary and/or tertiary amines are crucial in LNPs, providing pH-specific responsiveness. These lipids hold pKa values below 7, which

means that the structures have positive charges when protonated under acidic environments and can combine nucleic acids, while remaining neutral under physiologic conditions. Additionally, in lysosomal/endosomal acidic environments, protonated ionizable lipids facilitate the transfer of siRNA into the cytosol, effectively avoiding degradation. These characteristics underscore the significance of LNPs as candidates for RNA delivery.

Clinically, in addition to Patisiran, more than seven LNP siRNA drugs have entered trials. Specifically, ALN-PCS02, one siRNA-LNP drug developed by Alnylam Pharmaceuticals, targets the proprotein convertase subtilisin/kexin type 9 (PCSK9) gene, leading to the downregulation of corresponding protein levels [27]. The PCSK9 protein, primarily produced in the liver, is crucial in regulating low-density lipoprotein (LDL) cholesterol levels in the blood. Elevated PCSK9 levels are associated with increased LDL cholesterol levels, posing a risk factor for cardiovascular diseases such as atherosclerosis, heart attack, and stroke. Therefore, ALN-PCS02 helps lower LDL cholesterol levels in patients with hypercholesterolemia or familial hypercholesterolemia, potentially reducing their risk of cardiovascular complications. Additionally, siRNA LNP drugs ALN-VSP02, TKM-080301, and DCR-MYC also have entered clinical trials. They can specifically target cancer-related genes, including vascular endothelial growth factor, Eglin 5 (EG5), polo-like kinase 1, and MYC, affecting tumor proliferation, angiogenesis, and metastasis. Notably, they offer the advantages of avoiding adverse reactions associated with radiotherapy and chemotherapy while mitigating drug resistance. Moreover, siRNA LNPs are being developed for hepatic fibrosis and Idiopathic pulmonary fibrosis treatments.

1.1.3 Lipid−polymer hybrid nanoparticles

Combining with cationic polymers or oligomers offers another avenue for LNPs and liposomes, benefiting both systems. The lipid component provides stability, biocompatibility, and versatility. At the same time, the polymeric or oligomeric component enhances structural integrity, regulates siRNA release, and enables surface modification for targeted delivery. One of the most commonly used polymers is polyethyleneimine (PEI), employed in delivering nucleic acids into eukaryotic cells since 1995 [28]. It has the

advantages of chain flexibility and the high protonable ability of the tertiary amine group, enabling it to bind to negatively charged nucleic acid and facilitating high endosomal escape. Take an example, liposomes composed of 1,2-di-(9Z-octadecenoyl)-*sn*-glycero-3-phosphoethanolamine (DOPE)/dipalmitoylphosphatidylcholine/cholesterol were used to encapsulate PEI-complexed siRNA for ovarian tumor therapy [29].

In our group, a library of functional lipo-oligomers was established to complex nucleic acid *via* electrostatic interaction. These amino acids-based lipo-oligomers were synthesized using solid-phase supported peptide synthesis (SPPS) methodology. Lysine were adopted as branching sites, fatty acids as hydrophobic domains, and cysteines as crosslinking terminals. By integrating well-designed artificial amino acids, we synthesized linear, 3-armed, 4-armed, T-, i-, and U-shaped oligomers for gene delivery [30]. Moreover, introducing tyrosine tripeptides into the backbone improves the stability of lipopolyplexes and promotes the self-assembly of lipo-oligomer and siRNA through π–π interactions of the aromatic rings. The imidazole group within the histidine domain in the lipo-oligomer facilitates endosomal escape. Based on sequenced defined-lipo-oligomers, Luo *et al.* synthesized a cationizable lipo-oligomer backbone in a T-shape configuration coupled with atherosclerotic plaque-specific peptide-1 for targeting delivery [16]. Importantly, they adopted siEG5 (a member of the kinesin-5 family) to influence the assembly of the mitotic spindle apparatus, ultimately leading to mitotic arrest and tumor cell death.

1.1.4 Lipid-calcium-phosphate nanoparticles

Lipid-calcium-phosphate nanoparticles are a typical lipid-coated gene delivery platform, formed by coating one lipid bilayer on the surface of calcium phosphate nanoparticles [31,32]. Since the 1970s, calcium phosphate precipitates with good biocompatibility and biodegradability have been applied for *in vitro* transfection. The interaction between calcium ion and phosphate group within the gene sequence provides efficient nucleic acid encapsulation [33]. Furthermore, calcium phosphate exhibits an acid-responsive property, facilitating the transfer of nucleic acid from endosomes/lysosomes to the cytosol.

As a pioneer, Huang's lab developed the first generation of this core/shell structure to deliver siRNA [34]. This innovative structure consists of a sodium citrate-stabilized core

and a cationic liposome shell (1:1 molar ratio of DOTAP/cholesterol), which enhanced gene silencing efficacy of around 3–4 folds compared to liposome-polycation-siRNA formulation. In the second generation, researchers adopted anionic dioleoylphosphatydic acid as the inner leaflet lipid to avoid aggregation of the calcium phosphate core. Furthermore, compared with the first generation, the diameter of the optimized formulation is significantly reduced (around 25–30 nm), thereby modulating its *in vivo* distribution. For both generations, the Ca/P molar ratio is a crucial factor in controlling size, zeta potential, dispersion, and siRNA loading efficiency [35].

1.2 Major challenges of lipid-based nanoparticles for RNAi therapy

Over the past three decades, chemists, biologists, and material scientists have devoted extensive efforts to develop novel lipid-based formulations for siRNA delivery, with the aim of better understanding the chemical and biophysical properties of vehicles to enable effective therapy in clinical trials. Generally, the research directions address the following limitations in lipid-based gene delivery systems, including low endosomal escape efficacy, poor specificity, potential toxicity, etc.

Endosomal escape is a major biological barrier in realizing efficient gene silencing by non-viral lipid-based nanosystems [36]. Normally, nanoparticles are internalized *via* endocytosis; as they progress through the endosomal pathway, the environment gradually becomes acidic (pH 6.5 for early endosomes) as they develop into late endosomes (pH 4–5). Biological therapeutics will be degraded by hydrolases if they cannot escape from late endosomes [37]. Studies adopting intracellular imaging proved that only 1–2% of lipid-based vehicles could escape from endosomes [38].

In addition to the endosomal escape issue, biosafety problems caused by poor specificity and targeting also hinder applications of lipid-based systems. Mostly, they tend to accumulate in the liver and kidneys, taking function in metabolic and immune organs (**Figure 2**) [39]. During blood circulation, serum apolipoprotein E usually adsorbs on the surface of nanoparticles, which results in uptake by liver hepatocytes *via* LDL receptors

[40]. Moreover, the special hepatic anatomy, like hepatic sinusoids, can promote the extravasation of nanoparticles [41].

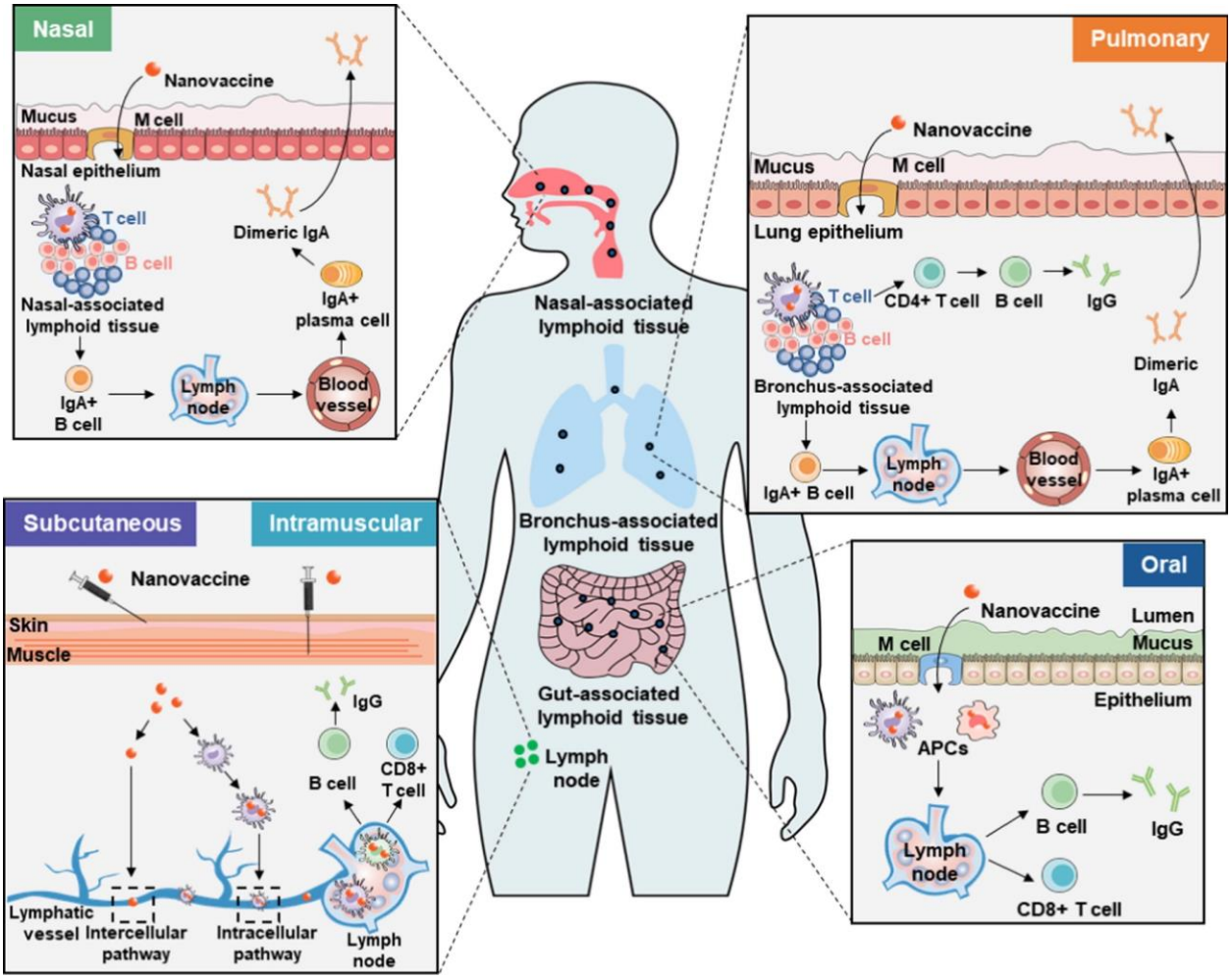

Figure 2. *In vivo* fates of nanovaccines administered by various routes. Reprinted with permission [39]. Copyright 2022, Elsevier.

Besides non-targeted accumulation, the potential toxicity and intrinsic immunogenicity of the carriers and RNA are also severe. After first injection, the body can generate anti-PEG antibodies, accelerating the blood clearance of PEGylated lipid nanocarriers upon subsequent injections [42]. Moreover, hypersensitivity reaction is another immune response to lipid-based nanoparticles, known as complement activation-related pseudoallergy. RNA sequence may also have immunogenicity by stimulating immune responses *via* Toll-like receptor and/or retinoic acid-inducible gene I sensing mechanisms

[43,44]. Stimulating the production of interleukin-1 receptor-associated cytokines through alternative sensing pathways, which can also induce reactogenicity [45,46].

1.3 Mechanisms for endosomal escape

To explain the endosomal escape of lipid-based nanoparticles, researchers have proposed two main mechanisms: non-lamellar phase change and proton sponge effect. For both of them, the membrane undergoes initial destabilization followed by membrane pore formulation or membrane fusion, the specific behavior dependent on the physiochemical characteristics of the formulation. Ultimately, these lead to the leakage of nucleic acids or nanoparticles from the endosomal compartment to the cytosol.

The non-lamellar phase change mechanism is induced by the membrane fusion as well as the phospholipid flip-flop. Ionizable lipids provide endosomal pH-specific responsiveness, exhibiting positive charges in endosomal acidic conditions. The endosomal membrane consists of negatively charged phospholipids, which can combine with cationic or ionizable lipids. Consequently, anionic phospholipids from the cytosolic leaflet can flip to the intraluminal side of the endosome [47,48]. Additionally, when RNA sequences are delivered *via* enveloped nanoparticles, such as liposomes and LNPs, the gene sequence escapes through fusion with the endosomal membrane. This fusion process leads to the formulation of charge-neutralized ion pairs, inducing non-lamellar phase changes and subsequent membrane destabilization [49]. For ionizable lipids, pH-specific endosomal action avoids direct damage to the cytosolic membrane, thus minimizing cytotoxic side effects. Cecilia et al. regulated the topology of lipid formulations to reduce the energetic cost of fusion and fusion–pore formation, thereby enhancing the efficiency of RNA translocation into the cytosol. They demonstrated that LNPs with cuboplex nanostructures were more effective than lipoplexes in endosomal escape [50].

Aside from pore formation, endosomal escape can also occur through the rupture or bursting of the endosomal membrane, also known as the proton sponge effect (**Figure 3**) [36,51]. This mechanism replies on V-ATPase-driven proton transport, thereby generating a proton gradient; protonated lipids increase the accumulation of protons within the

endosome by V-ATPase, thereby triggering the influx of chloride and water, finally inducing a high increase in osmotic pressure and swelling of endosomes. Building on this hypothesis, ionizable lipids, lipoids, and oligomers with a pKa of around 6 have been well explored to increase their endosomal buffer capacity. Furthermore, integrating amino lipids with varying pKa values allows for more sensitive adjustment of properties and delivery effectiveness. For example, Michael J. Hope and cooperators proved that combinations of three amino lipids generated different LNP formulations with average surface pKa values ranging from 5.64 to 6.93 [52]. These combined formulations showed superior gene silencing compared to single lipid-formulated liposomes.

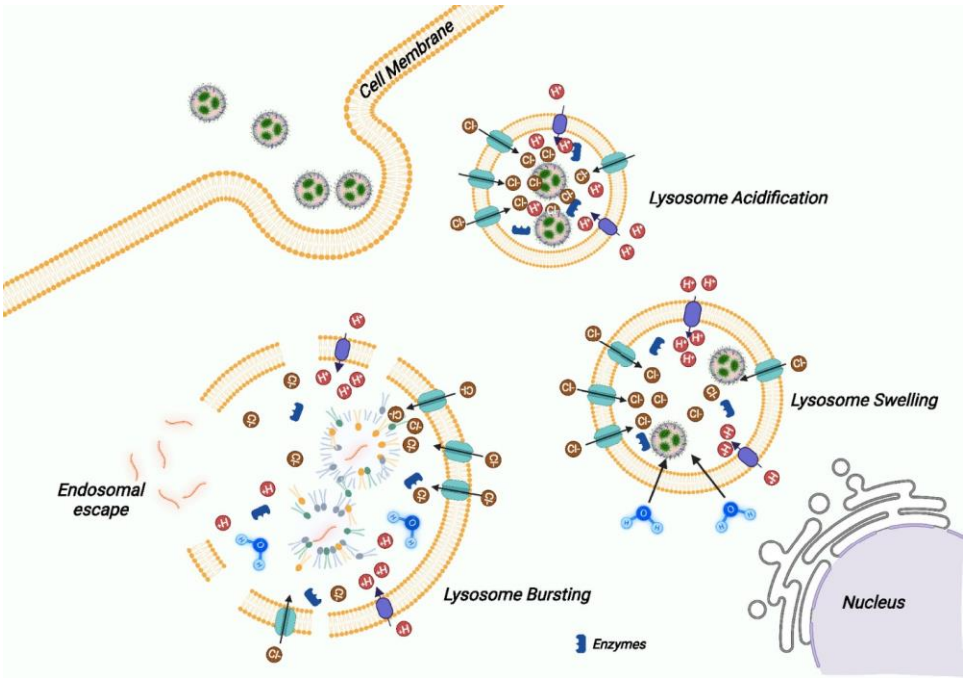

Figure 3. Schematic representation of the proton sponge effect. Reprinted with permission [36]. Copyright 2024, National Academy of Sciences.

1.4 Strategies for improving endosomal escape through external stimulus

To enhance nucleic acid cytoplasmic transfer, researchers have adopted numerous strategies. One main direction involves encapsulating stimulus-sensitive components into

lipid-based vesicles that could respond to external triggers such as photons, ultrasound, electricity, magnetism, etc.

1.4.1 Photochemical internalization

The utilization of photochemical stimulus to achieve biomacromolecule translocation is based on the photodynamic effect. For traditional organic photosensitizers (PSs), under the irradiation of a specific wavelength of light, PSs are excited by the energy from the light, changing the electronic state from the ground singlet state (S_0) to the first excited state (S_1). Subsequently, undergoing intersystem crossing, an excited triplet state (T_1) with a longer lifespan is formed. Then, two types of photochemical reactions can occur [53–56]. In Type I reaction, an excited sensitizer molecule transfers one electron or a hydrogen atom to an adjacent sensitizer, formulating ion radicals. These radicals then react with molecules, producing superoxide anion, hydrogen peroxide (H_2O_2), and hydroxyl radical. In Type II reaction, the energy from T_1 directly transfers to oxygen, exciting it into singlet oxygen ($^1O_2$). For most metal-based PSs, reactive oxygen species (ROS) can be produced on the plasmonic surface *via* high-energy 'hot electrons', which are also excited by the input light energy [56–58]. These hot electrons, holding a triplet-excited state, can also transfer energy to molecular oxygen.

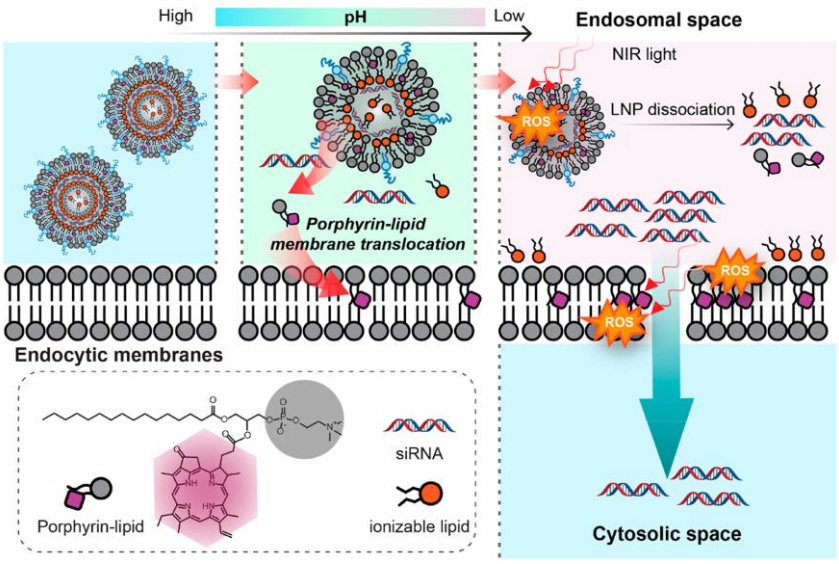

Figure 4. Schematic Illustration of porphyrin-lipids mediated light-activated siRNA endosomal release approach. Reprinted with permission [63]. Copyright 2023, American Chemical Society.

The generated ROS further induces lipid peroxidation of the endosomal membrane and cargos; this oxidation destabilizes the endosomal membrane and releases trapped macromolecules [59,60]. In 2008, as pioneers, de Bruin et al. used disulphonated *meso*-tetraphenylporphine to investigate photoinduced DNA endosomal release, demonstrating that photosensitizer-mediated release of polyplexes could be visualized in real-time for single endosomes [61]. Zheng's lab synthesized a series of porphyrin-lipids [32,62–64] and incorporated them into the FDA-approved Onpattro formulation to achieve light-activated siRNA endosomal release. Quantitative imaging analysis revealed that porphyrin-LNPs significantly downregulated the required therapeutic siRNA dose (around 4-fold) for silencing the target mRNA (**Figure 4**) [63].

1.4.2 Photothermal internalization

The photothermal effect refers to photothermal transduction agents absorbing photons' energy and converting it into heat, thereby increasing the temperature of the surrounding environment. In the case of organic agents, electrons in the S_1 state can return to the ground state through two pathways: radiative relaxation, which produces fluorescence, and non-radiative relaxation, which generates heat energy [65–67]. Inorganic nanoagents include noble metal nanoparticles [68,69], transition metal sulfides [70,71], carbon-based nanomaterials [72,73], and other two-dimensional nanoparticles [74,75], exhibit distinct mechanisms for generating heat energy. Taking noble metal nanoparticles as an example, free electrons from the conduction band can be polarized under visible light or near-infrared light irradiation. When the frequency of the optical absorption resonates with the oscillation frequency of the electron cloud, these nanoparticles absorb photons, leading to the redistribution of the electron cloud and generation of localized surface plasmon resonance, which further produces heat energy [76,77].

A mild photothermal effect with a local temperature below 43 ^{o}C increases membrane fluidity, thereby facilitating nanoparticle endocytosis and endosomal transfer. In addition, the higher temperature provides more opportunities for vehicles to release cargo (**Figure 5**) [78]. Most recently, Ni et al. introduced second near-infrared (NIR-II) LNPs, containing

pH-activatable NIR-II dye-conjugated lipid, enabling stimulus-responsive photothermal-assisted endosomal escape delivery [79].

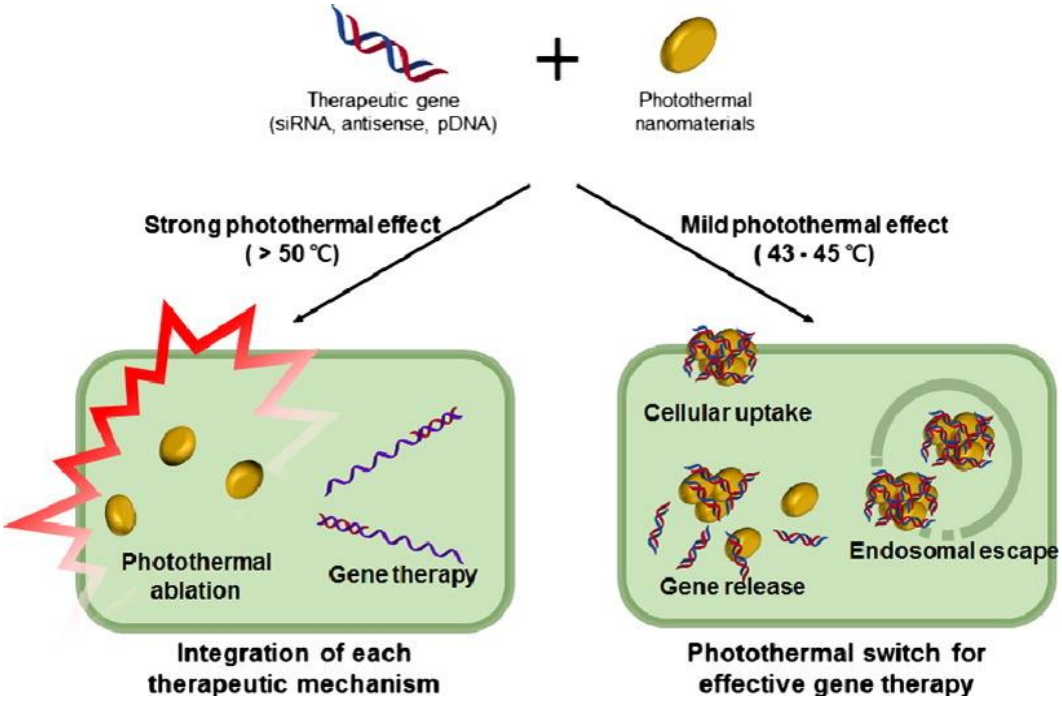

Figure 5. Schematic Illustration of the combination gene therapy and photothermal therapy. Reprinted with permission [78]. Copyright 2016, Elsevier.

1.4.3 Sonochemical internalization

Similar to photodynamic internalization, sonochemical-enhanced endosomal escape also relies on ROS generation. The combination of sonosensitizers and high-frequency ultrasound (1–10 MHz) enhances the therapeutic efficacy of gene sequences by facilitating their internalization while accompanying negligible side effects. There are two dominant mechanisms for the sonochemical effect: sonoluminescence as well as cavitation [80]. Sonoluminescence refers to the transfer of luminous energy through the electronic excitation of a sensitizer by ultrasound. Cavitation is a phenomenon where bubbles in a medium rapidly expand under ultrasound irradiation and then collapse rapidly, producing shock waves, micro-jet, high temperature, and high pressure, leading to the decomposition of water into ROS.

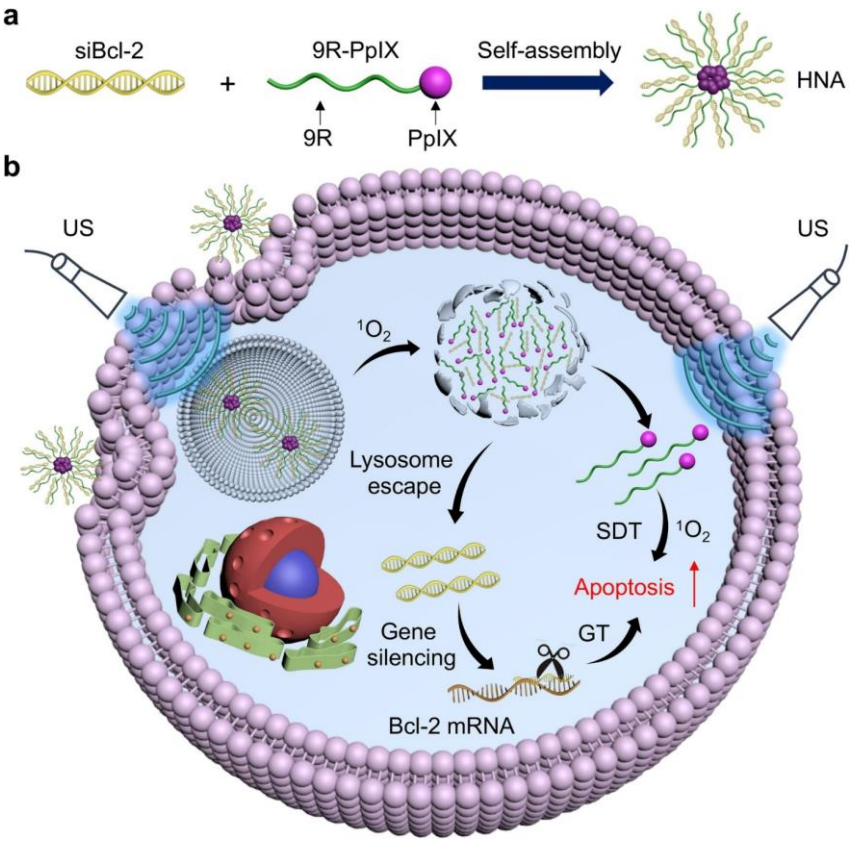

Figure 6. Schematic Illustration of the sono-controllable hybrid design. Reprinted with permission [84]. Copyright 2023, Elsevier.

To date, organic porphyrins and relative derivatives (such as hematoporphyrin, protoporphyrin IX, and hematoporphyrin monomethyl ether) are still the most widely used sonosensitizers in clinical practice. They hold the advantages of a large π-electron conjugated system, broad-ranging optoelectronic properties, and catalytic performance [81–83]. Li and colleagues reported a sono-controllable hybrid for ultrasound-inducible siRNA cytosolic delivery (**Figure 6**) [84]. Nona-arginine modified with protoporphyrin IX was adopted as a sonosensitizer, which electrostatic self-assembled with siRNA sequence. Under ultrasound irradiation, the colocalization ratios between siRNA and lysosomes downregulated from 91 % to 33 %, and the gene silencing efficacy increased from 46 % to 68 % with a hybrid concentration of 300 nM. In addition, nuclear factor erythroid 2-related factor 2 (Nrf2) is one of the crucial regulators of oxidative pressure, which mediates the classical deoxidation signaling pathway in maintaining normal redox levels and resists sonochemical internalization by continually consuming ROS [55,85,86].

Therefore, researchers introduced Nrf2-siRNA to inhibit ROS detoxification. Wan et al. used NIR fluorescence dye IR780 to couple nuclear-targeting peptide, further loaded Nrf2-siRNA, the siRNA was mainly removed to the cytoplasm after 4 h incubation [87]. Moreover, compared with the free sonosensitizer group, siNrf2 complexed IR780 and peptide group with ultrasonic irradiation significantly improved the intracellular ROS level.

1.4.4 Electroporation-mediated internalization

Electroporation is a well-explored strategy for enhancing cellular uptake of DNA, RNA, and protein *in vitro* and *in vivo*. With the help of a pulsed electric field, the permeability of the lipid membrane is transiently increased, and hydrophilic pores are formed in the plasma membrane; then macromolecules are transferred into the cytosol within a short time [88–90]. Studies have indicated that the electrotransfection efficiency also depends on endocytosis. Yuan's group used pharmacological inhibitors (chlorpromazine and dynasore) of endocytosis to treat cells before applying the pulsed electric field, proving that the inhibitors significantly reduced the electrotransfection efficiency [91].

Clinically, researchers used electroporation to deliver the interleukin-12 gene to patients with metastatic melanoma. 24 patients received a phase I trial at 7 dose levels, 2 of them had nonelectroporated distant lesions showed complete regression of all metastases, 8 patients showed disease stabilization or partial response. This study demonstrated that electrotransfection was safe, effective, reproducible, and treatable for humans [92]. Additionally, Jensen et al. optimized the delivery of siRNA into primary bovine monocyte-derived macrophages using electroporation, which achieved comparable levels of target gene silencing as transient transfection and exhibited negligible type I interferon response [93].

1.4.5 Magnetic field-assisted internalization

Superparamagnetic nanoparticles are important gene delivery systems that can be precisely guided to target regions with the help of external magnetic fields. When exposed to alternating magnetic fields, these nanoparticles undergo magnetic relaxations, finally generating hyperthermia [94–96]. It has been proved that superparamagnetic iron oxide

nanoparticles can generate Brownian motion through adjusting particle size under an alternating magnetic field with specific frequencies [97]. Both hyperthermia and Brownian motion are beneficial for gene sequence escaping from endosomes before degradation in lysosomes. Meanwhile, introducing the magnetic properties into the gene delivery system can endow multifunctionality to formulations, such as magnetic resonance imaging and magnetic hyperthermia treatment.

Qiao and colleagues synthesized magnetic silica nanoparticles with core-shell structure for siRNA delivery, these carriers were fabricated though coating dendrimer-like mesoporous silica layer on the surface of superparamagnetic nanocrystal clusters. The loading amount of siRNA of this nanocomposite carrier was 2 wt% and successfully delivered into the cytoplasm of cancer cells [96]. Most recently, caffeic acid–magnetic calcium phosphate nanoparticles were prepared as carriers for human epidermal growth factor type 2 gene siRNA, showing the capability to facilitate endosomal escape by upregulating osmotic pressure [94].

1.5 Aim of this thesis

RNAi promises excellent efficacy and specificity in silencing target mRNA, which exhibits potential for tumor therapy. However, the endosomal escape of siRNA remains a major limitation for successful RNAi therapy. Hence, novel strategies for improving the cytoplasmic transfer of therapeutics have to be explored to enhance therapeutic efficiency and downregulate nanovehicle dosage. Light free-photochemical internalization, based on ROS generation in the presence of sufficient H_2O_2, provides an alternative opportunity for endosomal escape. Compared with traditional internalization mediated by external energy (*e.g.*, photochemical, photothermal, sonochemical, electroporation, and magnetic internalization), chemical endosomal escape has a higher selectivity and gets rid of external triggers. Such internalization is suitable for deep tissues that overexpress H_2O_2. This process prevents non-specific gene silencing in normal regions to some extent, because the chemical reaction is initialed in the microenvironment of the cancer cells.

The chemiluminescence resonance energy transfer (CRET) system is a potential candidate for chemical internalization, which is achieved by nonradiative energy transfer between chemiluminescence donors and PSs and has been adopted for light-free chemodynamic therapy. Similar to conventional photodynamic therapy, excited electrons transfer to a higher-energy orbital of the PSs, undergo intersystem crossing, excite oxygen to generate $^1O_2$ *via* the type II photochemical reaction. The distance between the donor and the photosensitizer should be within 10 nm. Some PSs, such as metalloporphyrins and metal nanoparticles are excellent acceptors for CRET, exhibiting unique superiorities of broad spectrum, high stability, and minimal side effects.

The first aim of the thesis was to develop a chemical electron transfer (CET)-based self-activatable lipopolyplex for producing $^1O_2$ in endosomes, thereby enhancing siRNA delivery. The positively charged lipopolyplex could encapsulate bis(2,4,6-trichlorophenyl) oxalate (TCPO) in the hydrophobic section, gold nanoparticles (GNs) and siRNA in the hydrophilic core. When the lipopolyplexes gather in the H_2O_2-rich microenvironment, the acceptors (GNs) could be specifically self-activated by the transferred chemical energy from an energy-rich intermediate (1,2-dioxetanedione), catalyzing molecular oxygen to produce $^1O_2$. Enhanced endosomal membrane damage had to be verified using a cytosolic fluorescent galectin reporter, and siRNA targeting EG5 mRNA (also known as KSP or Kif11, one important participant in the process of centrosome separation) had to be cooperated into the system to initiate the tumor cellular apoptosis program.

The second part of the thesis aimed at incorporating CET into siRNA LNPs to achieve the dual effects: endosomal escape of tumor-protective gene siRNA and aggravation of ROS-triggered tumor cell killing. For this purpose, Nrf2 siRNA had to be introduced to extend the lifetime of ROS by silencing the oxidative stress mRNA. In the LNPs-loaded CET and siRNA system, the CET donor and acceptor had to be simultaneously encapsulated inside to ensure sufficient energy transfer. Moreover, an ionizable lipopeptide had to be selected by optimization for siRNA encapsulation in LNP and pH-induced endosomal escape, with the ultimate goal of accomplishing a higher therapeutic effect while reducing the required siRNA dose and amount of lipids, avoiding possible side effects caused by the lipids.

2 Materials and Methods

2.1 Materials

TCPO, hemin, sodium citrate, 9,10-diphenanthraquinone (DPA), chloroauric acid, agarose gel, Roswell Park Memorial Institute-1640 medium (RPMI-1640), Dulbecco's modified Eagle's medium (DMEM), antibiotics, fetal bovine serum (FBS), methyl thiazolyl tetrazolium (MTT), 4',6-diamidino-2-phenylindole (DAPI), paraformaldehyde (PFA), rhodamine phalloidin, nystatin, sucrose, methyl-β-cyclodextrin (MβCD), and amiloride were sourced from Sigma-Aldrich (Munich, Germany). Fmoc-Ala-Wang resin and Fmoc-a-amino acids were obtained from Iris Biotech (Marktredwitz, Germany). Cholesterol, DSPC, DOPE, DOTAP, and 1,2-dimyristoyl-rac-glycero-3-methoxypolyethylene glycol-2000 (PEG-DMG) were purchased from Avanti Polar Lipids (Birmingham, USA). *N*-2-hydroxyethylpiperazine-*N'*-2-ethanesulfonic acid (HEPES) was bought from Biomol (Hamburg, Germany). GelRed and peqGOLD Total RNA kits were obtained from VWR (Darmstadt, Germany). siRNA duplexes were obtained from Axolabs GmbH (Kulmbach, Germany). Enhanced green fluorescent protein (eGFP) -targeting siRNA (siGFP) (sense: 5'-AuAucAuGGccGAcAAGcAdTsdT-3'; antisense: 5'-UGCUUGUCGGCcAUGAuAUdTsdT-3') for silencing of eGFPLuc; EG5-targeting siRNA (siEG5) (sense: 5'-ucGAGAAucuAAAcuAAcudTsdT-3'; antisense: 5'-AGUuAGUUuAGAUUCUCGAdTsdT-3') for silencing EG5 motor protein; control siRNA (siCtrl) (sense: 5'-AuGuAuuGGccuGuAuuAGdTsdT-3'; antisense: 5'-CuAAuAcAGGCcAAuAcAUdTsdT-3'); Cy5-labeled siRNA (Cy5-siAHA1) (sense: 5'-(Cy5)(NHC6)GGAuGAAGuGGAGAuuAGudTsdT-3'; antisense: 5'-ACuAAUCUCcACUUcAUCCdTsdT-3'); small letters: 2'-methoxy-RNA; s: phosphorothioate. Cell lysis and luciferase assay kit were purchased from Promega (Mannheim, Germany). $^1O_2$ sensor green dye was obtained from Molecular Probes (Eugene, USA). Quant-iTTM RiboGreen® RNA assay kit, 5,5,6',6'-tetrachloro-1,1',3,3'-tetraethyl-imidacarbocyanine (JC-1), LysoTracker Green DND-26, and CellROX Green reagent were purchased from Invitrogen (Carlsbad, USA). Dialysis membrane (3.5 kDa molecular weight cut-off) was obtained from Spectrum Labs (Los Angeles, USA). The

luciferase assay kit was obtained from Promega (Madison, USA). Annexin V-fluorescein isothiocyanate (FITC)/propidium iodide (PI) apoptosis kit was obtained from R&D Systems (Minneapolis, USA). qScript^{TM} cDNA SuperMix was purchased from Quantabio (Beverly, USA). Reverse transcription-quantitative real-time PCR (RT-qPCR)-Mastermix was sourced from Thermo Fisher Scientific (Waltham, USA).

2.2 Methods

2.2.1 Synthesis of GNs

GNs were prepared *via* an UV-assisted citrate method according to the earlier research with slight modification [98]. In brief, 5 mL of sodium citrate solution (12 mM) was added into 5 mL of precooled $HAuCl_4$ solution (4 mM), and then gently stirred at 0 °C for 2 min. A 400 W UV lamp (365 nm, 80 mW cm^{-2}) was then used to irradiate the mixture for one hour under stirring in an ice bath. The color of the solution was changed from slight yellow to reddish after the reaction. Afterwards, one standard regenerated cellulose dialysis membrane (3.5 kDa MWCO) was chosen to dialyze the resultant GNs against 5 L of water at 4 ^{o}C for 4 h, removing the excess $HAuCl_4$ as well as reducing agent.

2.2.2 Preparation of CET-based lipopolyplexes

For the preparation of four-armed oligomer 573, solid-phase assisted peptide chemistry was adopted according to Lächelt *et al* [99]. There are three key parts in the synthesis process: loading Fmoc-Lys(Fmoc)-OH to the Fmoc-Ala-Wang resin, coupling Fmoc-a-amino acids as well as Fmoc-Stp to extend the sequence, and cleaving oligomer from the resin. Fmoc-Ala-Wang resin with the loading efficacy of 0.35 mmol g^{-1} was adopted.

The CET based lipopolyplex was formulated using a solvent-exchange deposition strategy. In detail, cholesterol, DOPE, PEG-DMG, DOTAP, and 4-armed oligomer with different molar ratios were dissolved in ethanol, and the resulting mixture was mixed with TCPO dimethyl sulfoxide (DMSO) solution. In the meanwhile, siRNA and GNs were prepared in 60 µL sodium citrate buffer (10 mM, pH 4). The aqueous solution was quickly pipetted into the organic phase at a ratio of 3/1 (vol./vol.), and then incubated the lipopolyplex for 20

min at room temperature. The whole process was protected from light. Next, standard regenerated cellulose dialysis membranes (3.5 kDa MWCO) were chosen to dialyze the resultant lipopolyplex against 5 L of HEPES buffer at 4 °C for 4 h.

2.2.3 Preparation of CET-based LNPs

LNPs were formulated using a rapid-mixing method [100]. First, cholesterol (5 mg mL^{-1}), DSPC (2.5 mg mL^{-1}), PEG-DMG (1 mg mL^{-1}), and ionizable lipopeptide (10 mg mL^{-1}) stock solutions were prepared in ethanol. The amounts of ionizable lipopeptide were calculated according to siRNA dose, hemin dose, and N/P or N/(P+C) ratios. The amounts of other lipids were determined by molar ratio (Table 2). The lipids ethanol solutions were mixed, and the mixture was then combined with a DMSO (v/v, 1/1) containing TCPO (9 mg mL^{-1}) and hemin (1 mg mL^{-1}). The total volume was 30 µL. After that, a siRNA aqueous solution (dissolved in citrate buffer, 10 mM, pH 4) was rapidly mixed with the organic solution at a volume ratio 3:1 and incubated at room temperature for 20 min. The resultant LNP solution was dialyzed in HEPES buffer (20 mM, pH 7.4) at 4 °C for 4 h to remove organic solvents. The final volume was 200 µL. The ionizable lipopeptide *tetra-oleoyl tri-lysino succinoyl tetraethylene pentamine* (TOTL-Stp) with U-shape topology was synthesized by Tobias Burghardt (PhD student at Pharmaceutical Biotechnology LMU München) according to protocols described in previous publications [30,101,102].

2.2.4 ^{1}H-nuclear magnetic resonance (NMR) spectroscopy

^{1}H-NMR spectroscopy of 4-armed oligomer was carried out using a JEOL JNMR-GX 400 at 400 MHz (JEOL, Tokyo, Japan). Chemical shifts were reported in ppm and D_2O as the solvent was referred internal standard (D_2O at 4.79). Spectrum was analyzed using MestReNova (Mestrelab Research).

2.2.5 Transmission electron microscopy (TEM)

A JEM 1011 transmission electron microscope (TEM, JEOL, Tokyo, Japan) at 80 kV acceleration voltage was used to analyze the morphology of LNPs. First, carbon-coated TEM copper grids (300 mesh, 3.0 mm OD; Ted Pella, Redding, USA) underwent hydrophilization using mild argon plasma (420 V, 1 min). After that, 10 µl sample droplets

were dropped on the grids and incubated for 3 min. Following incubation, the solution was removed, and the grid was washed once before being stained with 10 µl of 1% uranyl acetate solution for 5 seconds. Finally, the excess staining solution was removed, and the grid was allowed to air dry for 20 min before being measured by TEM.

2.2.6 Inductively coupled plasma mass spectrometry

The concentration of GNs was determined by inductively coupled plasma mass spectrometry (Agilent Technologies, Santa Clara, USA). Briefly, a concentrated stock solution of the sample (200 µL) was added to scintillation vials. Then, 0.8 mL of aqua regia was added to each vial to dissolve all GNs. Finally, deionized water was added to dilute the samples. The Au concentrations of the prepared solutions were then measured using inductively coupled plasma mass spectrometry.

2.2.7 Particle size and zeta potential

LNPs or lipopolyplexes containing 1 µg of siRNA in a total volume of 200 µL were diluted 1:5 with 20 mM HEPES buffer (pH 7.4) before measurement using a folded capillary cell (DTS1070). For hydrodynamic size and polydispersity index (PDI), and zeta potential of particles were tested in a folded capillary cell (DTS 1070) with a Zetasizer Nano ZS (Malvern Instruments, UK). The refractive index of the solvent was 1.330 and the viscosity was 0.8872 mPa·s. The measurements were run three times (15 sub-runs). Zeta potential was measured with a flexible attenuator at a 90° angle. Samples were measured three times (12-15 sub runs). Afterwards, the data was analyzed using Zetasizer software (version 7.13).

2.2.8 DPA degradation assay

For TCPO and GNs system, 1 mL GNs aqueous solution (100 µg mL^{-1}) was mixed with 1 mL TCPO solution (20 mM), 1 mL H_2O_2 solution at different concentrations (0, 0.3125, 0.625, 1.25, 2.5, 5, 10 mM), and 100 µL DPA solution (1 mg mL^{-1}), followed by analysis with an UV–vis–NIR spectrophotometer (Agilent Technologies, Santa Clara, USA) at different time points.

For TCPO and hemin system, a mixture was prepared by combining 12 μL of a 1 mg mL^{-1} DPA solution with 25 μL of a hemin solution (25 μg mL^{-1}), 15 μL of a TCPO solution (9 mg mL^{-1}), 300 μL of H_2O_2 with various concentrations (1.56, 3.13, 6.25, 13.3, and 26.6 mM), and 448 μL of H_2O. Subsequently, the mixture was measured using a UV–vis spectrophotometer (Agilent Technologies, Santa Clara, USA) at different incubation times (2 min, 30 min, 1 h, and 2h). For the LNPs-related ROS generation test, a reaction solution was similarly prepared by mixing 12 μL of a 1 mg mL^{-1} DPA solution with 25 μL of a Hemin+TCPO+siRNA@Lipid HEPES buffer, 300 μL of H_2O_2 (13.3 mM), and 463 μL of H_2O. or Hemin+TCPO+siRNA@Lipid, different TCPO/hemin molar ratios (20, 40, 60, 80, 100, 150, and 200) were prepared. The N/P ratio was 3, the siRNA amount was 1 μg, and the TCPO amount was 80 μg. The molar ratio of different lipids was 50/38.5/10/1.5 (ionizable lipopeptide/cholesterol/phospholipid/DMG-PEG). Finally, the absorption of the solution was analyzed after incubation for 2 min and 2 h, respectively.

2.2.9 siRNA binding assay

A 2.5% (w/w) agarose gel containing GelRed in TBE buffer was prepared for siRNA binding assay. Agarose was dissolved in TBE buffer by boiling and cooling to approximately 50 °C. GelRed (1/1000, v/v) was added to the solution. The TBE buffer containing 10.8 g of Trizma®base, 5.5 g of boric acid, 0.75 g of disodium ethylenediaminetetraacetic acid, and 1 L of H_2O. The lipopolyplex coated with different amounts of lipid (1.8, 3.6, and 5.4 mM) was incubated with 90% FBS at 37 °C for 4 h, 24 h, and 48 h, respectively. Then the lipopolyplex was added into the well after mixing with 4 μL loading buffer. Electrophoresis was run at 120 V for 40 min, afterwards, the gel was photographed by Dark Hood DH-40 UV transilluminator (Biostep, Burkhardtsdorf, Germany). For LNPs, the formulations (containing 100 ng siRNA in 20 μl HEPES buffer) with different N/P ratios were loaded into wells on the pre-prepared wells after adding 4 μL loading buffer.

2.2.10 Hemin and TCPO loading determination

The hemin DMSO solutions with different concentrations (0.94, 1.88, 3.75, 7.5, 15, and 30 μg mL^{-1}) were measured by UV–vis–NIR spectrophotometer. For TCPO, similar

measurements were done. Curve fitting for hemin and TCPO absorption were obtained by the absorbance and concentrations. The LNP formulations with different N/(C+P) were dissolved in DMSO, and the absorptions at 403 nm and 253 nm were measured. The loading efficiencies of hemin and TCPO in LNPs with N/P ratios were obtained according to the absorptions.

2.2.11 Cell culture

Human cervix carcinoma cells KB, human embryonic kidney cells HEK293, human prostate cancer cells DU145, mouse hippocampal neuronal HT22 cells, and murine neuroblastoma cells N2a were obtained from DSMZ (German Collection of Microorganisms and Cell Cultures, Braunschweig, Germany). KB cells, DU145 cells, N2a cells stably transfected with the eGFP-luciferase gene, KB/eGFPLuc, DU145/eGFPLuc, N2a/eGFPLuc, were used in gene silencing efficiency assay [102,103]. HeLa cells stably expressing Gal8-mRuby3 fusion protein was chosen to demonstrate endosomal escape, this work was performed by Dr. Yi Lin (former PhD student at Pharmaceutical Biotechnology, LMU München) [104,105]. The PB-CAG-mRuby3-Gal8-P2A-Zeo plasmid was a gift from Jordan Green's lab (Addgene plasmid no. 150815; http://n2t.net/addgene:150815; RRID: Addgene_150815). KB, KB/eGFPLuc, HeLa-Gal8-mRuby3, N2a, and N2a/eGFPLuc were cultured in DMEM at 37 ^{o}C in a 5% CO_2 atomsphere. HEK293 and HT22 cells were maintained in high-glucose DMEM. DU145 and DU145/eGFPLuc were cultured in RPMI-1640. The DMEM, high-glucose DMEM, RPMI-1640 medium were supplemented with 10 % FBS, 100 U mL^{-1} penicillin, and 100 µg mL^{-1} streptomycin.

2.2.12 Gene silencing assay

KB/eGFPLuc cells were used to prove the gene silencing potential of this novel lipopolyplex. We adopted siGFP for silencing the eGFP-luciferase fusion gene and siCtrl as a control for evaluating the non-specific silencing effect. KB/eGFPLuc cells were seeded in 96-well plates at a density of 5×10^3 cells/well 24 h prior to the treatments. On the next day, the medium was replaced with 80 µL of fresh medium and then 20 µL of sample solution containing a series of concentrations of GNs+siCtrl@Lipid and

GNs+siGFP@Lipid with or without *573* was added to each well. After incubation for 48 h, the medium was removed and 100 µL cell lysis buffer was added to each cell and the cells were incubated for 30 min at room temperature for complete protein release. Finally, the luciferase assay kit and Centro LB 96 plate reader luminometer were used to measure the luciferase activity in every well.

For LNPs, KB/eGFPLuc cells, N2a/eGFPLuc cells, and DU145/eGFPLuc were utilized to optimize the LNPs formulations with different N/P or N/(P+C) ratios. siGFP was used to silence eGFPLuc; the siCtrl was chosen to assess non-specific transfection effects. Cells were seeded in 96-well plates at a density of 5000 cells/well in standard cell culture medium contained 10% FBS one day before the treatments. Afterwards, the medium was replaced with 80 µL of fresh medium (containing 10 % FBS, 100 U mL^{-1} penicillin, and 100 µg mL^{-1} streptomycin) and 20 µL of LNP solution. The final amounts of siRNA were 100, 50, 25, 12.5, 6.25, 3.125, and 1.625 ng. The plates were incubated at 37 ^{o}C for 2 days. Then, the medium was removed, and 100 µL of cell lysis solution was added to fully lyse the cells by incubating at RT for 30 min. Following that, the luciferase activity was measured using a Centro LB 96 plate reader luminometer (Berthold, Bad Wildbad, Germany) with the help of a luciferin-LAR buffer solution. The transfection efficiency was calculated as a percentage of luciferase gene expression relative to HEPES buffer-treated control cells.

2.2.13 Cellular internalization

For lipopolyplex system, KB cells were seeded in 96-well plates at a density of 1×10^4 cells/well 24 h prior to treatments. On the next day, the lipopolyplexes containing 500 ng of siRNA including 20% siCy5 were added into each well. Following incubation for different time points, the cells were washed with 1×phosphate-buffered saline (PBS) and treated with 500 I.U. heparin to remove the lipopolyplex attached to the cell surface. The cells were finally suspended in PBS buffer containing 20% FBS and evaluated *via* a flow cytometry (Beckman Coulter, Fullerton, USA). The data were analyzed by the FlowJo 7.6.5 software (FlowJo, Ashland, USA).

For LNP system, KBs cells were plated in 96-well plates at a density of 10000 cells/well one day prior to the treatments. After that, the medium was replaced with 80 µL fresh DMEM (containing 10 % FBS, 100 U mL^{-1} penicillin, and 100 µg mL^{-1} streptomycin) and 20 µL of carrier solution. The nanocarrier solution contained 100 ng siCy5 as well as 4 µg hemin with an N/(P+C) ratio of 9. Following incubating the cells for different times (45 min, 4 h, 8 h, 12 h, and 24 h), 100 µL of PBS containing 500 IU heparin was introduced to clear away particles adhering to the cell. During the process, cells were incubated on ice for 30 min. Finally, the cells were collected, suspended in PBS with 10% FBS, and measured by flow cytometer in Cy5 channel (Ex: 635 nm, Em: 665 nm).

2.2.14 Endocytosis pathway

For determining the endocytosis pathway of lipopolyplex, three different pharmacological inhibitors were used according to the published literature. Cells were preincubated with different inhibitors (nystatin 15 µg mL^{-1}, sucrose 450 nM, amiloride 100 µM) for 1 h at 37 ^{o}C, then washed with PBS and incubated for 4 h after adding a medium containing lipopolyplexes. Finally, the cells were collected and measured by a flow cytometer.

For LNPs' uptake, one day before the treatments, KBs cells were plated in 96-well plates at a density of 10000 cells/well. Subsequently, the medium was replaced with 100 µL of serum-free medium containing various inhibitors (MβCD 5 mM, sucrose 450 mM, amiloride 100 µM) and incubated for 1 h at 37 ^{o}C. Afterwards, the medium was replaced with 80 µL of fresh medium (containing 10 % FBS, 100 U mL^{-1} penicillin, and 100 µg mL^{-1} streptomycin), and 20 µL of buffer containing 100 ng siCy5 and 4 µg hemin. For the 4 ^{o}C treatment, cells were placed at 4 ^{o}C cooling room for 1 h before adding siCy5-containing LNP in ice-cold medium. The following steps were carried out as described above.

2.2.15 Endosomal escape assay

The endosomal escape of the CET system was studied by confocal laser scanning microscopy (CLSM, Leica, Wetzlar, Germany) images using the HeLa-galectin-8 (Gal8)-mRuby3 cell line, stably expressing mRuby3-Gal8 fusion protein [105,106]. HeLa-Gal8-

mRuby3 cells were seeded in an 8-well Lab-Tek chamber at a density of 10000 cells/well. The following day, a fresh medium containing 10 % FBS, 100 U mL^{-1} penicillin, 100 µg mL^{-1} streptomycin, and different formulations was added, followed by incubation of the cells for 4 h, 12 h, 24 h, or 48 h. Subsequently, the cells were washed with PBS and fixed in a 4% PFA solution for 45 min at RT. DAPI and rhodamine-phalloidin were used to stain the cell nuclei and actin, respectively. Lastly, the cells were treated with PBS again to remove excess dye before observation with a CLSM. This work was performed by Miriam Höhn (Pharmaceutical Biotechnology, LMU München).

2.2.16 LysoTracker assay

To further investigate the endosomal escape of the lipopolyplex, KB cells were seeded in an 8-well Lab-Tek chamber, at a density of 20000 cells/well for 24 h. Next, the cells were incubated with 300 µL culture medium containing four kinds lipopolyplexes with 1500 ng of siRNA (siRNA@Lipid, GNs+siRNA@Lipid, TCPO+siRNA@Lipid, GNs+TCPO+siRNA@Lipid), which included 40% siCy5. The lipopolyplexes were prepared as described above. After incubation for 12 h, the cells were stained with LysoTracker Green DND-26 at a final concentration of 75 nM for 2 h. Thereafter, cells were washed with PBS before observation with a CLSM. This work was performed by Miriam Höhn (Pharmaceutical Biotechnology, LMU München).

2.2.17 Cellular ROS generation determination

KB cells were seeded in 96-well plates at a density of 1×10^4 cells/well, and then different groups were set. After 24 h, cells were treated with different kinds of lipopolyplexes (C_{GNs} = 100 µg mL^{-1}) for 12 h. For LNPs, the incubation time was 48 h. Each formulation contained siCtrl 100 ng $well^{-1}$, TCPO 8 µg $well^{-1}$, and hemin 130 ng $well^{-1}$. Subsequently, the cells were washed with PBS and stained with 750 nM CellROX@ Green reagent for 45 min at 37 °C. Finally, the cells were washed with PBS again and analyzed *via* flow cytometry.

To investigate the $^1O_2$ generation, KB cells were seeded in an 8-well Lab-Tek chamber, at a density of 2×10^4 cells/well for 24 h. Similar to flow cytometry measurement, the cells

were treated with different kinds of lipopolyplexes for 12 h. Then, the cells were stained with $^1O_2$ sensor green dye at a final concentration of 10 μM for 3 h. Thereafter, cells were washed with PBS again and observation with a CLSM. This work was performed by Miriam Höhn (Pharmaceutical Biotechnology, LMU München).

2.2.18 CET effect evaluation through cell viability

One day prior to the treatments, KB cells were seeded in 96-well plates at a density of 5×10^3 cells/well. Afterwards, the cells were incubated with a series of concentrations of formulations another 24 h or 48 h. Then a MTT assay was performed to evaluate the relative cell viability according to the standard protocol using SpectraFluor Plus microscopy reader (Tecan, Männedorf, Switzerland). In the case of the anti-oxidation experiment, cells were co-incubated with GNs+TCPO@Lipid and 1 or 3 mM *N*-acetylcysteine (NAC) for 24 h or 48 h, and then the same experimental steps were performed as described above.

Similarly, HEK293 and HT22 cells were adopted as H_2O_2 low-producing and $^1O_2$ high-sensitive cells for evaluating H_2O_2-induced cellular apoptosis. HEK293 and HT22 cells were individually seeded in 96-well plates at a density of 5×10^3 cells/well 24 h prior to the experiments with different concentrations of GNs+TCPO@Lipid or LNPs. After incubation for 24 h or 48 h, a standard MTT assay was performed.

2.2.19 JC-1 assay

2×10^5 KB cells were seeded in 12-well plates in each well 24 h prior to the treatment. The cells were separately treated with GNs@Lipid, TCPO@Lipid, and GNs+TCPO@Lipid for 24 h. Afterwards, the treated cells were collected and suspended in PBS buffer. And 50 μM carbonylcyanid-3-chlorphenylhydrazon treated cells were adopted as a positive control. Finally, 10 μL of 2×10^{-4} M JC-1 solution was added and the samples were incubated for 20 min, and analyzed with flow cytometry. The data was analyzed by the FlowJo 7.6.5 software.

2.2.20 Cell cycle test

1×10^4 KB cells were seeded on 96-well plates per well in 100 μL medium 24 h prior to the treatment. The medium was replaced with 80 μL of fresh medium and 20 μL of lipopolyplexes in HEPES buffer was added to each well. The concentration of GNs is 50 μg mL^{-1}. After incubation for 48 h, the cells were collected and suspension was added dropwise to 90 μL cold 70% ethanol and incubated at 4 °C for 2 h. Subsequently, the cells were centrifuged and incubated for 3 h in 100 μL PI staining buffer (0.1% sodium citrate, 0.1% Triton X-100, 180 units/mL RNase stock solution, and 50 μg mL^{-1} PI) with intermittent shaking. After that, the cells were collected, washed with PBS, measured by flow cytometry, and analyzed by the FlowJo 7.6.5 software.

2.2.21 siEG5 CET system

To measure the enhanced gene silencing efficacy, siEG5 was incorporated into the CET system. KB cells were seeded on 96 plates at a density of 5×10^3 cells/well 24 h prior to the treatments. Then, the medium was replaced with 80 μL of fresh medium (containing 10 % FBS, 100 U mL^{-1} penicillin, and 100 μg mL^{-1} streptomycin) and 20 μL of lipopolyplexes in HEPES buffer at various concentrations was added to each well. The lipopolyplexes included six groups: GNs+siCtrl@Lipid, TCPO+siCtrl@Lipid, GNs+TCPO+siCtrl@Lipid, GNs+siEG5@Lipid, TCPO+siEG5@Lipid, and GNs+TCPO+siEG5@Lipid. After incubation for 48 h, a MTT assay was performed to analyze the cell viability.

For LNP system, the formulations are Hemin+siEG5@Lipid, TCPO+siEG5@Lipid, and Hemin+TCPO+siEG5@Lipid, TCPO amount was 8 μg $well^{-1}$ and hemin amount was 130 ng $well^{-1}$. The other treatments were same as lipopolyplexes.

2.2.22 siNrf2 CET system

KB cells (5×10^3) were seeded on 96-well plates per well in 100 μL of medium 24 h prior to the treatment. Then, the medium was replaced with 80 μL of fresh medium (containing 10 % FBS, 100 U mL^{-1} penicillin, and 100 μg mL^{-1} streptomycin), and 20 μL of in HEPES

buffer containing LNPs was added. TCPO amount was 8 μg well^{-1} and hemin amount was 130 ng well^{-1}. After incubation for 48 h, a MTT assay was performed.

2.2.23 Annexin V-FITC/PI apoptosis assay

12-well plates were prepared with KB cells seeded at a density of 20000 cell/well 24 h prior to the treatments. Next, cells were incubated with different formulations for 48 h. The siRNA amount was 1.88 μg well^{-1}, the TCPO amount was 60 μg well^{-1}, and the hemin amount was 975 ng well^{-1}. Then cells were collected and washed with PBS to remove LNPs or lipopolyplex. Then, the cells were then suspended in 100 μL Annexin V binding buffer containing 1 μL Annexin V-FITC and 10 μL PI, incubated in room temperature for 15 min. Subsequently, the collected cells were measured by the flow cytometer.

2.2.24 Ribogreen assay

siRNA loading efficacy was determined by a Quant-iTTM RiboGreen® RNA assay kit. 50 μL LNPs were mixed with 50 μL of TE buffer or TE buffer containing 2% Triton X-100, and added to a 96-well plate. Next, 100 μL of Ribogreen solution was added to each well and incubated at 37 ^{o}C for 15 min. The fluorescence intensity was detected using a microplate reader (Tecan, Männedorf, Switzerland). The fluorescence intensity from TE buffer treated LNPs (F_{TE}) represents unencapsulated siRNA, and fluorescence intensity from 2% Triton X-100 treated LNPs (F_{TX}) represents total siRNA. The siRNA encapsulation efficiency can be determined as

$$Encapsulation\ \% = \frac{F_{TX} - F_{TE}}{F_{TX}} \times 100\%$$

For LNPs stability assay under different ionic strength conditions, 50 μL of TE buffer containing varying concentrations of Heparin and NaCl were added to 96-well plates, respectively. Subsequently, 50 μL of LNPs with an N/(P+C) of 9, containing 65 ng hemin, 4 μg TCPO, and 50 ng siRNA were added to each well. Final NaCl concentrations ranged from 0 to 5 M, and the final amounts of heparin ranged from 0 to 5 IU per μg of siRNA. After incubating for 30 min at 37 ^{o}C, 100 μL of Ribogreen solution was added to each well and incubated at 37 ^{o}C for 15 min. The fluorescence intensity was measured using a microplate reader. Additionally, the fluorescence intensity of LNPs mixed with 2% Triton

X-100 and TE buffer-treated LNPs was also tested. The fluorescence intensity of LNP samples (F_S) treated with different ionic strengths represents leaked siRNA. The fraction of dye exclusion can be calculated as

$$Fraction\ of\ dye\ exclusion\ = 1 - \frac{F_S - F_{TE}}{F_{TX} - F_{TE}}$$

2.2.25 RT-qPCR assay

One day before treatment, KB cells were seeded in 6-well plates at a density of 120,000 cells/well. Subsequently, the medium was replaced with 1600 µL of fresh medium (containing 10 % FBS, 100 U mL^{-1} penicillin, and 100 µg mL^{-1} streptomycin) and 400 µL of HEPES buffer (20 mM, pH 7.4) containing LNPs. Each well contained 400 µg of TCPO, 6.5 µg of hemin, and 2 µg of siRNA. After incubation for 48 h, KB cells were collected from the different treatment groups, and total RNA was extracted using the peqGOLD Total RNA kit. cDNA was synthesized using qScript™ cDNA SuperMix. Subsequently, RT-qPCR was conducted on a LightCycler 480 system using UPL Probes (Roche, Mannheim, Germany), TaqMan® Gene Expression, and Mastermix Assays. The comparative cycle threshold (Ct) method was employed to calculate the relative abundance of Nrf2 mRNA and EG5 mRNA, with GAPDH mRNA serving as the housekeeping gene. Every assay was performed in triplicate.

2.2.26 Statistical analysis

Data were expressed as the means G standard deviation of at least three independent experiments. The statistical significance of the experiments was determined using the two-tailed Student's *t* test (***$p \leq 0.001$, **$p \leq 0.01$, *$p \leq 0.05$).

3 Results and Discussion

3.1 CET-based lipopolyplexes for enhanced siRNA delivery

Section 3.1 has been adapted from: Fengrong Zhang, Yi Lin, Miriam Höhn, and Ernst Wagner*, Chemical-Electron-Transfer-Based Lipopolyplexes for Enhanced siRNA Delivery, Cell Rep. Phys. Sci., 2023, 4, 101444.*

RNAi therapeutics mediated by siRNA, is a sequence-dependent endogenous regulatory strategy capable of selectively down-regulating gene expression of human beings at the post-transcriptional level, holding superb prospects for genetic diseases and cancer therapy [5]. To date, the first FDA-approved siRNA drug, Onpattro [4,107,108], has been realized with the assistance of non-viral lipid-based nanoparticles. This approach is adopted to avoid rapid elimination in the bloodstream as well as poor cellular uptake of naked siRNA, which is due to its large molecular weight, negative charge, and hydrophilicity [16,17].

In most cases, non-viral nanosystems are internalized *via* an endo-lysosomal pathway [109–111]. However, a major technological bottleneck in realizing efficient gene silencing is the endosomal escape of nucleic acids [112]. One literature using real-time intracellular tracking demonstrated that only 1–2% of lipid nanocarriers could achieve endosome-to-cytosol transfer [38].

Owing to the tremendous advances in optical technology and nanotheranostics [113], cytoplasmic delivery with the assistance of photochemical internalization, i.e., photochemical disruption of the endosomal membrane [61,114–116], has been explored to resolve this delivery bottleneck. Although photochemical internalization is ideal for superficial tissues, the external photoexcitation usually induces unspecific skin and tissue damage and suffers from insufficient energy supply, which makes it unsuitable for clinical application in deep-sited and metastatic tumors [69,117]. As an alternative, CET self-initiated by the tumor microenvironment without external irradiation has been explored. CET is defined as the transfer of non-radiative energy between donors and ground state PSs [118–121]. Similar to conventional photodynamic therapy, the excited electrons

transfer to a higher energy orbital of the PSs, undergo intersystem crossing, and then excite oxygen to generate $^1O_2$ *via* the type II photochemical reaction [55,122–124].

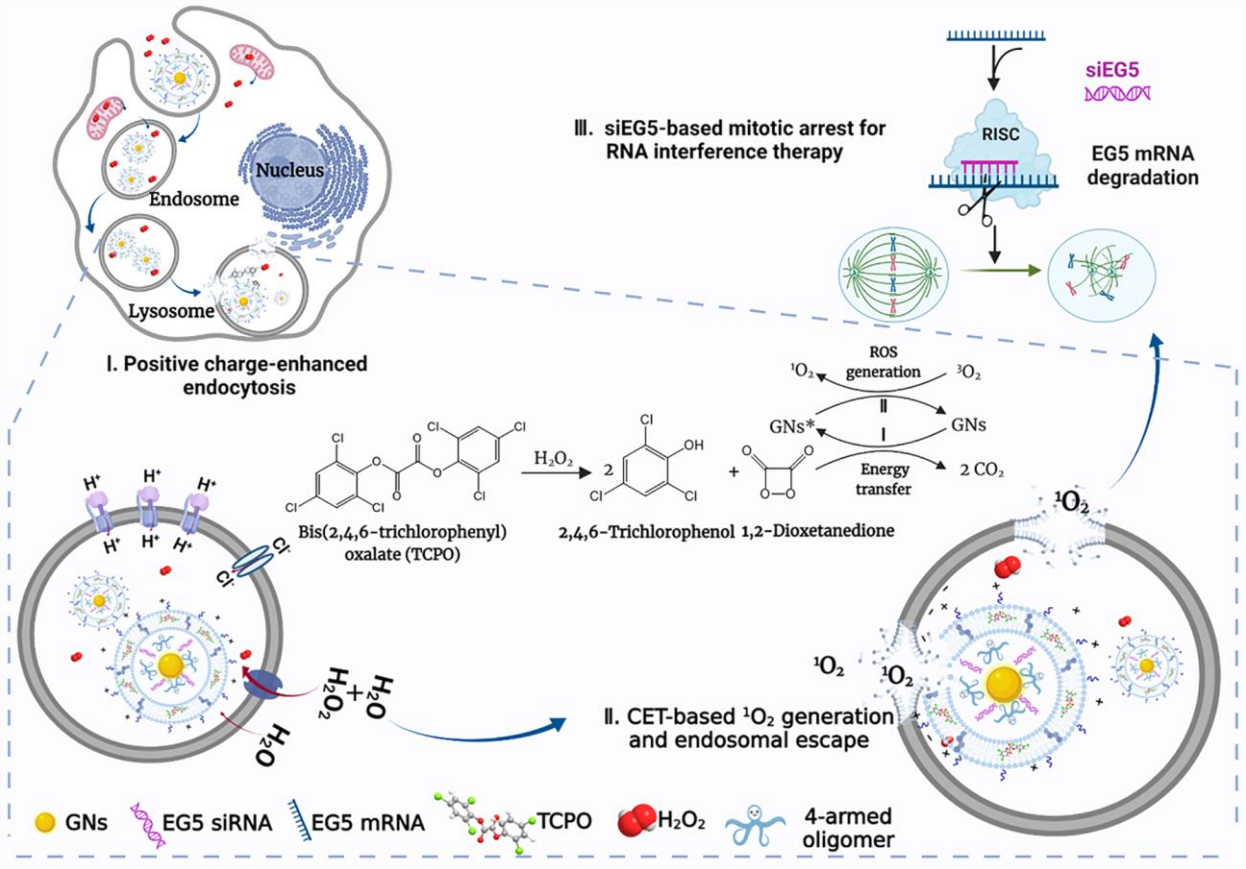

Scheme 1. Illustration of CET-based $^1O_2$ generation and endosomal escape for enhancing gene therapy.

Inspired by the lipid peroxidation and protein oxidation of $^1O_2$, herein, we were committed to developing a novel CET-based lipopolyplex as the first example showing the self-exciting chemical internalization-assisted endosomal escape of siRNA (**Scheme 1**). In detail, the positively charged lipopolyplex acted as a nanocarrier, encapsulated CET donor (oxalate derivative) in the hydrophobic section, and acceptor (GNs), siRNA, and cationic oligomer in the hydrophilic core. Once the lipopolyplex accumulates into the H_2O_2-rich tumor cell environment, GNs are chemically excited by energy-rich intermediate (1,2-dioxetanedione) which is generated from a reaction between TCPO and endosomal H_2O_2, inducing $^1O_2$ generation by catalyzing molecular oxygen. The sequence-defined cationic oligomer located in the core of the lipopolyplex was synthesized *via* SPPS, which

possesses proton-sponge and nucleic acid loading dual function. The resulting $^1O_2$ and oligomer facilitated endosomal membrane rupture and synergized siRNA targeting EG5 mRNA, initiating the tumor cellular apoptosis program [125]. Meanwhile, oxidation of $^1O_2$ along with the proton-sponge effect of the cationizable carrier greatly improved endosome-to-cytosol transfer. Overall, we demonstrate the first success in CET-enhanced RNAi *via* internal disrupting the endosomal membrane of cancer cells.

3.1.1 Formulation and characterization of CET-based lipopolyplexes

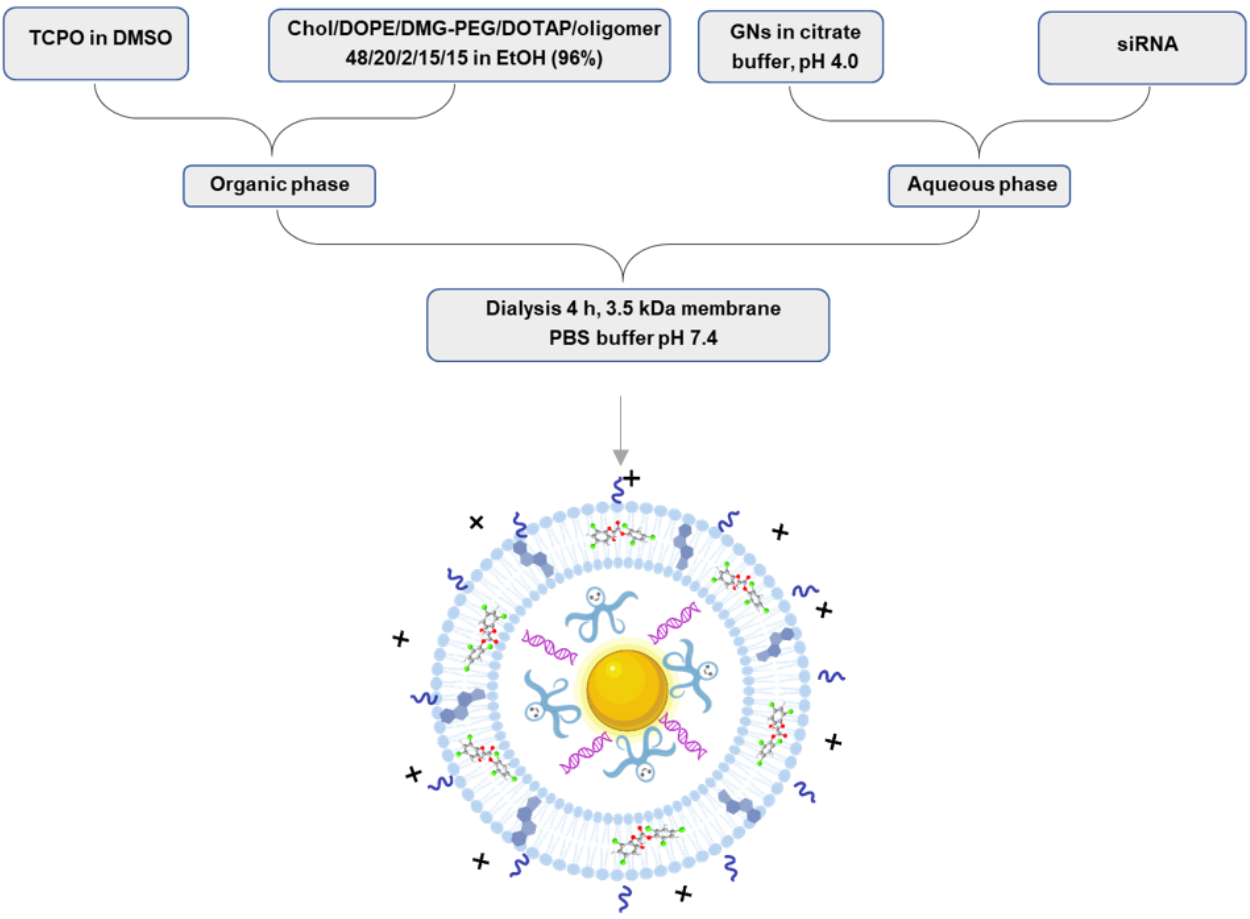

Scheme 2. Schematic illustration of lipopolyplex formulation. Lipids (Cholesterol, DOPE, PEG-DMG, and DOTAP), oligomer *573*, and TCPO were well dissolved in organic phase. siRNA was mixed with GNs in sodium citrate buffer (pH 4). Finally, the lipopolyplex was formed *via* adding the aqueous solution into the organic mixture.

The CET-based lipopolyplex was formulated according to the solvent-exchange deposition strategy [126,127], which involved a lipid mixture including helper lipids (cholesterol as well as PEG lipid, cationic lipid (DOTAP), and sequence-defined cationic four-armed oligomer *573* (**Figure 7A**). Briefly, the lipids and TCPO were well dissolved in the organic phase firstly, meanwhile, siRNA was mixed with GNs in sodium citrate buffer (pH 4). After that, the GNs-oligomer-siRNA complex was encapsulated in the hydrophilic cavity of the lipopolyplex *via* dramatically upregulating volume of the aqueous solution (**Scheme 2**).

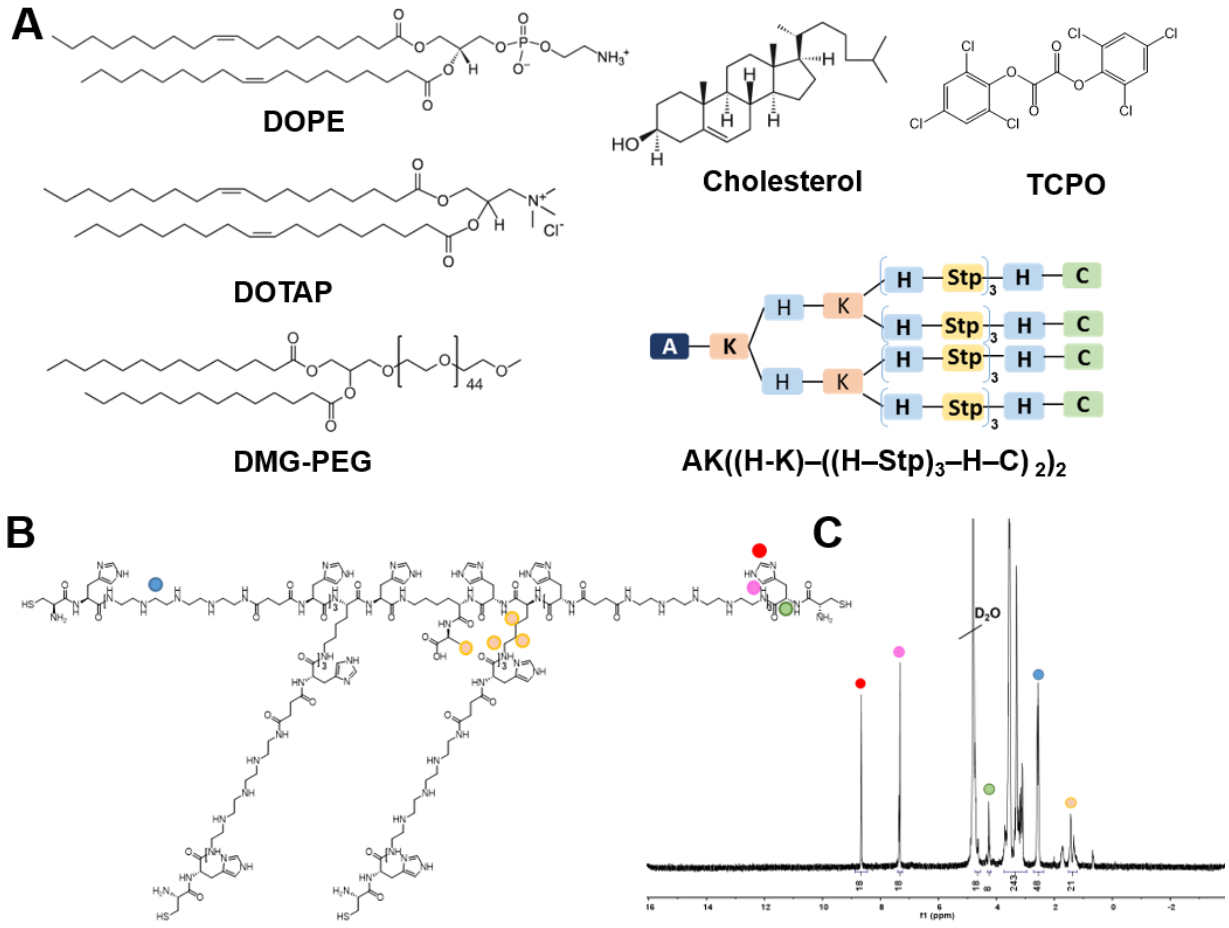

Figure 7. Formulation and characterization of CET-based lipopolyplex. (A) Structures of lipids, oxalate, and four-armed oligomer *573* involved in the lipopolyplex. A: alanine; K: lysine; H: histidine; C: cysteine. Stp: succinyl-tetraethylene-pentamine. (B) Structure of four-armed oligomer *573* synthesized *via* SPPS. (C) ^{1}H-NMR spectrum of *573* in D_2O. Yellow points: δ(ppm) = 1.0–1.5 (m, 21H, βH alanine, βγδH lysine); Blue points: 2.3–2.6 (m, 48H, –CO–CH_2–CH_2–CO–succinic acid);

Green points: 4.0–4.3 (m, 8H, αH alanine, αH cysteine, and αH lysine); Pink points: 6.9–7.5 (m, 18H, imidazole); Red points: 8.4–8.7 (d, 18H, imidazole).

Cationic Stp, providing three protonatable amines, was adopted as a building block for synthesizing sequence-defined four-armed oligomer AK((H–K)–((H–Stp)$_3$–H–C)$_2$)$_2$ (*573*) using solid-phase assisted peptide chemistry. The four-armed structure contained terminal cysteines which exposed free thiol groups not only for Au–S bond formation with GNs, but also for the disulfide crosslinking within the oligomer's hydrophilic core. Importantly, this cationic four-armed oligomer could attract anionic nucleic acids electrostatically and enabled endosomal escape of loaded cargo through protonation of Stp and histidine (**Figure 7B**). The successful synthesis of *573* was demonstrated by the NMR spectrum in **Figure 7C**. This oligomer was previously successfully used for plasmid DNA transfer but not for siRNA delivery [99].

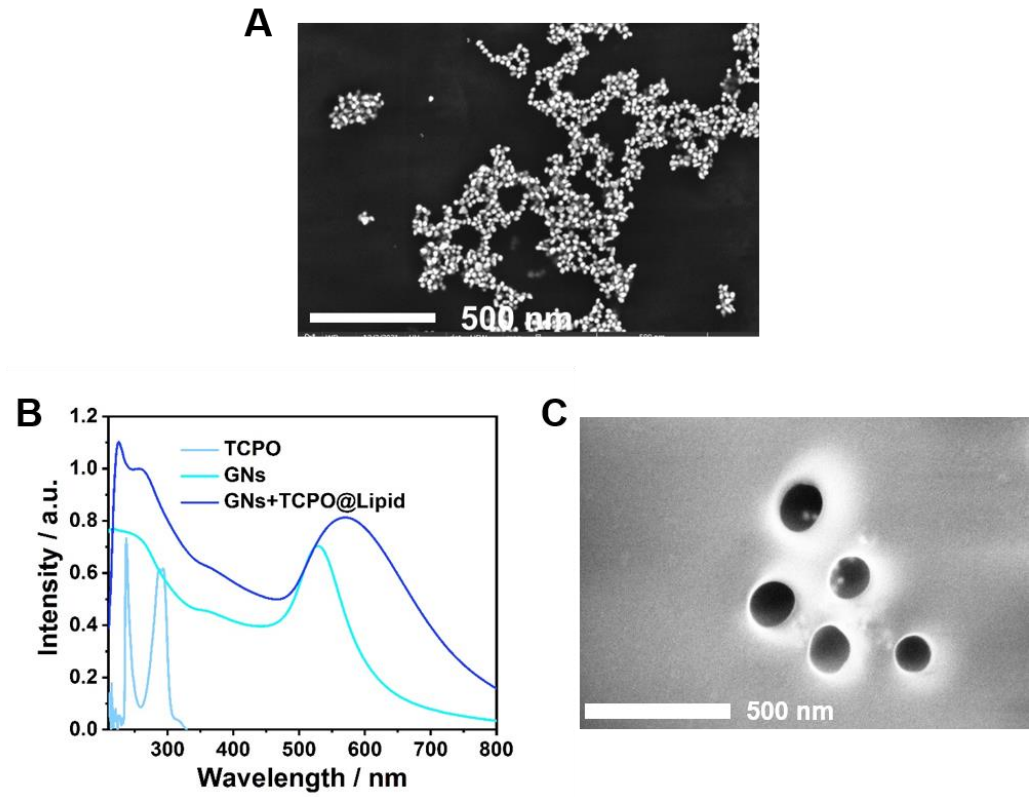

Figure 8. Physicochemical features of the formulations. (A) TEM showing the morphology and size of GNs. (B) UV–vis light absorption spectra of TCPO, GNs, and GNs+TCPO@Lipid. (C) TEM image of GNs+TCPO+siRNA@Lipid.

GNs were selected as the inorganic nanoparticle core of the lipopolyplex and fabricated as previously published method with a slight modification [98]. A TEM image showed that GNs were monodisperse with an average diameter of around 30 nm (**Figure 8A**). Adopting GNs as a start point, we further incorporated siRNA, TCPO, four-armed oligomer, and lipids into the system, generating the CET-based lipopolyplex (GNs+TCPO+siRNA@Lipid). During the preparation of the lipopolyplex, siRNA, the hydrophilic negatively charged nucleic acid sequence, was automatically encapsulated inside the core. The UV–vis–NIR absorption spectra and TEM image of GNs+TCPO+siRNA@Lipid greatly suggested that GNs and TCPO were successfully incorporated into the lipopolyplex (**Figure 8B and C**).

3.1.2 Characterization of CET system for ROS generation

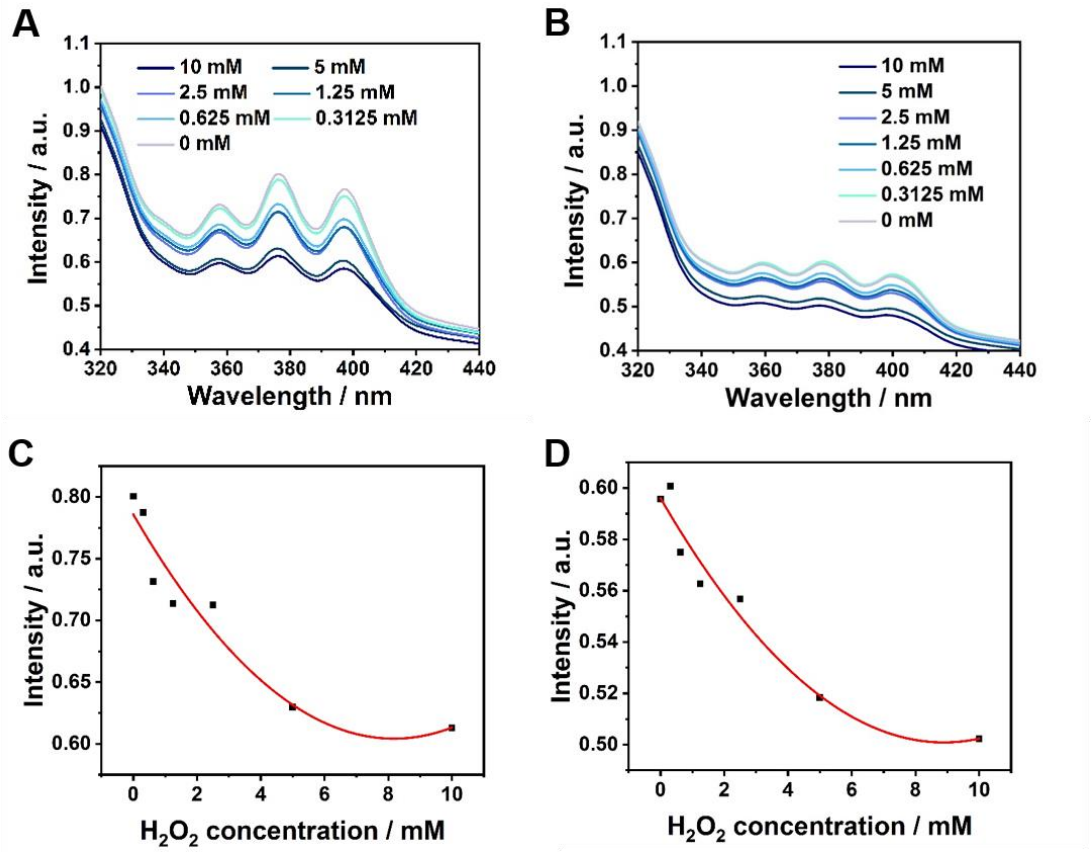

Figure 9. Analysis of the generation of $^1O_2$. H_2O_2 concentration-dependent DPA degradation spectra. (A) Reaction time is 5 min and (B) reaction time is 2 h. Rate constant for DPA decomposition under different concentration of H_2O_2 (C) T = 5 min and (D) T =2 h.

The CET effect is the prerequisite for subsequent ROS generation, thus DPA dye was chosen to confirm this crucial effect, which can be oxidized to related dioxide under the existence of $^1O_2$ (one of ROS) [81,128]. As the H_2O_2 concentration increased, the three characteristic absorption peak of DPA dye gradually decreased within 5 min (**Figure 9**). Besides, the oxidation also displayed apparent time-dependency when the reaction time was prolonged from 5 min to 2 h. The corresponding CET reaction was monitored by an UV–vis–NIR spectrometer.

Furthermore, to investigate the CET-based reaction, the characteristic absorption peak of GNs at 536 nm was attenuated after the addition of TCPO and H_2O_2; moreover, a new species was formed, leading to a new absorption peak at 777 nm (**Figure 10**).

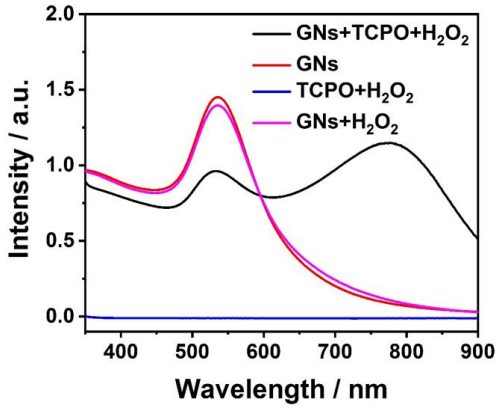

Figure 10. UV–vis–NIR light absorption spectra of GNs, GNs+TCPO+H_2O_2, TCPO+H_2O_2, and GNs+ H_2O_2 aqueous solution.

3.1.3 Optimization of lipopolyplex for siRNA loading and gene silencing

Since lipopolyplexes formation can vary with the ratio of cholesterol, phospholipids, PEG-DMG, DOTAP, and four-armed oligomer, we tested the various formulations using different molar ratios (**Figure 11A and B**). *573* was the most prominent component of the lipids, so we postulated that it impacts the formulation, lipopolyplexes with series *573* ratios were prepared. Dynamic light scattering (DLS) was performed to demonstrate the size and zeta potential shift of the resulting particles, observing that lipids with 0 to 40% *573* formed lipopolyplexes with an average diameter ranging from 90 nm to 230 nm

(**Figure 11C and D**). We concluded that GNs+siRNA@Lipid size varied with the ratio of the cationic oligomer, but there was no obvious regularity in the results.

A

Molar ratio				
573	15	10	5	0
DOTAP	15	20	25	30
Cholesterol	48	48	48	48
PEG-DMG	2	2	2	2
DOPE	20	20	20	20

B

Molar ratio				
573	40	30	20	10
Cholesterol	48	48	48	48
PEG-DMG	2	2	2	2
DOPE	10	20	30	40

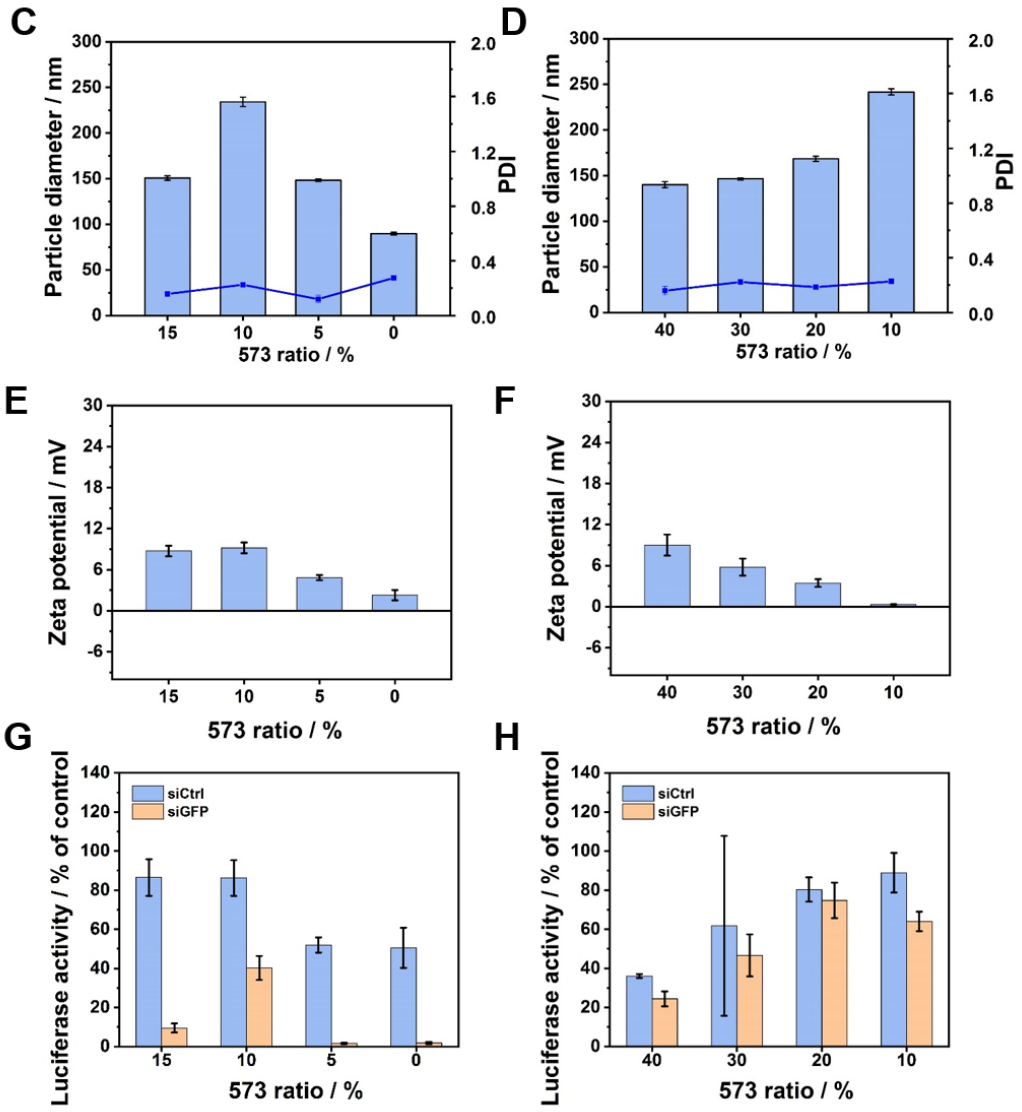

Figure 11. Optimization of lipopolyplex formulation by adjusting lipids molar ratio. (A) (B) Specific ratio of cholesterol, phospholipids, PEG-DMG, DOTAP, and four-armed oligomer for

lipopolyplexes. (C) (D) Size distributions (Z-average), PDI, (E) (F) zeta potentials, and (G) (H) eGFPLuc gene silencing efficiency of GNs+siRNA@Lipid with different 573 ratios.

Importantly, the tendency of zeta potential clearly showed *573* dose dependence (**Figure 11E and F**). We also evaluated the gene silencing potential of the corresponding nanocarriers, a human cervix carcinoma KB/eGFPLuc cell line which expresses eGFPLuc fusion protein was used. The control siRNA was used to exclude any non-specific eGFPLuc reduction. At a specific ratio of lipids (cholesterol/phospholipids/PEG-DMG/DOTAP/*573*: 48/20/2/15/15 mol%), the lipopolyplexes exhibited superior gene silencing (**Figure 11G and H**).

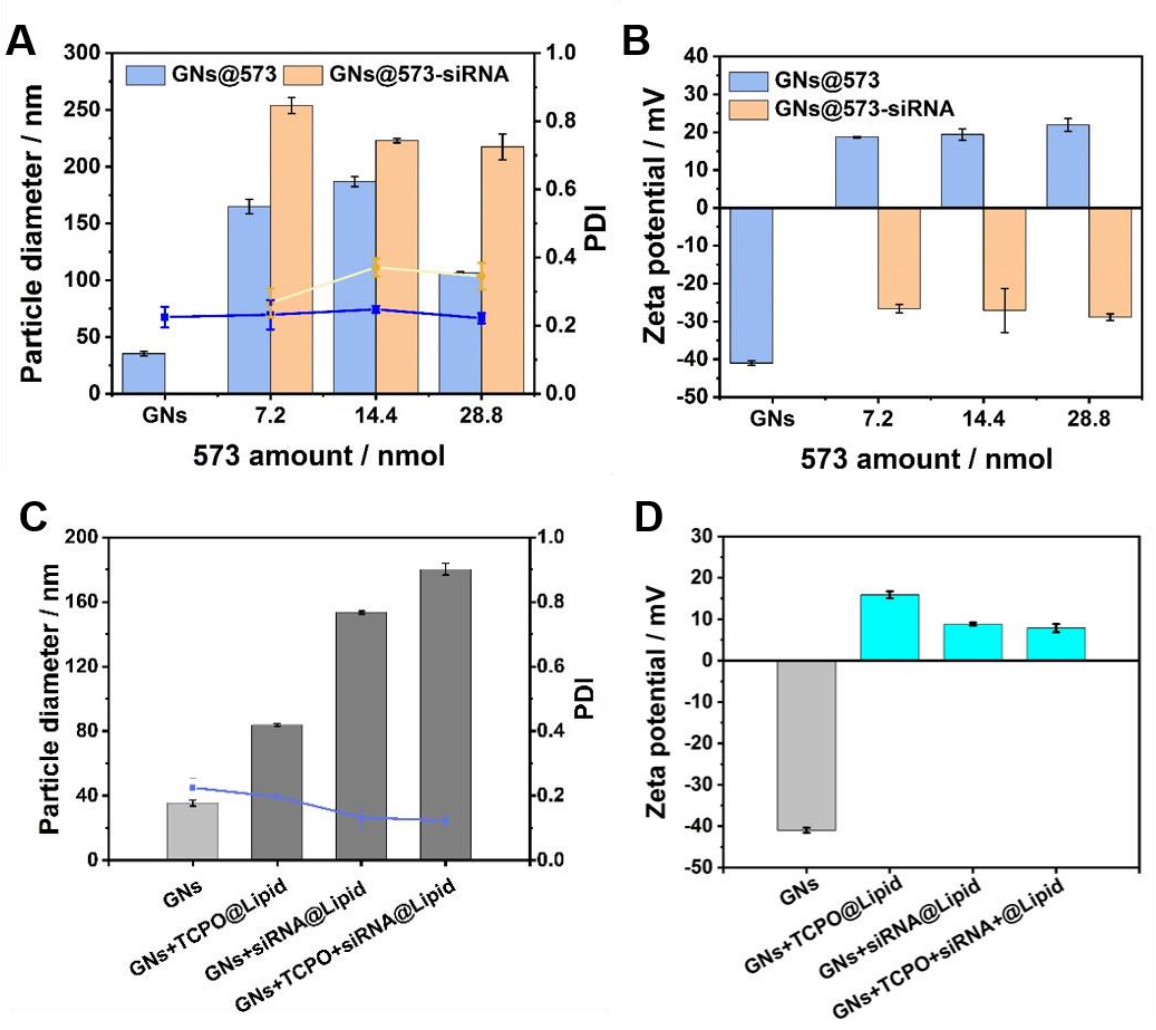

Figure 12. Analysis of GNs coated with different amount of oligomer with or without siRNA. (A) Particle sizes (Z-average), PDI and (B) zeta potentials of the formulations. (C) Size distributions

(Z-average), PDI, and (D) zeta potentials of GNs, GNs+TCPO@Lipid, GNs+siRNA@Lipid, and GNs+TCPO+siRNA@Lipid.

Further exploration of encapsulation amount of the four-armed oligomer *573* showed that 7.2 nmol of *573* was sufficient to reverse the charge of GNs (**Figure 12A and B**). Taken together, the addition of TCPO and siRNA resulted in an increase in average diameter from 35 nm to 84 nm (GNs+TCPO@Lipid) and 153 nm (GNs+siRNA@Lipid), respectively (**Figure 12C**). Finally, the lipopolyplex (GNs+TCPO+siRNA@Lipid) possessed the largest size less than 200 nm and it benefits tumor accumulation *via* passive targeting. Consistent with the observation in size, the zeta potential of GNs shifted from –41 mV to positive charge after coating with the cationic lipid (**Figure 12D**).

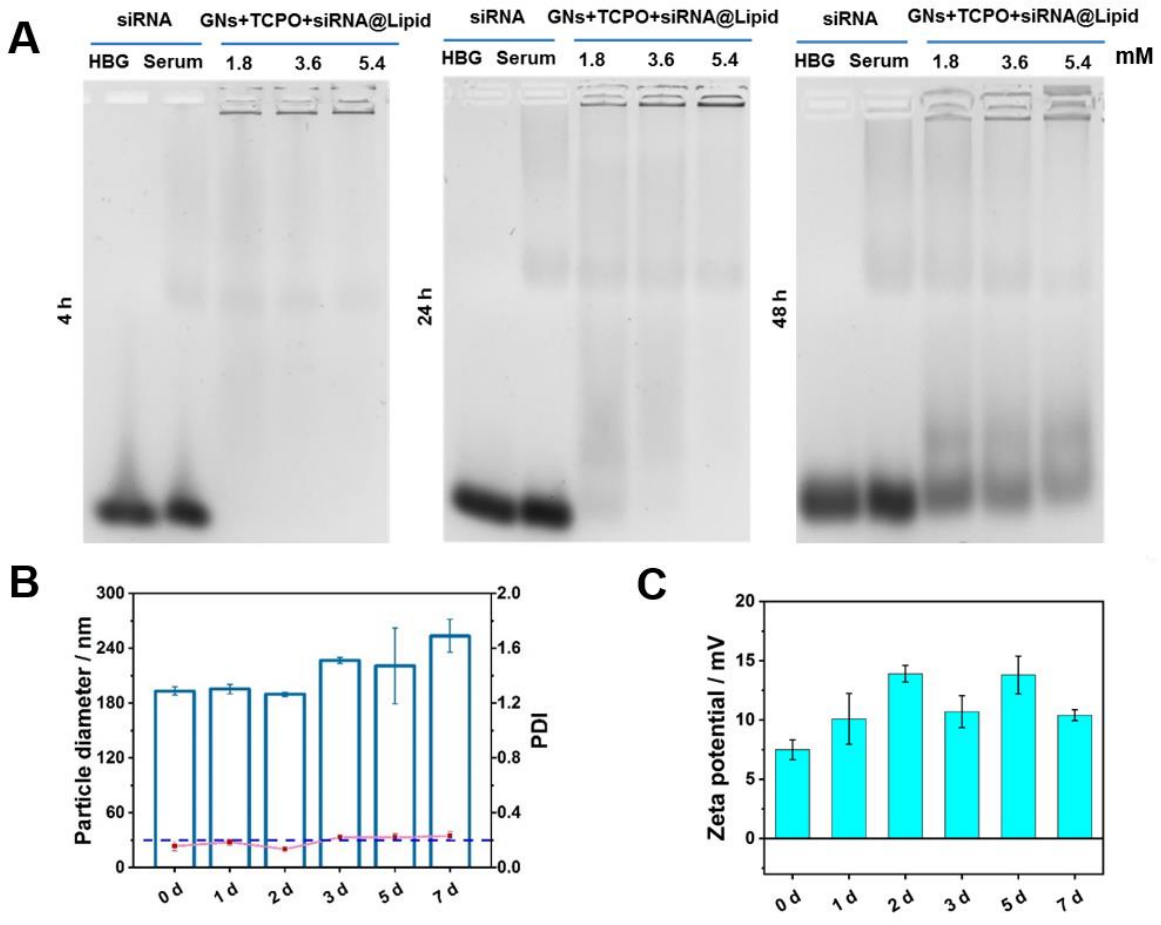

Figure 13. Optimization of lipopolyplex for siRNA loading and gene silencing. (A) siRNA binding assay of lipopolyplex coated with different amounts of lipids (1.8, 3.6, and 5.4 mM). The

lipopolyplexes were incubated with 90% FBS at 37 °C for 4 h, 24 h, and 48 h, respectively. 2.5% agarose gel, 100 V, 60 min running time. (B) Particle size (Z-average), PDI, and (C) zeta potentials of lipopolyplex measured by DLS. The lipopolyplex was incubated in PBS (pH=7.4) at 4 °C for one week. The blue dotted line represents a PDI value of 0.2.

To better explore the stability of the lipopolyplex, the siRNA binding efficiency with different lipid concentrations was analyzed by evaluating the electrophoretic mobility of GNs+TCPO+siRNA@Lipid in a 2.5% agarose gel (**Figure 13A**). After incubating lipopolyplex with 90% FBS for 4, 24, and 48 h, the electrophoresis assay was performed. At the 24-h incubation time point, some siRNA leaked out the lipopolyplex at a lipid concentration of 1.8 mM. When we up-regulated the lipid concentration to 3.6 mM, complete gel retardation of siRNA was observed. According to this result, a lipid concentration of 3.6 mM was selected for all formulations in the following experiments. Besides, under this condition, the lipopolyplex exhibited excellent stability in PBS at 4 °C for one week, which was supported by the slight size increase and negligible discrepancy of zeta potentials (**Figure 13B and C**).

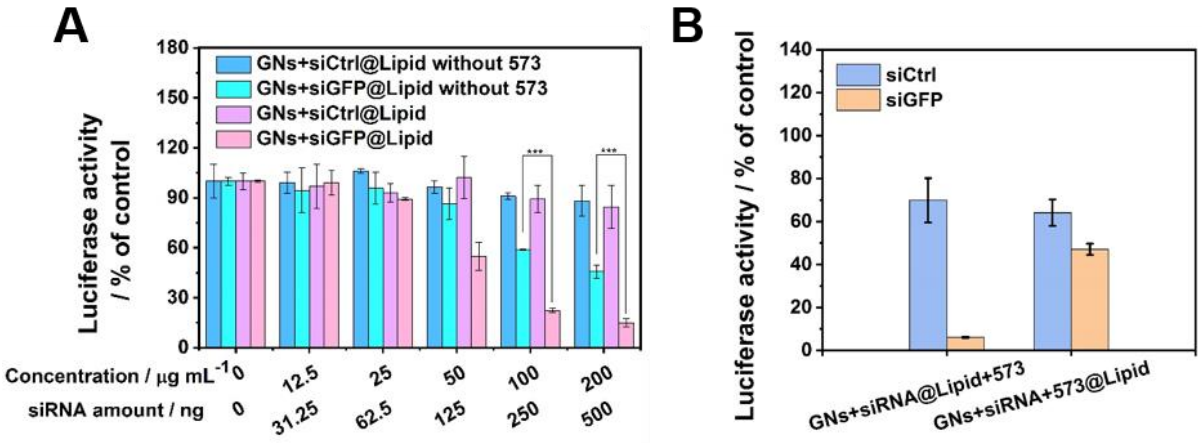

Figure 14. (A) eGFPLuc gene silencing efficiency of different concentrations of GNs+siRNA@Lipid with or without four-armed oligomer. The lipopolyplexes were prepared with siGFP and siCtrl, respectively. (B) eGFPLuc gene silencing efficiency of GNs+siRNA@Lipid+*573* (added *573* together with other lipids) and GNs+siRNA+*573*@Lipid (layer-by-layer encapsulation). **P* < 0.05, ***P* < 0.01, ****P* < 0.001, *****P* < 0.0001. Data are presented as mean ± SD (n = 5).

To further confirm the impact of *573* on lipopolyplex-mediated gene silencing, we prepared two distinct formulations, one with and one without the four-armed oligomer. The group treated with GNs+siRNA@Lipid lacking *573* exhibited approximately 55% knock-down of eGFPLuc after 48 h incubation, whereas the corresponding lipopolyplex containing the four-armed oligomer could induce an increased gene silencing efficiency to 85% (**Figure 14A**)**.** Both siCtrl formulations showed negligible intrinsic cytotoxicity. In addition, the final gene silencing efficiency was also dependent on the adding order of the 4-armed oligomer during the lipopolyplex preparation. To our understanding, the hydrophilic *573* in lipid mixture would competitively bind to GNs and siRNA to achieve a balance of encapsulation and release, we proved that the post-encapsulation (adding *573* together with other lipids) exhibited better gene silencing than layer-by-layer encapsulation (**Figure 14B**).

3.1.4 Evaluation of cellular uptake of lipopolyplexes

Outstanding gene silencing usually depends on efficient cellular uptake, reasonably, we explored the endocytosis of the lipopolyplexes in KB cells (**Figure 15A**). Notably, nearly no obvious shift was observed for naked siRNA without lipid encapsulation. By comparison, the endocytosis of the GNs+siRNA@Lipid group increased to 140% after 24 h incubation. Importantly, the uptake of the lipid-engaged group was superior over unencapsulated siRNA at 45 min. To further define the feasibility of self-exciting GNs, ROS level was assessed by flow cytometry (**Figure 15B**). Compared with the control group, quantification of fluorescence intensity in cells demonstrated significantly higher ROS generation in the GNs+TCPO@Lipid treated cells with a 44% fluorescence enhancement. To our understanding, the GNs in the lipopolyplex were chemically excited by an energy-rich intermediate (1,2-dioxetanedione), and then excite oxygen to generate $^1O_2$ *via* the chemical reaction. To look for more supporting evidences for the CET effect initiated $^1O_2$ generation, a $^1O_2$-selective sensor dye, $^1O_2$ sensor green, was employed (**Figure 15C**). As expect, the CLSM confirmed that only the combined group exhibited bright $^1O_2$ florescence signal.

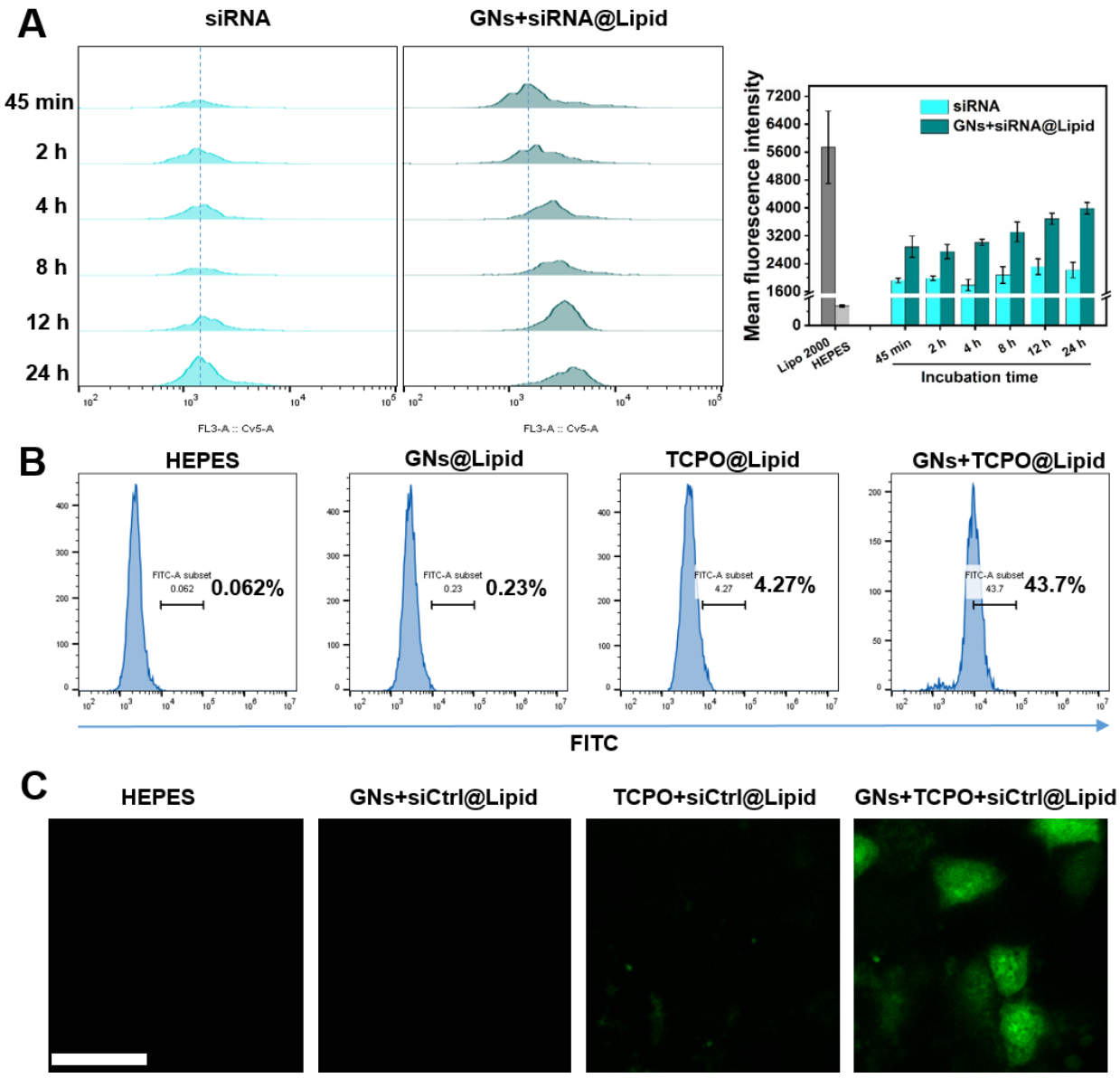

Figure 15. Evaluation of cellular uptake and CET effect. (A) Left part: cellular uptake assay of naked siRNA and GNs+siRNA@Lipid in KB cells obtained by flow cytometry after 45 min, 2 h, 4 h, 8 h, 12 h and 24 h incubation. Right part, the corresponding quantitative analysis of Cy5 fluorescence intensity. Lipo 2000 and HEPES buffer were adopted as positive and negative controls, respectively. (B) Detection of ROS level in KB cells treated with different formulations for 12 h. (C) Fluorescence image of KB cells incubated with different lipopolyplexes. Green represents $^1O_2$ fluorescence. Scale bar, 25 µm. The CLSM was performed by Miriam Höhn (Pharmaceutical Biotechnology, LMU München).

3.1.5 Evaluation of CET effect through cell viability

Before confirming the feasibility of lipopolyplex-mediated oxidative damage, the potential cellular cytotoxicity was firstly evaluated. Encouragingly, after incubation of KB cells with GNs@Lipid and TCPO@Lipid for 24 h, the superior biosafety of the basic components of the CET system was validated (**Figure 16A**). The highest cell lethality of GNs+TCPO@Lipid can be attributed to the combined effect of TCPO and GNs. After incorporating GNs and TCPO, the inhibitory effects of GNs+TCPO@Lipid on KB cells displayed a TCPO dose-dependent behavior (**Figure 16B**). Consistent with the above result, more than 50% of cells viability decreased when the GNs concentration increased up to 200 μg mL^{-1}. Given this consequence, NAC, holding the functions of anti-oxidation [129], scavenging free radicals, and regulating cellular metabolic activity, was adopted to further indirectly validate the presence of $^1O_2$ (**Figure 16C**). Consistent with our assumption, KB cell viability exhibited a concentration-related improvement when exposed to NAC.

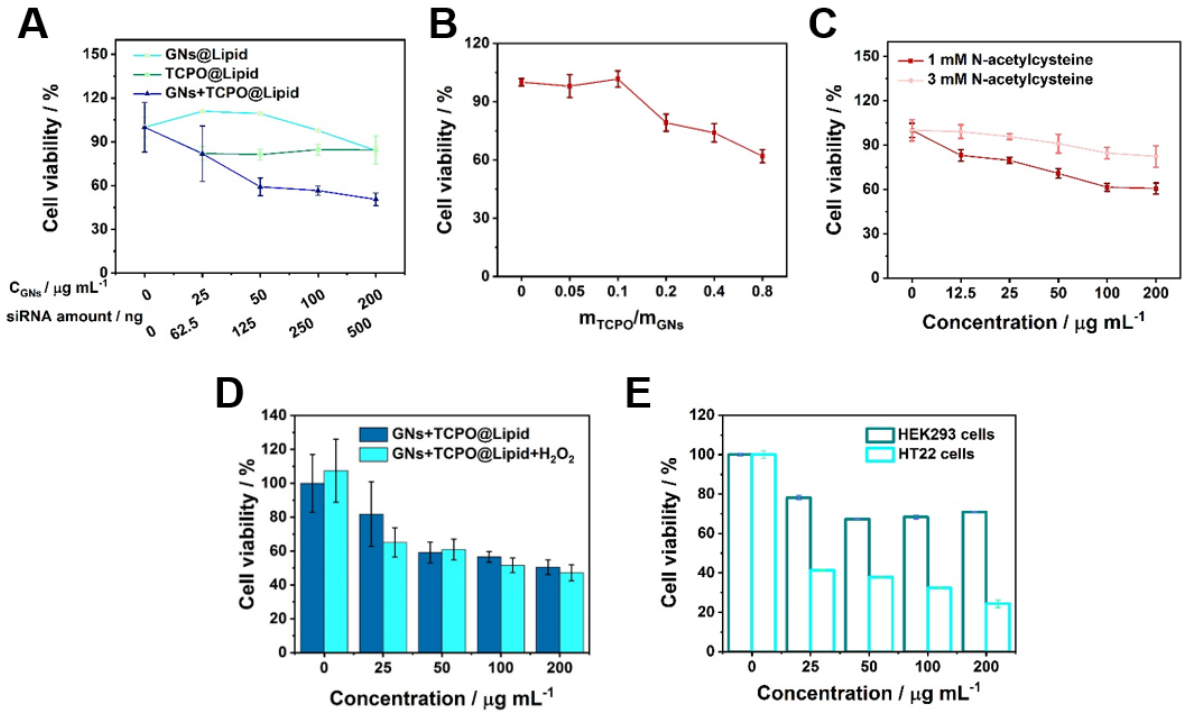

Figure 16. Evaluation of CET effect-mediated cell killing. Cell viability of KB cells incubated with (A) various concentrations of GNs+siCtrl@Lipid, TCPO+siCtrl@Lipid, and

GNs+TCPO+siCtrl@Lipid, (B) various weight ratios of TCPO to GNs (m_{GNs} = 10 μg well^{-1}), (C) GNs+TCPO+siCtrl@Lipid in the presence of 1 mM or 3 mM NAC, (D) a series of concentrations of GNs+TCPO@Lipid with or without H_2O_2 (100 μM). The incubation time is 24 h. (E) Cell viability of HEK293 and HT22 cells incubated with different concentrations of GNs+TCPO@Lipid for 24 h.

Additionally, previous reports have clearly demonstrated that cancer cells remain an enhanced metabolic rate, leading to high production of H_2O_2 in mitochondria. The over-expressed H_2O_2 plays one indispensable role in the reaction with TCPO [130,131]. To confirm whether additional H_2O_2 is required in the medium, the cellular viability with or without H_2O_2 addition was assessed. As shown in **Figure 16D**, the negligible discrepancy was discerned with extra H_2O_2. Meanwhile, HEK293 and HT22 cells, were adopted as H_2O_2 low-producing and $^1O_2$ high-sensitive cells for evaluating H_2O_2-induced cellular apoptosis, respectively [132]. Compared to KB cells and HEK293 cells, GNs+TCPO@Lipid treatment could mediate more efficient cell damage in HT22 cells, with cell viability lower than 25% at a GNs concentration of 200 μg mL^{-1} (**Figure 16E**).

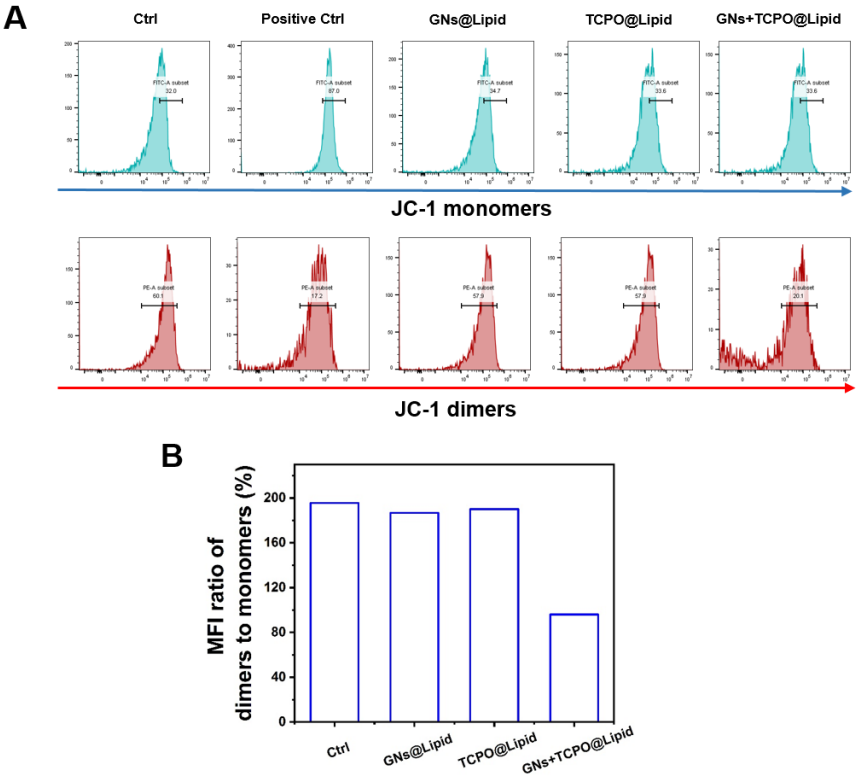

Figure 17. Mitochondrial membrane potential stained by JC-1 after KB cells were incubated with different formulations for 24 h. (A) Flow cytometry data presenting the shift of green and red

fluorescence by various treatments. (B) Quantitative analysis of the mean fluorescence intensity ratio of dimers to monomers.

Increasing evidence has proved that the mitochondrial membrane could be damaged by $^1O_2$. So JC-1 was employed as an indicator of mitochondrial dysfunction, which performs as red JC-aggregates in normal mitochondria due to relatively high mitochondrial membrane potential, and re-disperses as green fluorescence in damaged mitochondria [133]. As shown in **Figure 17**, the combined group (GNs+TCPO@Lipid) exhibited the lowest red/green fluorescence ratio compared with single treatments and the control group, indicating a relatively high ratio of mitochondrial membrane depolarization in KB cells. Taken together, these data evidence the superior ROS generation in the lipopolyplex-mediated CET system.

3.1.6 Evaluation of endosomal escape

To fully explore the ROS-enhanced endosomal escape, we explored the intracellular trafficking of lipopolyplexes by monitoring Cy5-labeled siRNA and LysoTracker-stained endosome or lysosome. It can be seen that siRNA was efficiently endocytosed by cells with the help of the lipopolyplexes, but they were mostly co-localized in endosomes and lysosomes for groups without TCPO or GNs (**Figure 18A**). By comparison, the co-localization between siRNA and endosome or lysosome was significantly reduced for GNs+TCPO+siRNA@Lipid. Effective endosomal escape can be attributed to the rupture of its membrane, so a cytosolic Gal8-mRuby3 fusion protein was selected as a sensor of endosomal membrane damage (**Figure 18B**). Without endosomal disruption, Gal8 is unable to contact its molecular targets, which are galactose-containing glycans exposed only at the inner membrane of endocytic endosomes, and is evenly distributed within the cytosol, see HEPES buffer negative control groups. In case of endosomal rupture, the Gal8 protein is able to be recruited to the now exposed galactose-containing glycans, resulting in punctuate fluorescent pattern of Gal8-mRuby3 of disrupted endosomes [133]. Thus, in HeLa cells expressing Gal8-mRuby3 fusion protein, the foci of intracellular galectin per cell was adopted as evidence of endosomal escape [104]. Consistent with the MTT results, the recruitment of Gal8-mRuby3 was most abundant in the ROS-

generated group, holding an obvious signal increase that was ~51-fold higher than HEPES group (**Figure 18B and C**).

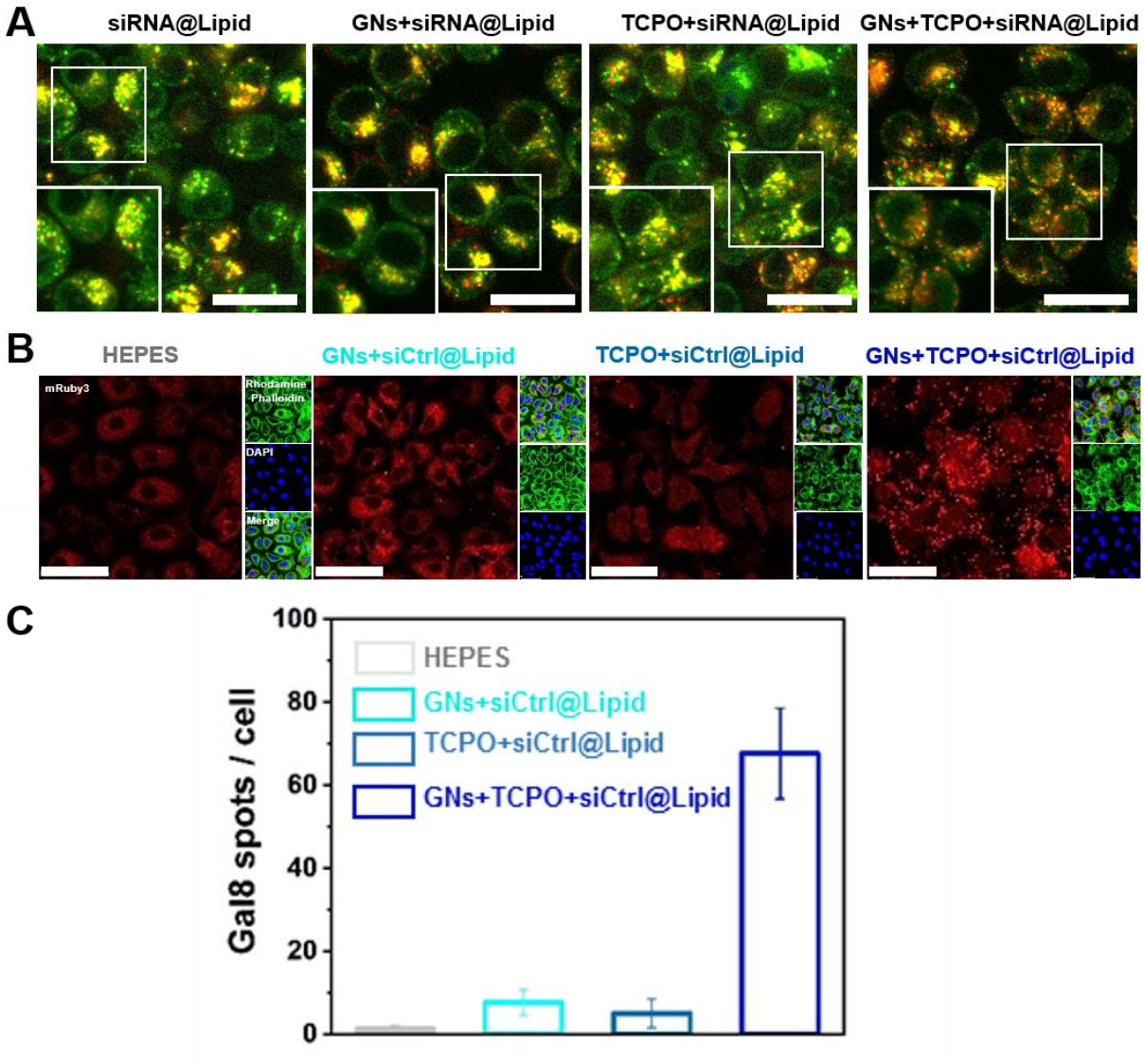

Figure 18. Endosomal escape and cellular uptake mechanism of lipopolyplexes. (A) CLSM images of KB cells incubated with siRNA@Lipid, GNs+siRNA@Lipid, TCPO+siRNA@Lipid, and GNs+TCPO+siRNA@Lipid for 12 h. siRNA was labeled with Cy5 (Red), Endo/lysosomes were stained with Lysotracker (Green). The left lower corner presents the 1.5-fold magnification area indicated by the white squares. Scale bar, 25 μm. (B) Subcellular localization of HeLa cells expressing Gal8-mRuby3 after treatments with HEPES, GNs+siCtrl@Lipid, TCPO+siCtrl@Lipid, and GNs+TCPO+siCtrl@Lipid for 4 h. Red, green, and blue fluorescence represent Gal8-mRuby3, actin filaments, and nucleus, respectively. Scale bar, 75 μm. HeLa cells expressing Gal8-mRuby3

fusion protein were established by Dr. Yi Lin (former PhD student at Pharmaceutical Biotechnology, LMU München). (C) Quantitative analysis of Gal8 spots per cell for Figure 18B. The CLSM was performed by Miriam Höhn (Pharmaceutical Biotechnology, LMU München).

Besides, we observed around 6-fold and 4-fold enhancements after 4 h exposure to GNs+siRNA@Lipid and TCPO+siRNA@Lipid, respectively. Notably, such increases were consistence with the fusogenic, inverted hexagonal lipid structure of DOPE and the proton sponge effect of the cationic four-armed oligomer (**Figure 19A and B**).

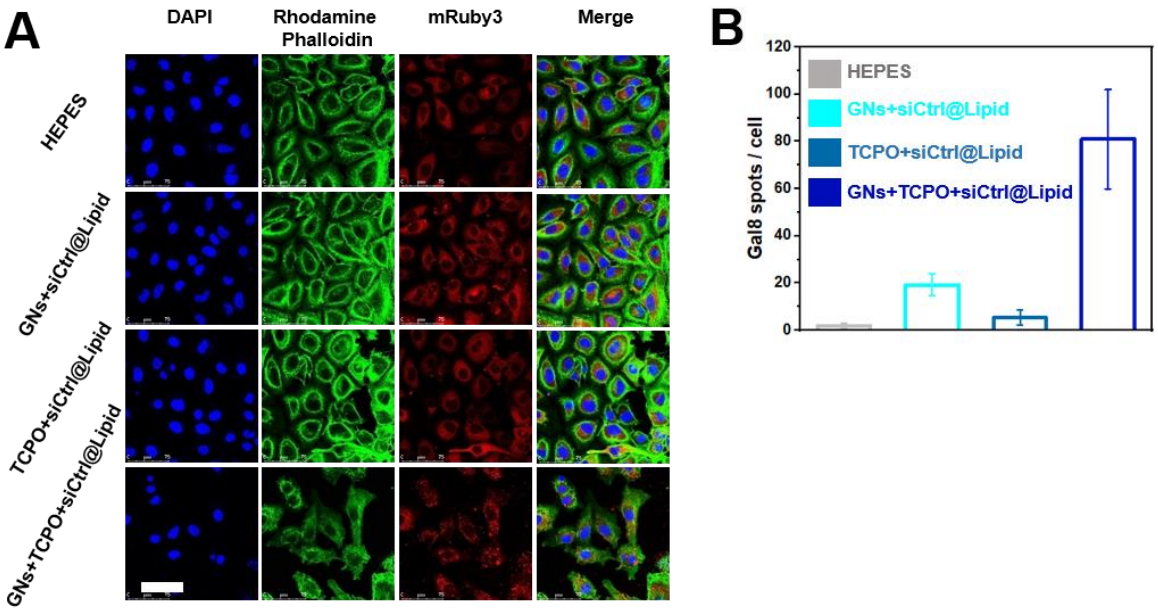

Figure 19. Endosomal escape and CET-correlated apoptosis elevation of lipopolyplexes. (A) Confocal microscopy images of HeLa cells stably expressing Gal8–mRuby3 fusion protein after treatment with for 12 h. Red, green, and blue fluorescence represent Gal8, actin filaments, and nucleus, respectively. Scale bar, 75 µm. (B) Quantitative analysis of Gal8 spots per cell for Figure 19A. The CLSM was performed by Miriam Höhn (Pharmaceutical Biotechnology, LMU München). HeLa cells expressing Gal8-mRuby3 fusion protein were established by Dr. Yi Lin (former PhD student at Pharmaceutical Biotechnology, LMU München).

3.1.7 Mechanism of cellular uptake

Based on the evidence that endocytosis of lipid-based nanoparticles is prerequisite for siRNA delivery and mRNA downregulation [134–136], we analyzed the endocytosis

pathway of our lipopolyplex. Three different pharmacological inhibitors were used according to the published literatures. Nystatin is responsible for inhibiting the caveolae-mediated pathway [137], sucrose is explored to down-regulate the clathrin-mediated pathway [138], amiloride as the Na^+/H^+ exchanger pump inhibitor is used for intervening the macropinocytosis [139]. Cells were preincubated with inhibitors for one hour, then the changes of GNs+siCy5@Lipid internalization were monitored by flow cytometry (**Figure 20A**). Downregulation of clathrin as well as caveolae-induced endocytosis did not significantly affect the cellular uptake of the lipopolyplexes. Encouragingly, amiloride regulated the macropinocytosis and led to a ~45% decrease in lipopolyplex uptake.

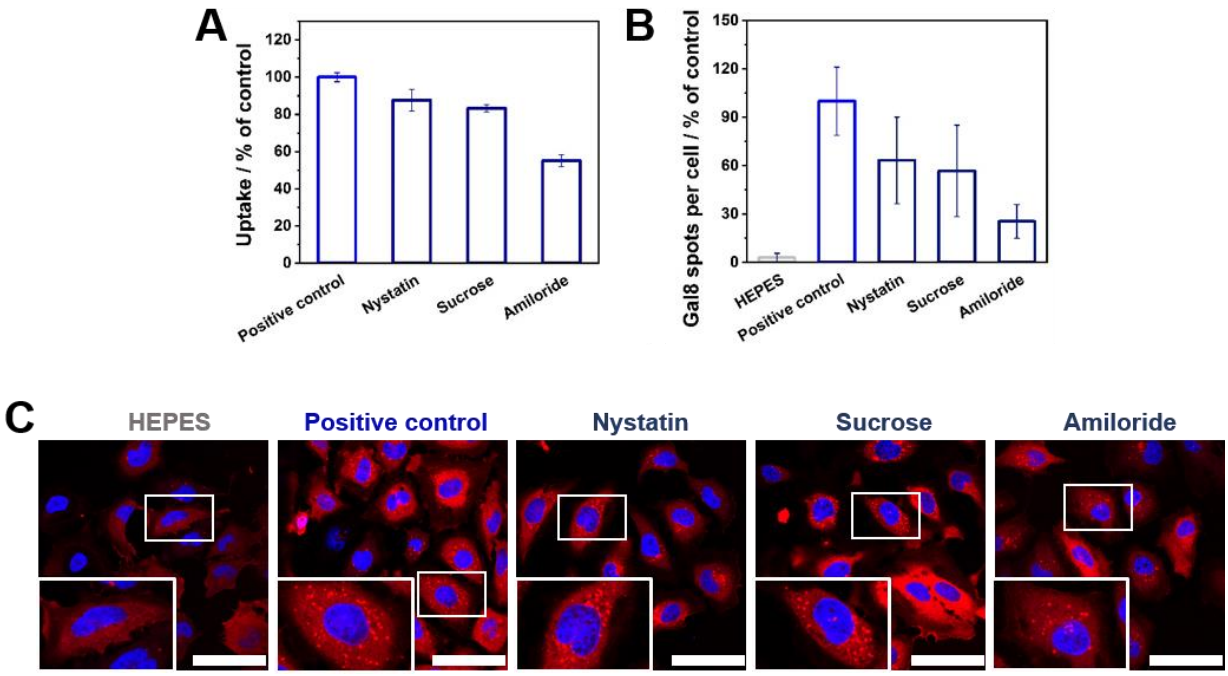

Figure 20. Cellular uptake mechanism of lipopolyplexes. (A) Quantification of Cy5 fluorescence intensity in KB cells treated with GNs+siRNA@Lipid and endocytosis inhibitors. (B) Quantitative analysis and (C) confocal microscopy images of HeLa-Gal8-mRuby3 cells after incubation with GNs+siRNA@Lipid and endocytosis inhibitors. The left lower corner presents the 2-fold magnification area indicated by the white squares. Scale bar, 75 µm. The CLSM was performed by Miriam Höhn (Pharmaceutical Biotechnology, LMU München). The HeLa cells expressing Gal8-mRuby3 fusion protein were established by Dr. Yi Lin (former PhD student at Pharmaceutical Biotechnology, LMU München).

According to this finding, we further investigated whether downregulating the endocytosis of lipopolyplex could also induce less endosomal escape. Therefore, we evaluated the endosomal escape behaviors of the lipopolyplex in HeLa-Gal8-mRuby3 cells with or without the inhibitors (**Figure 20B and C**). The GNs combined TCPO group (GNs+TCPO+siRNA@Lipid) and HEPES group were chosen as the positive control and the negative control, respectively. Notably, opposite to the inhibitor-free group, after being preincubated with inhibitors, the corresponding intracellular Gal8 spots also dramatically decreased. Specifically, more than 74% of Gal8 spots were blocked by amiloride, and the nystatin as well as sucrose treated groups showed little difference in endosomal escape regulation. Therefore, CET-induced ROS generation well potentiated endosomal disruption, implying that self-exciting chemical internalization could enhance cytosolic siRNA delivery.

3.1.8 Evaluation of CET-correlated anti-cancer effect

To further verify the enhanced gene silencing efficacy of the lipopolyplex, siEG5 was incorporated into the CET system. EG5 (also known as KSP or Kif11) is a motor protein involved in cellular mitosis. Silencing EG5 can block mitotic spindle apparatus organization and result in cell cycle arrest in the G2/M stage, initiating tumor cellular apoptosis program (**Figure 21A**) [139,140]. Cellular toxicity was assessed in advance *via* standard MTT assay, and no obvious cytotoxicity was induced by introducing siCtrl into the CET system (**Figure 21B**). In contrast, after changing siCtrl into siEG5, significant cell death was observed in a concentration-dependent behavior. Notably, we noticed a ~91% reduction in cell viability after co-incubation with GNs+TCPO+siEG5@Lipid at 100 μg mL^{-1} GNs and 250 ng siRNA doses. To further confirm this outcome, KB cells were analyzed by flow cytometry with fluorescent probes after the same treatment. Cells treated with GNs+TCPO+siEG5@Lipid exhibited an enhanced apoptosis ratio (~59%) compared with single chemotherapy (~21%) or RNAi therapy (~22%) (**Figure 21C**). Our data strongly evidenced that CET-based chemotherapy synergized RNAi displayed enhanced apoptotic killing in KB cells compared to other single therapeutic modalities.

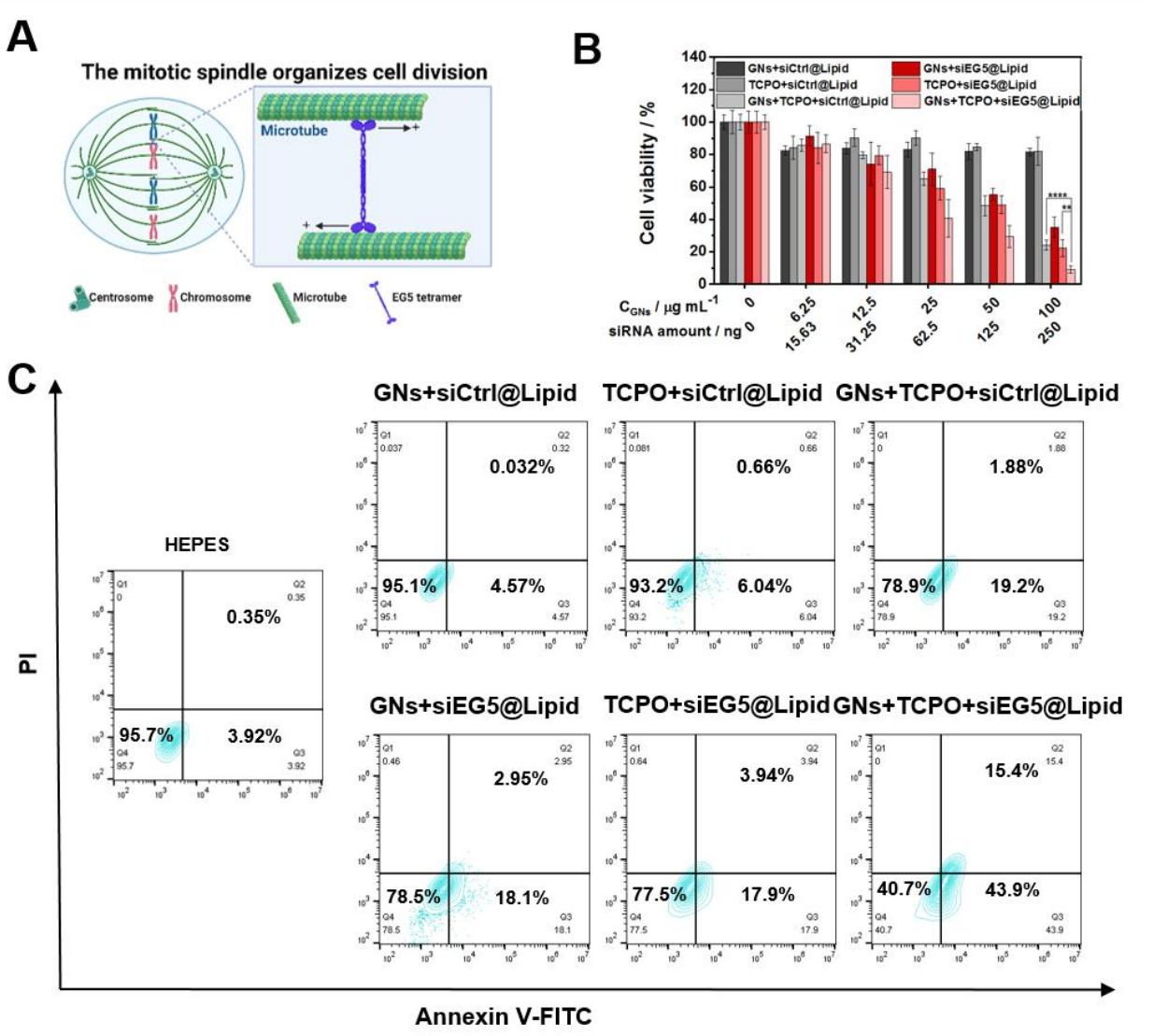

Figure 21. CET-correlated anticancer effect. (A) Schematic illustration of EG5 as a key motor protein involved in cellular mitosis, and its silencing with siEG5 can block centrosome separation and result in cell cycle arrest and apoptosis. (B) Cell viability of KB cells exposed to a series of concentrations of GNs+siCtrl@Lipid, TCPO+siCtrl@Lipid, GNs+TCPO+siCtrl@Lipid, GNs+siEG5@Lipid, TCPO+siEG5@Lipid, and GNs+TCPO+siEG5@Lipid for 48 h. (C) Annexin V-FITC/PI-based apoptosis analysis of KB cells using various treatments. **P* < 0.05, ***P* < 0.01, ****P* < 0.001, *****P* < 0.0001. Data are presented as mean ± SD (n = 5).

To confirm the biological effect of EG5 silencing, the cell cycle was evaluated with the help of PI. As shown in **Figure 22**, cells incubated without siEG5 were mainly distributed in the G1 stage (61% for HEPES group, 62% for GNs+siCtrl@Lipid group, 60% for

TCPO+siCtrl@Lipid group, 54% for GNs+TCPO@Lipid group). Oppositely, the ratio of G1 stage of siEG5-involved groups was obviously downregulated, and the population in G/M stage simultaneously increased (40% for GNs+siEG5@Lipid group, 43% for TCPO+siEG5@Lipid group, and 35% for GNs+TCPO+siEG5@Lipid group). Especially, the sub-G1 peak of cells incubated with GNs and TCPO combined groups both strongly increased with or without siEG5, indicating the cells started cellular apoptosis program under the action of ROS. And compared with the GNs+TCPO@Lipid group, the increased sub-G1 ratio was observed after integrating siEG5, suggesting a consequence of ROS-enhanced EG5 gene silencing.

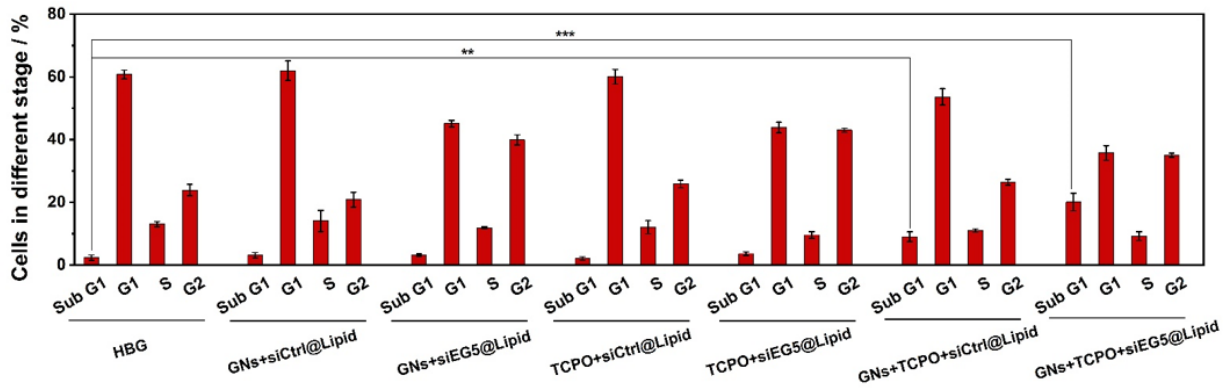

Figure 22. PI-mediated cell cycle evaluation of KB cells using various treatments. **P* < 0.05, ***P* < 0.01, ****P* < 0.001, *****P* < 0.0001. Data are presented as mean ± SD (n = 5).

3.2 Dual effect by CET enhanced siRNA LNPs: ROS-triggered tumor cell killing aggravated by Nrf2 gene silencing

Section 3.2 has been adapted from: Fengrong Zhang, Tobias Burghardt, Miriam Höhn, and Ernst Wagner*. Dual Effect by Chemical Electron Transfer Enhanced siRNA LNPs: ROS-Triggered Tumor Cell Killing Aggravated by Nrf2 Gene Silencing, Pharmaceutics, 2024. 16, 779.*

LNPs, with their core component consisting of cationic or ionizable lipids, are employed to package negatively charged nucleic acids [141–145]. Ionizable lipids containing secondary and/or tertiary amines are advantageous due to chemical architecture flexibility, providing endosomal pH-specific responsiveness [146–149]. Specifically, their acidic-switchable structure provides protonation-deprotonation capabilities during the preparation process, collaborating with other constituents to shape amorphous cores [150–152]. Importantly, facilitating the nucleic acid transfer into the cytosol is another crucial mission of ionizable lipids, avoiding the fate of degradation in lysosomal/endosomal acidic environments [110,153,154].

Mechanistic studies aimed at elucidating the endosomal escape of ionizable LNPs have been proposed, mainly membrane fusion as well as phospholipid flip-caused non-lamellar phase change and proton sponge effect [155–159]. The initial membrane destabilization in this process relies on endosomal acidification and involves a combination of positive-charged lipids with negatively charged host phospholipids [160]. Notably, pH-specific endosomal action avoids direct damage to the cytosolic membrane, thus minimizing cytotoxic side effects. Researchers have adopted numerous strategies to enhance nucleic acid cytoplasmic transfer [109,161–163]. Despite the clinical success of LNPs with siRNA and messenger RNA (mRNA) transfer, the efficiency of endosomal escape remains suboptimal, with success rates observed at only 1−2% [38]. Application of higher therapeutic doses carries the risk of side effects [126,164,165].

One alternative option to improve endosomal escape is the incorporation of sensitizers into nanovehicles that respond to specific external triggers, such as photo/sono energy, adjustably facilitating the destabilization of the vehicle and endosomal target membranes,

inducing cytoplasmic transfer [79,84,87,115,166–170]. For example, researchers reported on a porphyrin-LNP that enabled NIR light-induced siRNA endosomal release [170]. Such a photochemically triggered cytosolic delivery is suitable for superficial tissues that can be specifically addressed by light. Recently, we explored CET-assisted RNAi as an alternative to photochemical internalization, which successfully generated ROS without external triggers [171]. TCPO and GNs were employed as CET donor and acceptor, respectively. With the assistance of a donor and H_2O_2, the acceptor is activated, generating $^1O_2$ to disrupt endosomes and release siRNA formulated as lipopolyplexes into cytosol.

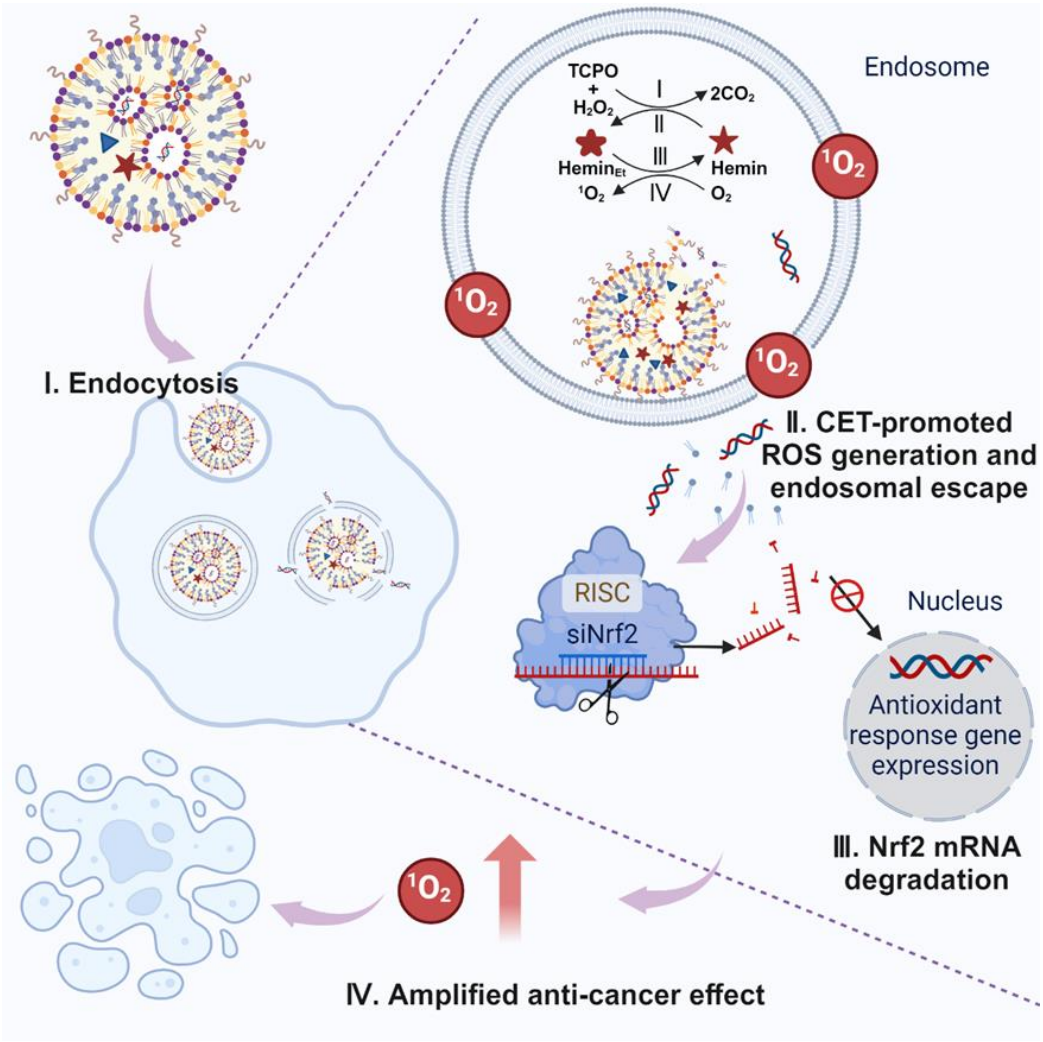

Scheme 3. Illustrations for CET-induced siRNA endosomal escape and siNrf2-aggravated ROS cancer cell killing.

Here, for the first time, we applied CET as an external trigger for the enhanced cytosolic delivery of LNPs-loaded with siRNA (siRNA@Lipid) and enhanced ROS-triggered tumor cell killing. For this purpose, novel LNP compositions were packaged with siRNA and various doses of TCPO and hemin as CET donor and acceptor, respectively (**Scheme 3**). Given the excellent capacity of hemin and TCPO to induce ROS production in cancer cells, we sought to enhance gene silencing *via* endosomal membrane lipid peroxidation: the CET effect would induce the endosomal accumulation of ROS, accelerating the transfer of the gene sequence to the cytoplasm. Effective silencing of gene targets at low siRNA doses demonstrated a LNP-integrating CET enhancing effect. Simultaneously, antitumoral siRNA extended the lifetime of ROS by silencing the oxidative stress protein, Nrf2, promoting cancer cell killing efficiency.

3.2.1 Formulation and characterization of CET-based LNPs

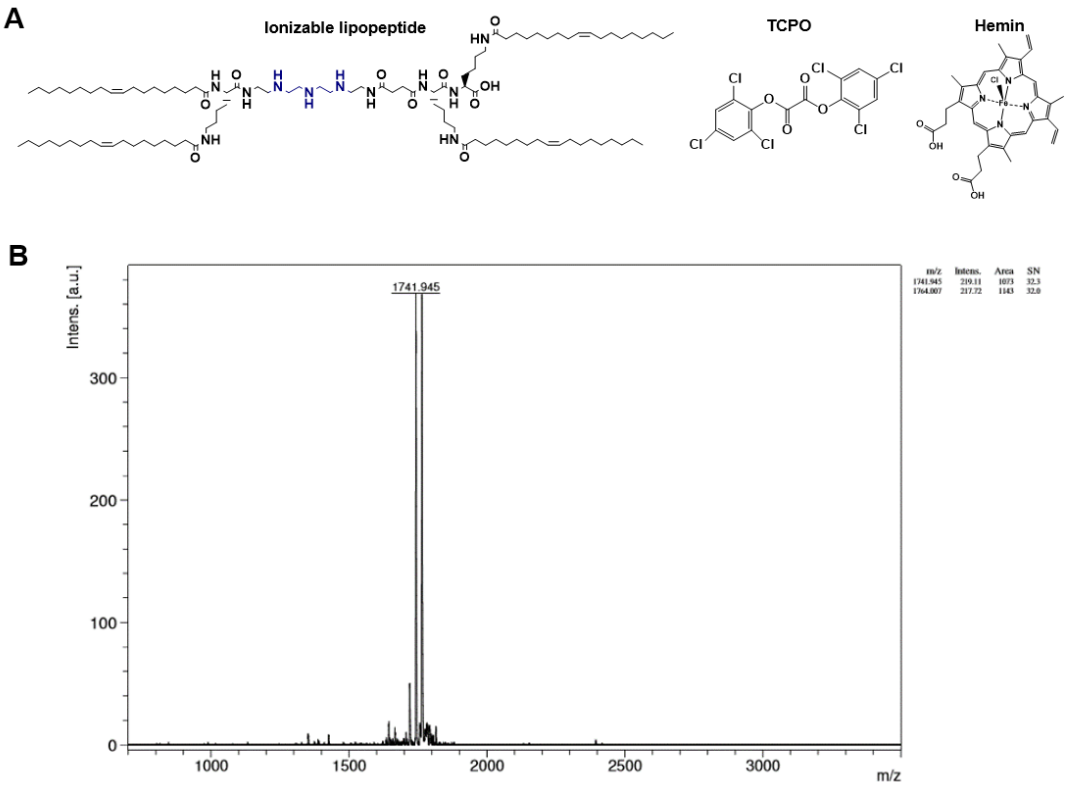

Figure 23. Design and preparation of LNPs. (A) Chemical structures of the ionizable lipopeptide TOTL-Stp, TCPO, and hemin used in the LNP formulation. (B) Chemical structure and MALDI-MS spectrum of the ionizable lipopeptide TOTL-Stp. Molecular weight:1730.48. $[M+NH_4]^+$ found

1741.95 and $[M+K]^+$ found 1764.00. TOTL-Stp was synthesized by Tobias Burghardt (PhD student at Pharmaceutical Biotechnology LMU München).

The ionizable lipopeptide TOTL-Stp provides siRNA binding and endosomal escape capabilities through its three cationizable secondary amines (**Figure 23A**). TOTL-Stp had been synthesized by SPPS analogously as previously reported (**Figure 23B**) [30,101,102]. The four oleic acid tails are incorporated in a U-shaped sequence $K(OleA)_2$-Stp-K(OleA)-K(OleA)-OH *via* bridging lysines and promote LNP stabilization through hydrophobic interactions and provide a fusogenic ability with the endosomal host membrane.

LNPs were prepared using the standard solvent-exchange deposition method. In detail, helper lipids (cholesterol and phospholipid), PEG lipid, ionizable lipopeptide, TCPO, and hemin were dissolved in an ethanol and DMSO-containing organic solvent, and siRNA was dispersed in acidic citrate buffer. The TCPO and hemin were encapsulated in the hydrophobic interlayer by rapidly adding the aqueous solution containing siRNA (**Figure 24A and B**). Both electrostatic and hydrophobic interactions guided the assembly process.

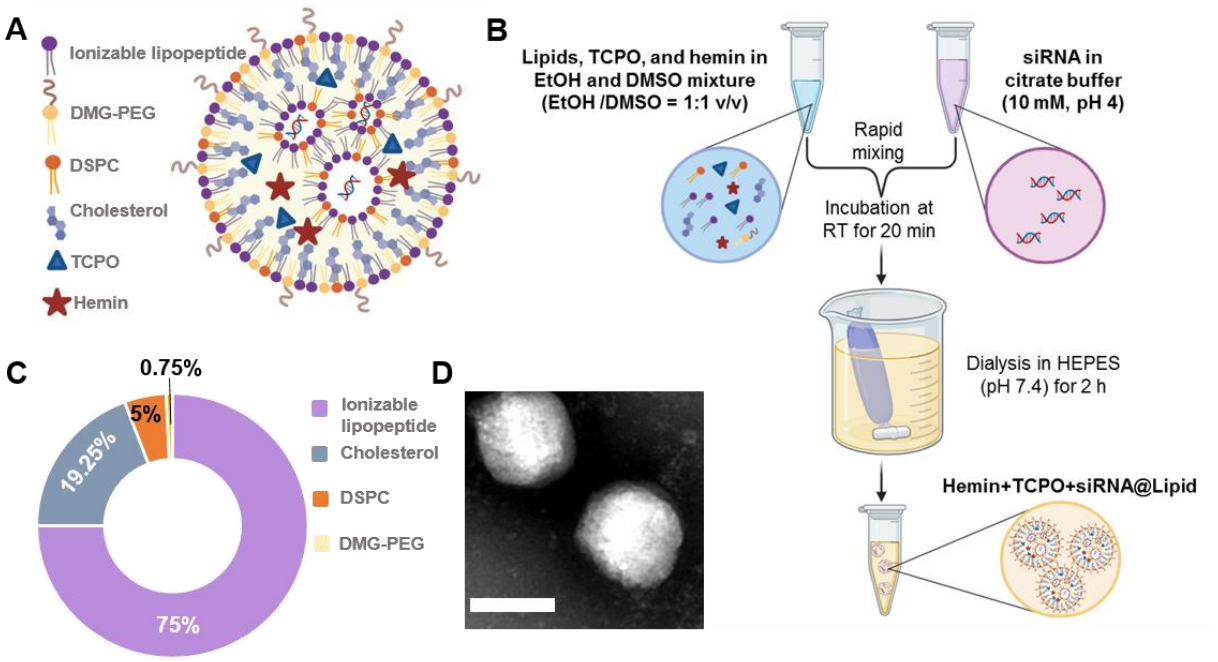

Figure 24. (A) Schematic representation of the compounds in the CET-based LNP. (B) Illustration of the generation of CET-based LNPs via rapid mixing. Hemin and TCPO for the CET effect were dissolved in DMSO, and lipids were dissolved in ethanol. The ionizable lipopeptide enables siRNA

encapsulation through its positive charge at the low pH of the citrate buffer (pH 4). (C) The molar ratio of each compound in the top-performing LNP. (D) TEM image of LNPs contained hemin and TCPO in 20 mM HEPES buffer (pH 7.4). The N/(P+C) ratio was 9, the siRNA amount was 1 µg, the hemin amount was 1.3 µg, and the TCPO amount was 80 µg. The molar ratio of different lipids was 75/19.25/5/0.75 (ionizable lipopeptide/cholesterol/phospholipid/DMG-PEG). Scale bar is 100 nm.

The top-performing formulation was derived from the LNP formulation of Onpattro®, increasing the ionizable lipopeptide content in accordance with the N/P ratio while maintaining the other components constant. The best formulation had a N/P or N/(P+C) ratio of 9 and a molar ratio of 75/19.25/5/0.75 (ionizable lipopeptide/cholesterol/ phospholipid/PEG-DMG) (**Figure 24C**). Specifically, N represents the molar amount of ionizable nitrogen, P denotes the molar amount of phosphate group, and C corresponds to the molar amount of carboxyl group derived from the anionic hemin content. TEM revealed the morphological characteristics of the nanoparticles loaded with hemin and TCPO, exhibiting a relatively regular and spherical shape (**Figure 24D**).

3.2.2 Characterization of CET-based system for ROS generation

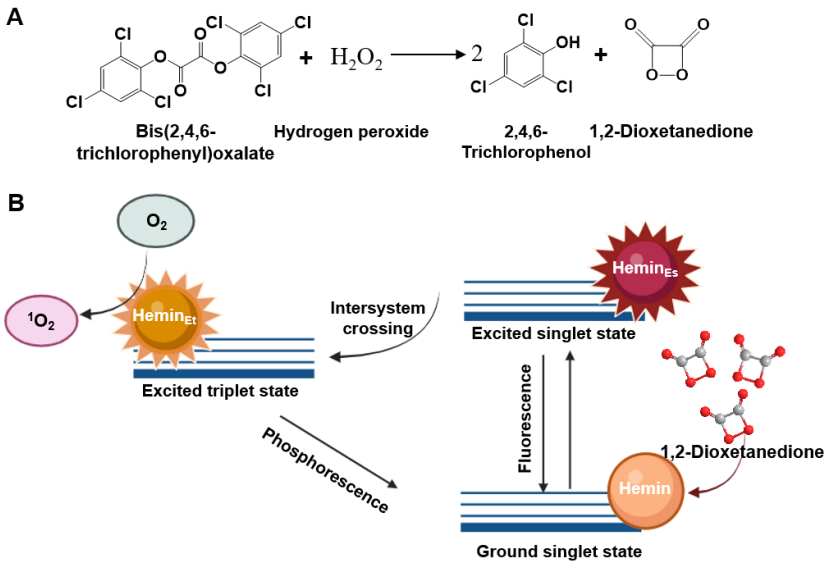

Figure 25. Illustration depicting (A) the chemical reaction of TCPO and H_2O_2 and (B) the excitation of hemin from the ground singlet state to the excited singlet state through energy transfer with 1,2-

dioxetanedione. Subsequently, through intersystem crossing, it transitions to an excited triplet state capable of reacting with oxygen to generate $^1O_2$.

ROS generation is the prerequisite for the CET effect-enhanced endosomal escape of siRNA. In the current light-free CET system, the lipophilic oxalate derivative TCPO and the acceptor hemin co-localize in the hydrophobic section, ensuring an energy transfer distance of less than 10 nm. As displayed in **Figure 25**, the reaction between TCPO and H_2O_2 generates an energy-rich dioxetanedione. The intermediate excites hemin from the ground singlet state to the excited singlet state through energy transfer rather than light energy. Subsequently, through intersystem crossing, an excited triplet state is formed that reacts with oxygen to produce $^1O_2$.

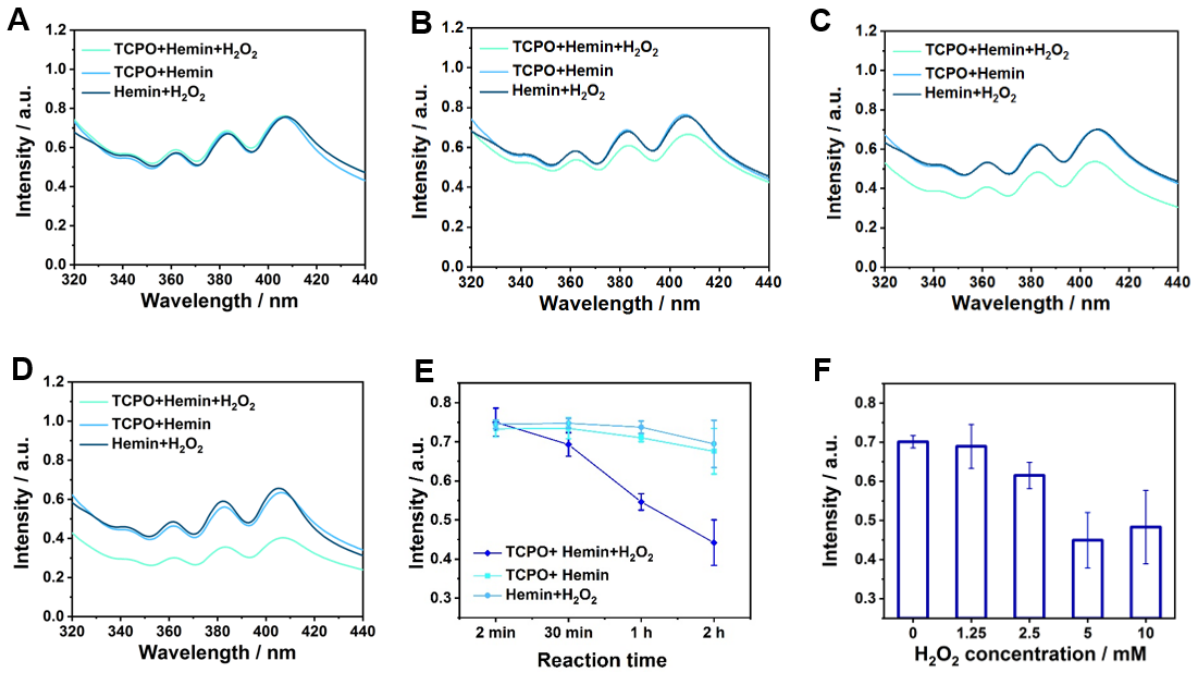

Figure 26. ROS-based degradation of DPA, spectra under different conditions (A) T = 2 min, (B) T = 30 min, (C) T = 1 h, and (D) T = 2 h. (E) UV–vis absorption intensity of DPA at 383 nm over reaction time. The concentrations of DPA, TCPO, and hemin used in DPA degradation assay were 15 μg mL^{-1}, 0.17 mg mL^{-1}, and 0.78 μg mL^{-1}, respectively. (F) Ultraviolet–visible absorption intensity of DPA for LNPs at 383 nm under varying concentrations of H_2O_2. Reaction time was 2 h. The concentrations of DPA, TCPO, and hemin used in the DPA degradation assay were 15 μg mL^{-1}, 0.17 mg mL^{-1}, and 0.78 μg mL^{-1}, respectively.

For the analysis of $^1O_2$, DPA, characterized by three distinctive absorption peaks, was adopted. Notably, in the CET group, the signal of DPA significantly decreased to 72% after 1 h and further dropped to 59% within 2 h. In comparison, without the assistance of H_2O_2 or TCPO, the retention rate was still higher than 90% after 2 h (**Figure 26A-E**). Furthermore, H_2O_2-dependent DPA oxidation was further evidenced by elevating H_2O_2 concentration from 0 to 5 mM (**Figure 26F**). These findings strongly evidenced the excellent ability of CET-based light-free system in inducing ROS production through energy transfer.

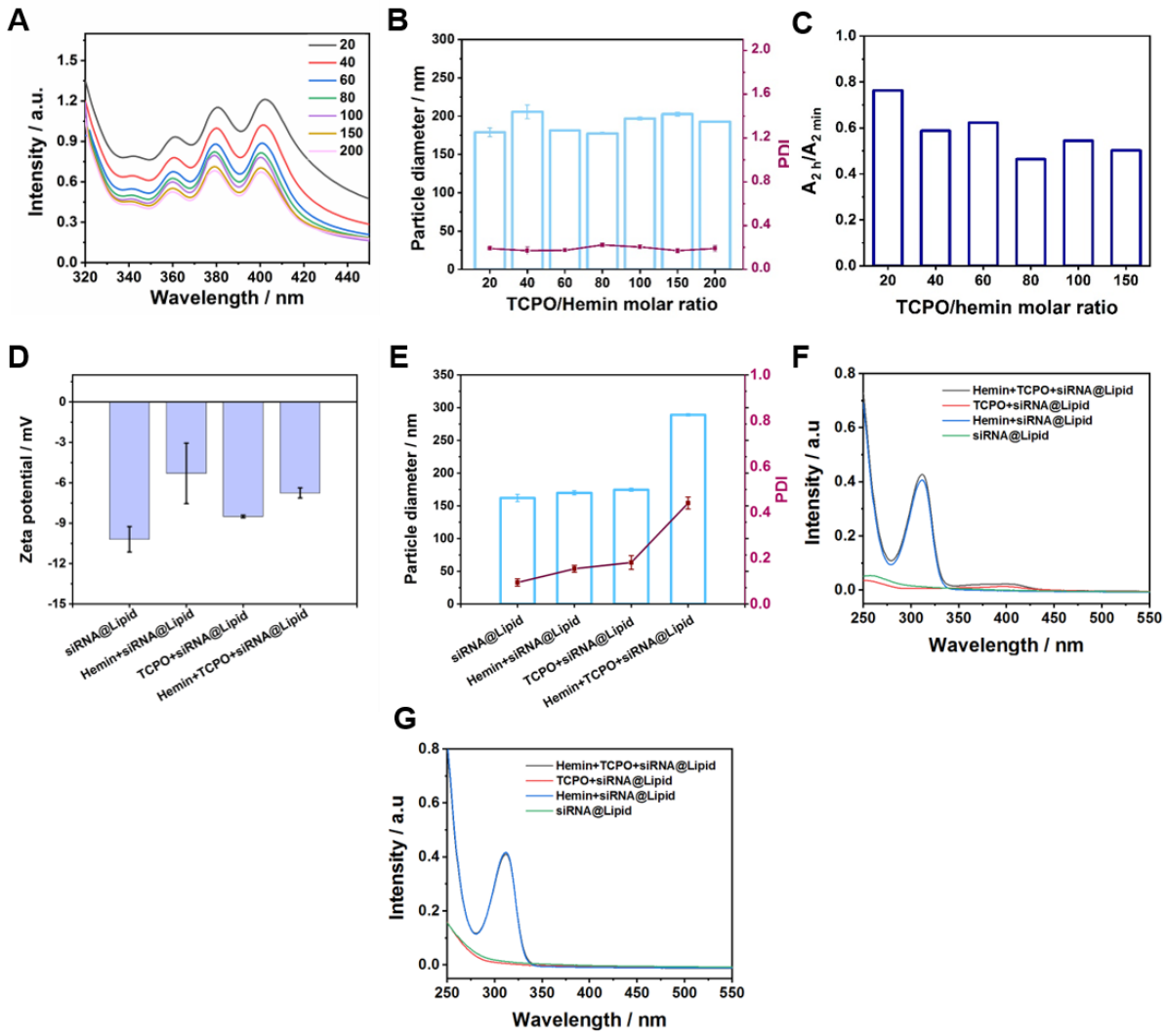

Figure 27. (A) Degradation spectra of DPA after adding different LNPs with a range of TCPO/hemin molar ratios. The concentration of H_2O_2 adopted was 5 mM. T = 2 h. (B) Size distributions and PDI of Hemin+TCPO+siRNA@Lipid with different TCPO/hemin ratio. (C)

Absorption intensity ratio of DPA at 383 nm between reaction times of 2 h and 2 min for different LNPs. The N/(P+C) ratio was 3, the siRNA amount was 1 μg, and the TCPO amount was 80 μg. The molar ratio of different lipids was 50/38.5/10/1.5 (ionizable lipopeptide/cholesterol/phospholipid/DMG-PEG). (D) Size distributions, PDI and (E) zeta potentials of different formulations. The N/(P+C) ratio was 9, the siRNA amount was 1 μg, the hemin amount was 1.3 μg, and the TCPO amount was 80 μg. UV–vis light absorption spectra of Hemin+TCPO+siRNA@Lipid, TCPO+siRNA@Lipid, Hemin+siRNA@Lipid, and siRNA@Lipid (F) before and (G) after adding H_2O_2.

Building on the foundation of the CET effect, we expanded the system by integrating siRNA, cholesterol, and lipids, thereby creating the CET-based LNPs (Hemin+TCPO+siRNA@Lipid). Since ROS generation can vary with the molar ratio of TCPO/hemin, we optimized the DPA signal of various formulations using different molar ratios (**Figure 27A**). The average hydrodynamic sizes of the formulations measured by DLS exhibited minimal variation (**Figure 27B**). Importantly, the monodispersity of all formulations was well proved by PDI values, all around 0.2.

The optimal TCPO/hemin molar ratio, determined to be 80, was utilized in the following experiments (**Figure 27C**). In addition, DLS showed that the ionizable lipid composition and siRNA formed LNPs, with or without TCPO and hemin, holding hydrodynamic sizes ranging from 162 nm and 289 nm and ζ-potentials among –5 mV and –10 mV (**Figure 27D and E**). In the case of the CET reaction, it was observed that the UV–vis absorption of TCPO at 400 nm disappeared upon reaction with H_2O_2, which can be attributed to the decomposition of TCPO (**Figure 27F and G**).

3.2.3 Optimization of LNPs for siRNA loading and gene silencing

An elevated N/P ratio in LNP formulations may contribute to higher gene silencing efficacy but also amplifies potential toxicity issues. To address these conflicting requirements, we optimized the formulation by selectively improving the ionizable lipid content according to the N/P ratio, and keeping the other components constant. As indicated in **Table 2**, the optimized LNPs possess ionizable lipopeptide ratios ranging from 60–86%, with the corresponding ratio of PEG lipid reduced from 1.2 to 0.4%, significantly lower than that of typical LNPs (1.5%).

Table 2. Molar ratio of each compound for LNPs with different N/P ratios.

	N/P	Molar ratio of ionizable lipopeptide/cholesterol/DSPC/PEG-DMG
Initial formulation	3.0 to 18	50/38.5/10/1.5 mol%
Optimized lipopeptide formulation	4.5	60/30.8/8/1.2 mol%
	9	75/19.25/5/0.75 mol%
	18	85.71/11/2.86/0.43 mol%

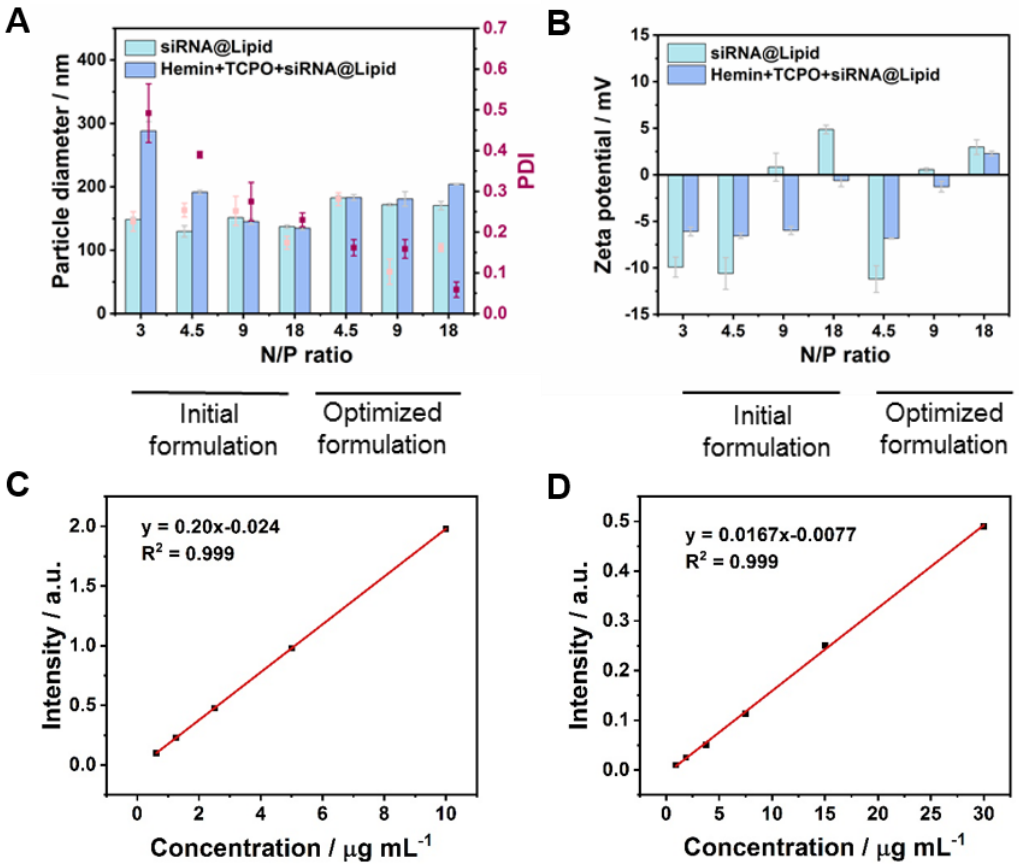

Figure 28. Optimization of LNPs. (A) Size distribution, PDI, and (B) zeta potentials of initial formulations and optimized formulations at different N/P ratios. The siRNA amount was 1 μg, the hemin amount was 1.3 μg, and the TCPO amount was 80 μg. The siRNA@Lipid group was formulated without hemin and TCPO addition. Curve fitting for (C) hemin and (D) TCPO absorption.

In general, all LNPs exhibited a favorable size range of 130–183 nm and PDI range of 0.10–0.28 without hemin and TCPO (**Figure 28A**). Adjusting the N/P ratio had a negligible impact on the hydrodynamic size and dispersion of optimized LNPs. The ζ-potentials of optimized LNPs shifted to positive at N/P 9 (**Figure 28B**). In contrast, after incorporating CET components, the size of siRNA@Lipid at N/P 3 increased to 288 nm; and low dispersibility in the HEPES buffer was observed. Notably, for the optimized formulations, encapsulating hemin and TCPO led to a slight increase in size, and their monodispersity was maintained. The loading efficiency of the TCPO and hemin were calculated. Specifically, the formulation with N/P 9 was the top performer, displaying encapsulation efficiencies >60% for hemin and >20% for TCPO (**Figure 28C, D, and Table 3**).

Table 3. Loading efficiencies of hemin and TCPO in optimized CET LNPs with N/P ratios of 3.0, 4.5, 9, and 18.

N/(P+C)	Hemin loading efficiency	TCPO loading efficiency
3	58.2	14.2
4.5	53.1	12.1
9	62.8	24.2
18	57.6	23.0

To investigate the siRNA binding ability of CET-enhanced LNPs, a gel shift assay was performed using a 2.5% agarose gel (**Figure 29A**). The binding was significantly potentiated when the fraction of ionizable lipopeptide was increased in LNPs. The results indicated the specific elevation in ionizable lipopeptide content substantially enhanced siRNA binding efficiency. Particularly, when the N/P ratio of the optimized formulation reached or exceeded 9, superior siRNA binding capabilities were observed. In addition, the storage stability of the new formulation was evaluated. The formulations showed no considerable change in size over one week at 4 ^{o}C (**Figure 29B**). Oppositely, a substantial increase in size and PDI was recognized upon introducing the H_2O_2, and this phenomenon was further amplified with prolonged incubation at 37 ^{o}C (**Figure 29C and D**).

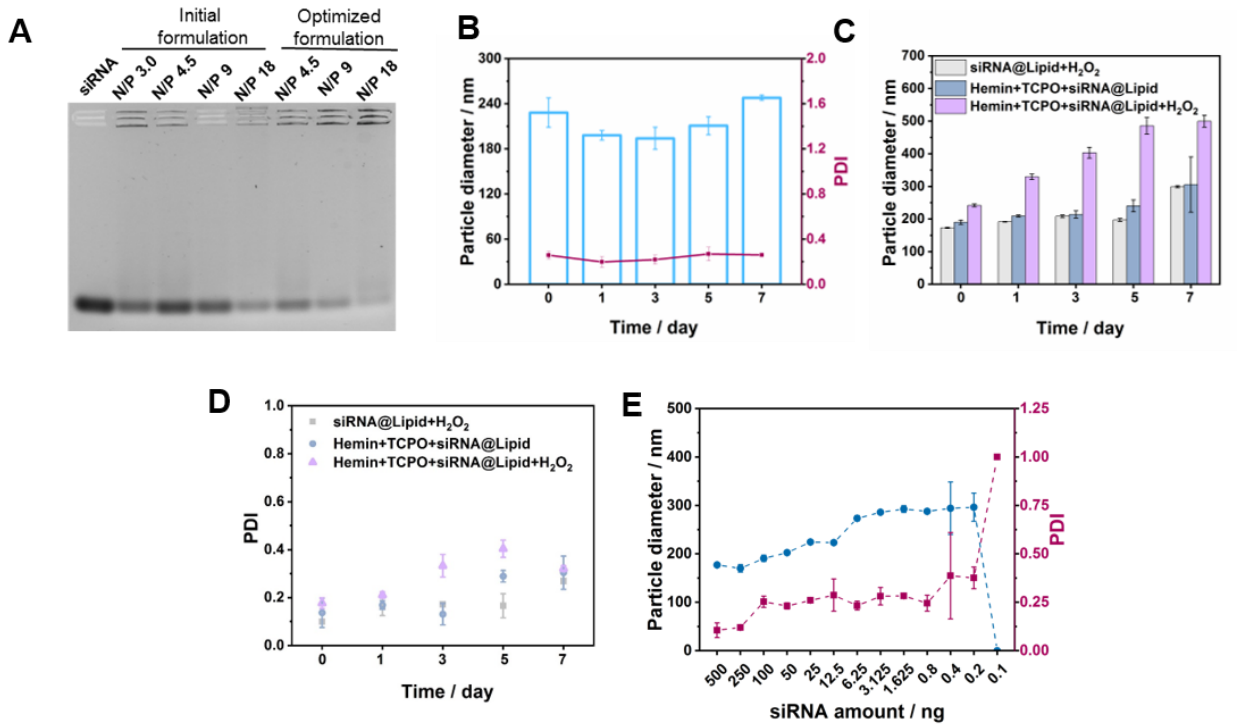

Figure 29. (A) siRNA binding assay of initial formulations and optimized formulations at different N/P ratios. The siRNA@Lipid group was formulated without hemin and TCPO addition. For the siRNA binding assay, all formulations were CET LNPs (Hemin+TCPO+siRNA@Lipid). The gel electrophoresis conditions were: 2.5% agarose gel, 100 V, running time was 60 min. The siRNA amount was 100 ng, the hemin amount was 0.13 µg, and the TCPO amount was 8 µg. (B) Stability assay of CET LNPs after storing at 4 °C for one week. The siRNA amount was 1 µg, the hemin amount was 1.3 µg, and the TCPO amount was 80 µg. (C) Size and (D) PDI of siRNA@Lipid and Hemin+TCPO+siRNA@Lipid with or without the addition of H_2O_2. LNPs were incubated in PBS (pH 7.4) at 37 °C for 1 week. The siRNA amount was 1 µg, the hemin amount was 1.3 µg, and the TCPO amount was 80 µg. (E) Effect of dose dilution on the CET LNPs' size and PDI measured by DLS.

The CET-dependent size alteration of LNPs likely corresponds to CO_2 generation within the core and rearrangement events that might be induced by lipid peroxidation. Previous researches have demonstrated that the double bonds in phospholipid can be oxidized in the presence of $^1O_2$ [59,172]. Next, we tested the influence of dilution on integrity. The nanoparticles were prepared with a high siRNA amount of 500 ng, followed by serial dilution to lower concentrations. Encouragingly, the formulations exhibited excellent dilution stability at relatively low doses (**Figure 29E**).

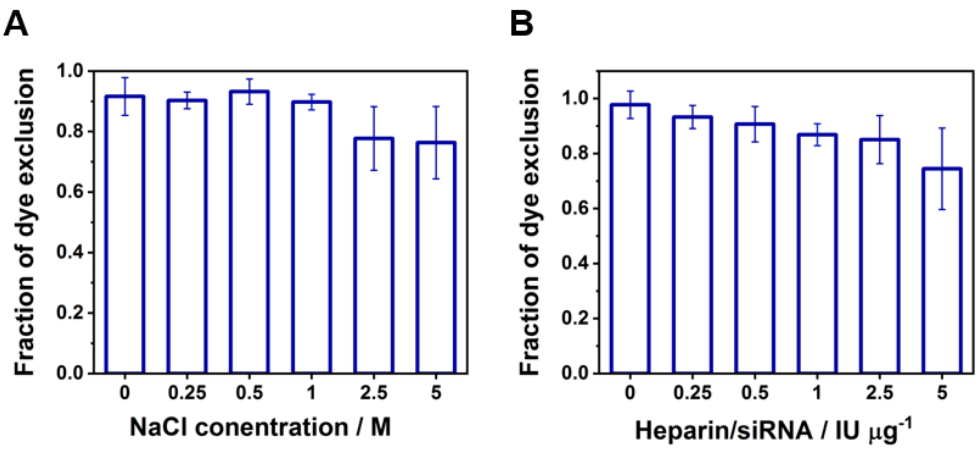

Figure 30. CET-enhanced LNPs stability against varying concentrations of (A) NaCl and (B) heparin. Ribogreen was utilized to detect free siRNA. The formulations contained siCtrl 1 µg, TCPO 80 µg, and hemin 1.3 µg.

It has been reported that the hydrophilicity of PEG-lipid contributes to the steric stabilization of LNP, ensuring excellent stability even under high ionic strength conditions. So, the RNA leakage assay of CET-enhanced LNPs was investigated following exposure to heparin and sodium chloride at series concentrations (**Figure 30**). At relatively high sodium chloride concentration (1.25 M), LNPs exhibited robust encapsulation of siRNA. With increased ionic strength, slightly stronger Ribogreen fluorescence was observed, indicating that some siRNA was released from dissociated LNPs. This observation is consistent with the trends in the heparin competition assay.

Before we explored the CET-enhanced gene silencing, the efficiency of CET free LNPs was first analyzed after treatment with serial concentrations of LNPs for 48 h (**Figure 31A**). The transfections were carried out in KB/eGFPLuc cells, which express eGFPLuc fusion protein. Target gene silencing was assessed by measuring luciferase activity. The MC3 LNP formulation dosed at 500 ng siRNA/well was selected as positive control. Both the initial and the optimized CET-free LNPs effectively silenced eGFPLuc expression at siGFP concentrations varied from 12.5 to 100 ng per well. Conversely, the siCtrl groups of the corresponding initial formulations exhibited noticeable intrinsic cytotoxicity. Specifically, in the range of N/P ratios from 4.5 to 18, the luciferase activity of LNPs exhibited gradually decreased with the escalating dose of siCtrl in LNPs. Encouragingly,

all optimized LNPs loaded with siCtrl showed nearly no reduction of luciferase activity; meanwhile, the excellent gene silencing capability was validated, with all formulations containing siGFP at 50 ng mediated more than 90% gene silencing efficiency. By comparison, the MC3 LNPs exhibited the same efficiency with a 10-fold higher siRNA amount. Similar conclusions were also demonstrated in DU145/eGFPLuc and N2a/eGFPLuc cells (**Figure 31B**). Considering both the CET effect and RNAi efficacy, LNP with N/P 9 was identified as the top performer and utilized in the subsequent experiments. Its siRNA encapsulation efficiency was determined to be 98% by Ribogreen assay.

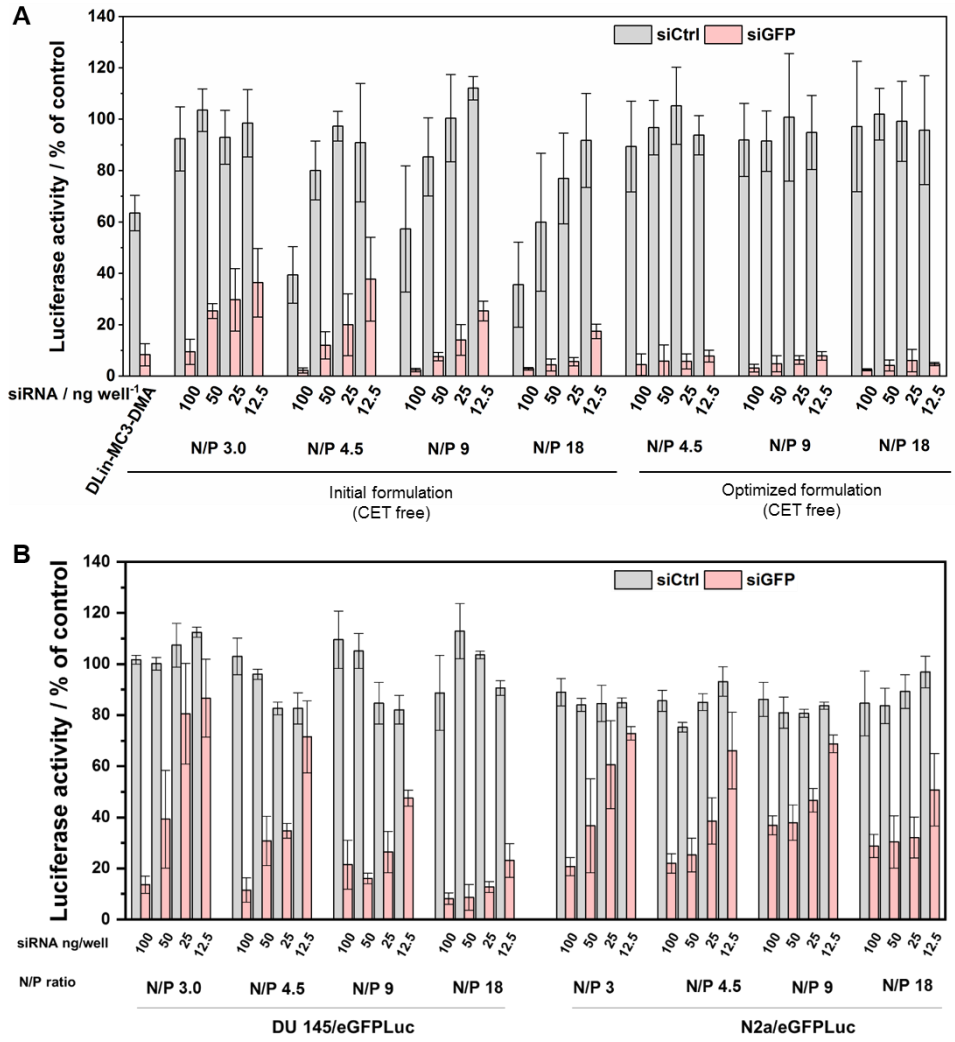

Figure 31. (A) Gene silencing efficiency of KB/eGFPLuc cells treated with various CET free LNPs (siRNA@Lipid) at siRNA dose of 12.5, 25, 50, and 100 ng for 48 h. DLin-MC3-DMA was formulated as LNPs at N/P ratio of 3 and a siRNA dose of 500 ng well^{-1}. (B) Gene silencing

efficiency in DU145/eGFPLuc and N2a/eGFPLuc cells treated with LNPs at siRNA amounts of 12.5, 25, 50, and 100 ng for 48 h. Luciferase activity was normalized to cells without any treatment.

3.2.4 Evaluation of cellular uptake

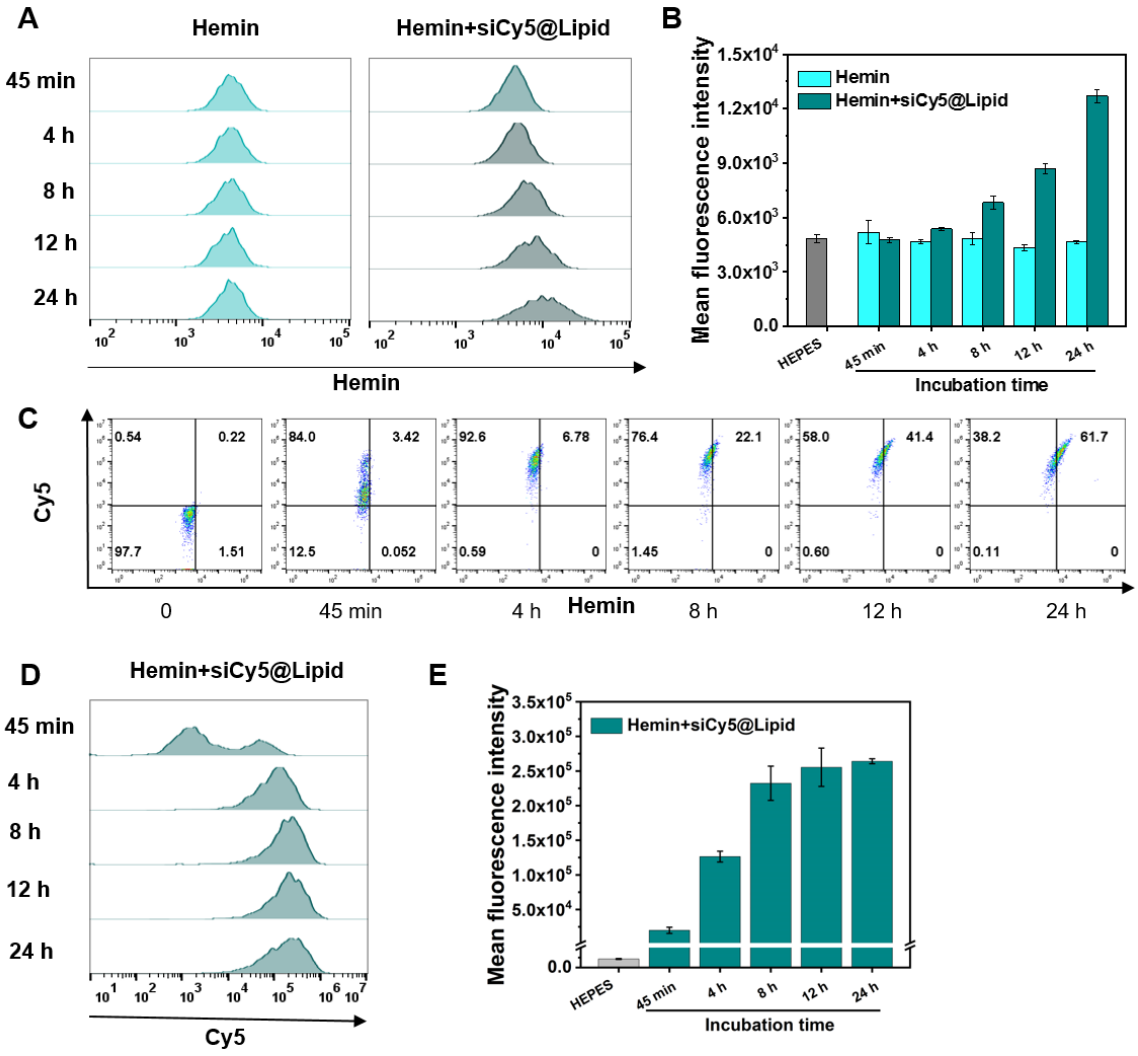

Figure 32. Endocytosis production assays. (A) Investigation of hemin and Hemin+siCy5@Lipid cellular internalization after a series of incubation times. (B) Quantitative analysis of cellular hemin fluorescence intensity after different incubation times. (C) Hemin/Cy5-based cellular internalization assay in cancer cells following treatment with Hemin+siCy5@Lipid. The nanocarrier solution contained 100 ng siCy5 as well as 4 µg hemin with an N/(P+C) ratio of 9. (D) Cellular uptake study of Hemin+siCy5@Lipid after 45 min, 4 h, 8 h, 12 h, and 24 h of incubation. The 20% siRNA was labelled with Cy5. (E) Quantitative data of cellular Cy5 fluorescence intensity after varying incubation time.

Excellent RNAi primarily depends on effective cellular internalization, and therefore, the endocytosis of Hemin+siRNA@Lipid was explored using Cy5-labeled siRNA. The results showed that no significant signal shift observed for naked hemin (**Figure 32A**). In contrast, the uptake of the Hemin+siRNA@Lipid was gradually improved after incubation for 8 h (**Figure 32B**). Similarly, the enhanced cytosolic delivery of siRNA through a lipid encapsulation strategy was demonstrated in **Figure 32C, D and E**. However, the hemin signal from the encapsulated group was notably lower than that of siCy5, which was attributable to aggregation-induced quenching of PSs.

3.2.5 Mechanism of cellular uptake

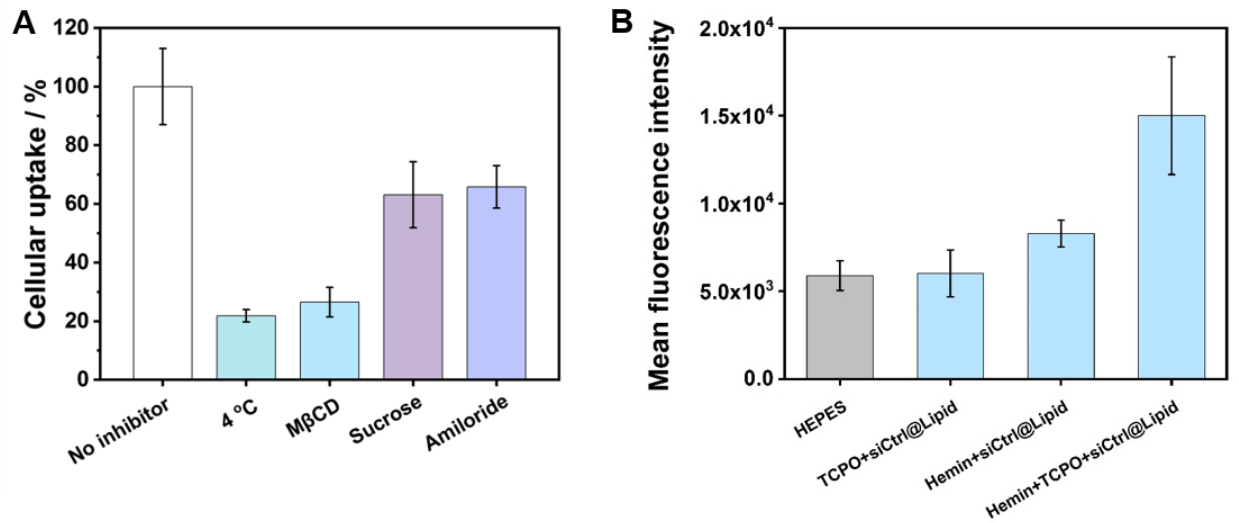

Figure 33. (A) Endocytosis pathway study of LNP with different inhibitors. 4 °C: energy-dependent endocytosis; MβCD: lipid rafts/caveolae-mediated endocytosis; sucrose: clathrin-mediated endocytosis; amiloride: macropinocytosis. Incubation time was 4 h. Uptake was normalized to cells without inhibitor. (B) Assessment of ROS production in cells exposed to various formulations. Each formulation contained siCtrl 100 ng well^{-1}, TCPO 8 μg well^{-1}, and hemin 130 ng well^{-1}.

In an attempt to validate the internalization pathway of the LNP, three types of inhibitors and low temperature were adopted following literature protocols. At 4 °C, energy-dependent endocytosis is affected; MβCD can inhibit caveolae/lipid rafts-mediated endocytosis; sucrose is the clathrin-mediated pathway inhibitor; amiloride is utilized to interfere the Na^+/H^+ exchange pump in macropinocytosis [139,173,174]. As shown in

Figure 33A, low temperature and MβCD inhibited the cellular internalization of nanocarriers by 78 and 73%, respectively, demonstrating energy- and caveolae/lipid rafts-dependent endocytosis mechanisms. Based on the good cellular uptake, we further investigated the CET-based LNP-mediated cellular ROS generation (**Figure 33B**). In comparison to the HEPES group, a 1.5-fold increase in the fluorescent signal was observed in the CET group. As expected, the hemin in the hydrophobic interlayer was excited by the chemical energy through the CET donor, produced by TCPO and cellular H_2O_2 reaction.

3.2.6 Evaluation of CET effect through cell viability

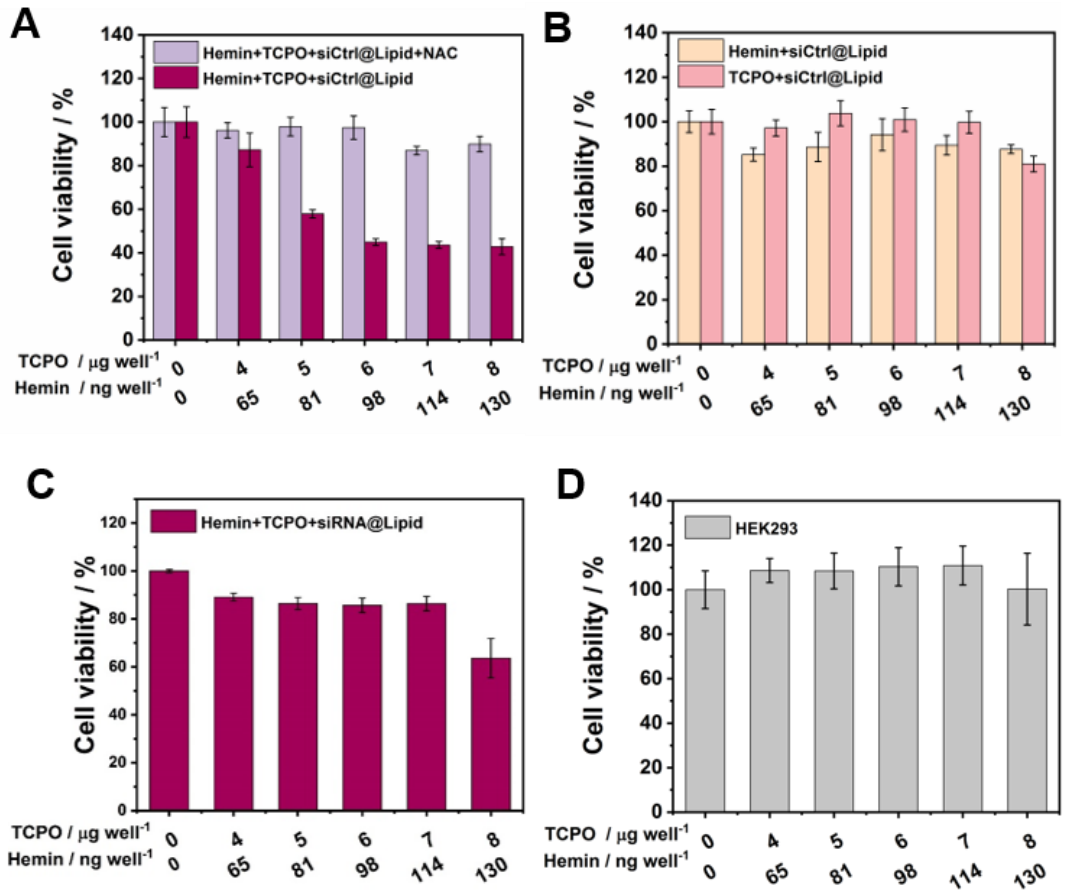

Figure 34. Cell viability, gene silencing, and endosomal escape assay of CET system. N/P and N/(P+C) ratios were 9. (A) KB cell viability after incubation with serial concentrations of Hemin+TCPO+siCtrl@Lipid with or without 3 mM NAC for 48 h. NAC was used as an antioxidant. (B) Cell cytotoxicity of single CET components. KB cells were incubated with LNPs for 48 h and

then evaluated using an MTT assay. (C) Cell viability of KB cells incubated with serial concentrations of Hemin+TCPO+siRNA@Lipid for 24 h. (D) Cytocompatibility of Hemin+TCPO+siRNA@Lipid in H_2O_2 low producing cells. Incubation time was 48 h.

The CET-triggered ROS generation depends on the dosage and the cell type, which not only enhances siRNA delivery by destabilizing endosomal membranes, but also induces cell killing. To prove the CET capability for cancer cell elimination through intracellular ROS, the cell metabolism activity was measured with or without addition of an antioxidant (NAC). Consistent with expectations, in the absence of NAC, the cell viability exhibited a concentration-dependent reduction pattern in the presence of CET components. Notably, co-incubation with Hemin+TCPO+siRNA@Lipid for 48 h at doses of 6 μg well^{-1} TCPO and 96 ng well^{-1} hemin induced a ~55% reduction in cell viability. In contrast, after scavenging $^1O_2$ with NAC, cellular metabolic activity was considerably restored, with no obvious decrease observed (**Figure 34A**). Moreover, the potential cytotoxicity of individual contributors was also evaluated. Encouragingly, following a 48 h treatment of cells with Hemin+siRNA@Lipid or TCPO+siRNA@Lipid, the excellent biocompatibility of the CET fundamental elements was confirmed (**Figure 34B**). In addition, we demonstrated that the CET effect-mediated cancer cell killing was time-consuming process. With a shorter incubation time, less cell lethality was detected, indicating a gradual yield of cellular $^1O_2$ and sustained induction of cell apoptosis (**Figure 34C**). It has been demonstrated that cancer cells manifest metabolic alterations leading to notably elevated H_2O_2 levels in mitochondria (50-100 μM); the overproduced H_2O_2 takes responsibility for CET efficacy and specificity. HEK293, characterized by low H_2O_2 production, were employed to study the specificity of the CET system. Compared with KB cells, negligible non-selective effects were exhibited towards normal cells, even at a relatively high dose (**Figure 34D**).

3.2.7 Evaluation of CET effect for enhancing endosomal escape

As mentioned above, the produced ROS in the CET system is beneficial for improving gene silencing *via* endosomal membrane lipid peroxidation. To verify this hypothesis, we measured the RNAi efficacy of LNPs with or without the CET system. In the initial step, an MTT assay was conducted for low doses of hemin and TCPO to ensure no interference with cell viability (**Figure 35A**). Also, luciferase activity assays in KB/eGFPLuc cells

showed no noticeable difference with or without the presence of the CET single factor (**Figure 35B**). Successful improvement in gene silencing was achieved at low doses of siRNA (3.1–6.3 ng well^{-1}) (**Figure 35C**). Subsequently, a double CET dose was introduced. As expected, high RNAi efficacy was attained at a low siRNA dose of 3.1 ng, which was explainable by the $^1O_2$ assistance in endosomal membrane disruption (**Figure 35D**).

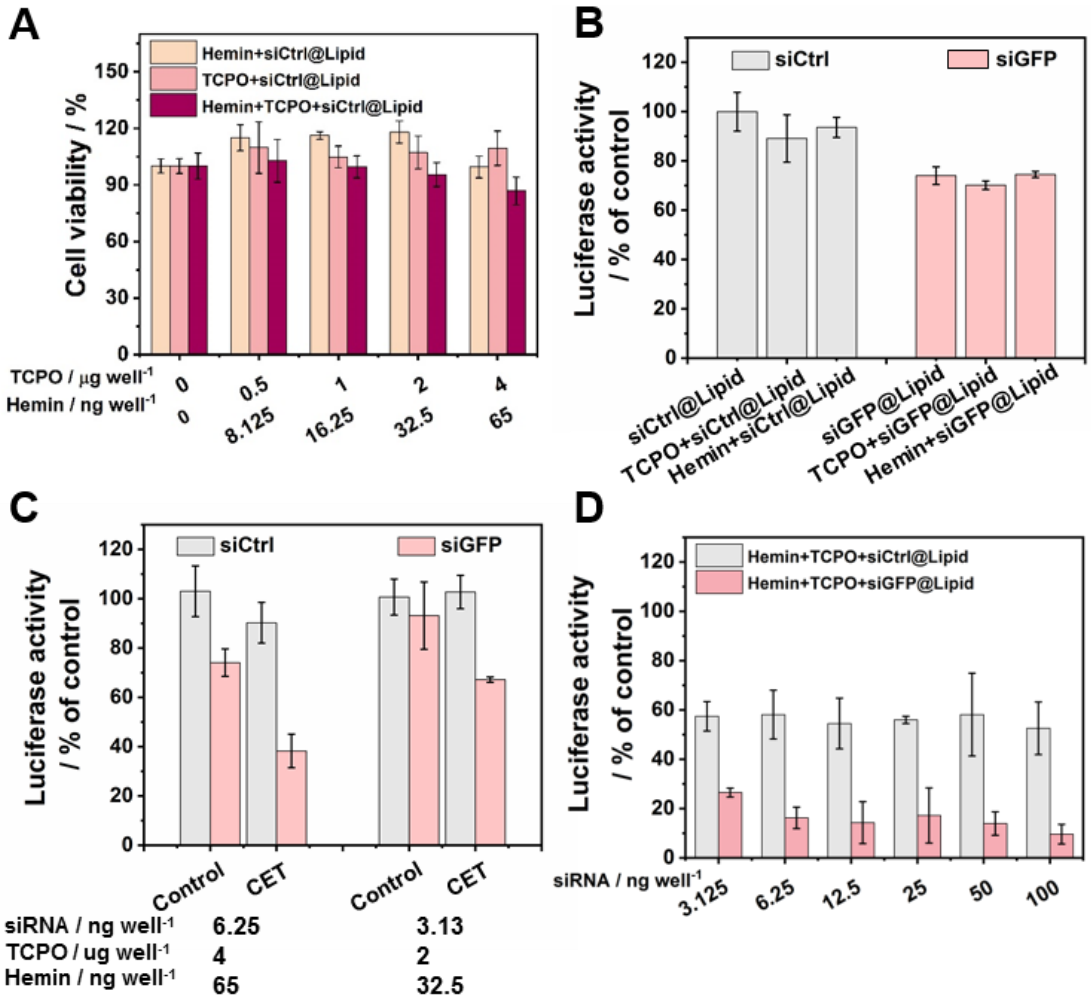

Figure 35. (A) Cell viability of KB cells incubated with serial concentrations of Hemin+siRNA@Lipid, TCPO+siRNA@Lipid, and Hemin+TCPO+siRNA@Lipid. Incubation time was 48 h. (B) Gene silencing efficiency of KB/eGFPLuc treated with various control LNPs for 48 h. siRNA amount was 6.25 ng well^{-1}; TCPO amount was 4 µg well^{-1}; hemin amount was 65 ng well^{-1}. (C) Gene silence efficacy of CET-enhanced siRNA@Lipid. The CET group refers to Hemin+TCPO+siRNA@Lipid and control group refers to siRNA@Lipid. Luciferase activity was

normalized to cells without any treatment. (D) Gene silencing efficiency of siRNA@Lipid enhanced with a higher CET dose (8 µg TCPO well^{-1}; 130 ng hemin well^{-1}).

3.2.8 Evaluation of CET effect for enhancing gene silencing

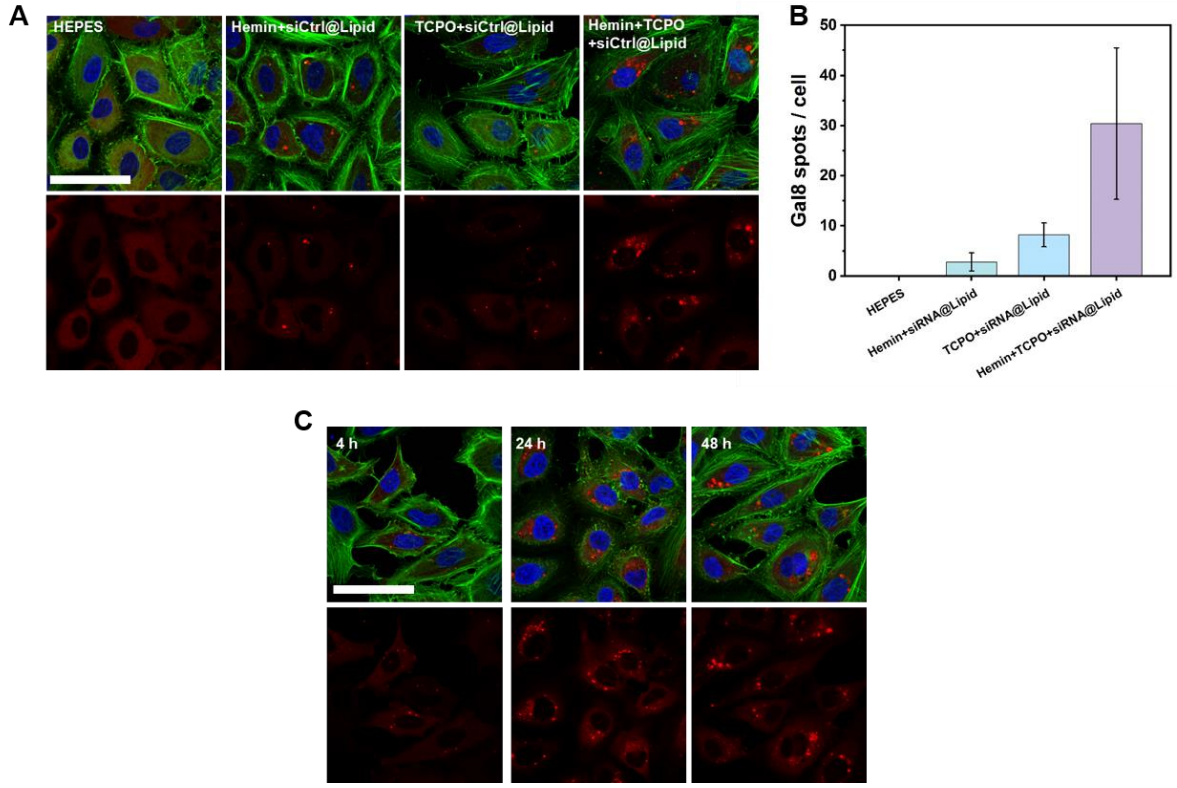

Figure 36. (A) CLSM of Hela mRuby3/Gal8 cells after treating with different formulations. siRNA, TCPO, and hemin concentrations were same as Figure 35C on the right side; the siRNA amount was 500 ng; incubation time was 12 h. (B) Quantitative analysis of Gal8 spots per cell of cells treated with Hemin+TCPO+siRNA@Lipid for 12 h. (C) CLSM images of Hela mRuby3/Gal8 cells after treating with Hemin+TCPO+siRNA@Lipid for 4 h, 24 h, and 48 h. scale bar, 100 µm. Nuclei were stained with DAPI (blue), actin filaments were stained with rhodamine phalloidin (green), red fluorescence indicates Gal8-mRuby3. The CLSM was performed by Miriam Höhn (Pharmaceutical Biotechnology, LMU München). The HeLa cells expressing Gal8-mRuby3 fusion protein were established by Dr. Yi Lin (former PhD student at Pharmaceutical Biotechnology, LMU München).

To further confirm this conclusion, an endosomal escape reporter cell line, HeLa cells expressing Gal8-mRuby3, was employed to assess the endosomal rupture capability of the CET system (**Figure 36A**). In this model, a cytosolic Gal8-mRuby3 fusion protein

would be recruited to disrupt endosomal membranes, forming visible bright fluorescent spots [171]. In this model, the molecular targets of Gal8 are glycans containing galactose, found exclusively on the inner membrane of endosomes. Following a 12-h treatment, formulations combining hemin and TCPO were found to prompt superior endosomolytic events compared to their individual counterparts, showing nearly 3-fold (*P* value of 0.03) and 10-fold (*P* value of 0.02) higher than TCPO and hemin group, respectively (**Figure 36B**). Meanwhile, no intracellular punctate spot was detected in the HEPES group. The endosomal escape event started at approximately 4 h of incubation and extended for over 48 h (**Figure 36C**). Altogether, consistent with the conclusion above, the designed CET system could induce effective double bonds oxidization in phospholipid through lipid peroxidation, providing an opportunity for nucleic acid to escape from LNP and endosome.

3.2.9 Evaluation of siNrf2-based LNPs-correlated cancer cell killing effect

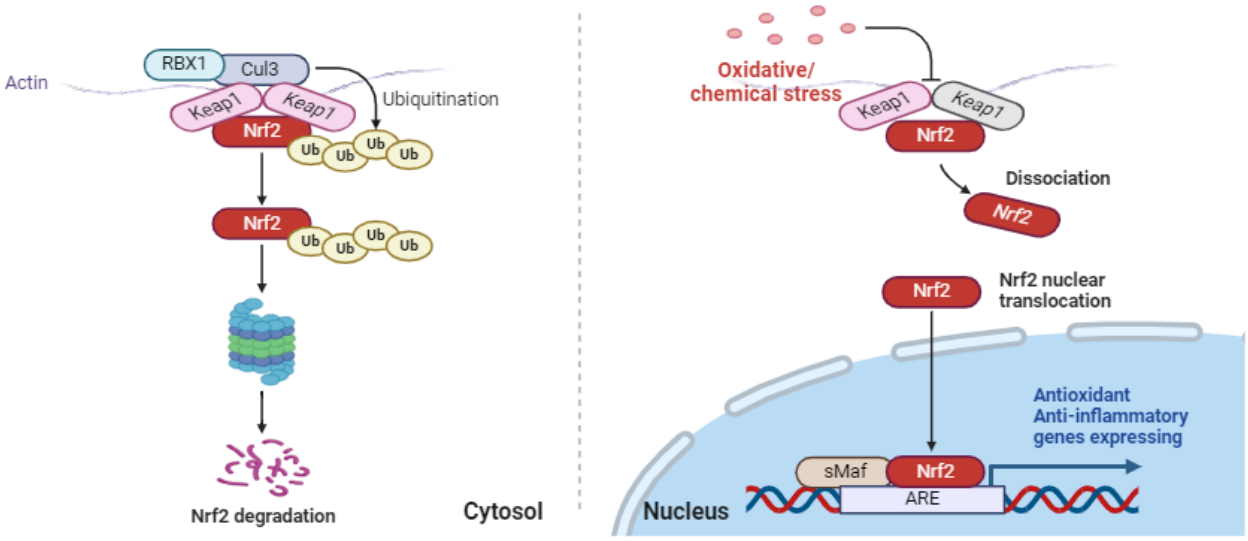

Scheme 4. Schematic illustration of transcription factor Nrf2-Keap 1 system associated detoxification.

As demonstrated in **Figure 34**, the CET system at standard dose (4 μg TCPO and 65 ng hemin) was capable of delivering siRNA and holding good biocompatibility; at a high dose (8 μg TCPO and 130 ng hemin), more ROS can be produced for directly killing cancer cells. To enhance the anticancer capability of CET toward cancer cells, gene silencing of the Nrf2 (also known as Nfe2l2)-Keap1 system was introduced; it is considered as a

master transcriptional regulator of endogenous oxidative stress [55,85,86,175–177]. For ROS-mediated treatments, Nrf2 plays a crucial role in helping cancer cells evade oxidative damage. Under oxidative stress, Nrf2 dissociates from Keap1, relocates to the nucleus, and takes shape into a heterodimer with its partner (**Scheme 4, right**). The resulting complex binds to antioxidant-responsive element sequences, activating downstream genes and antioxidants. Oppositely, under healthy conditions, Nrf2 mRNA is constitutively expressed and bound to its inhibitor, Keap1, which facilitates binding of the Cullin-3 (Cul3)/RING box protein1 (RBX1) E3 ubiquitin ligase complex, consequently causing proteasomal degradation of Nrf2 (**Scheme 4, left**). Adopting the Nrf2-Keap1 pathway as the target, we used siNrf2 to synergize with the ROS oxidative effect, and the generated ROS enhanced the siRNA endosomal escape simultaneously.

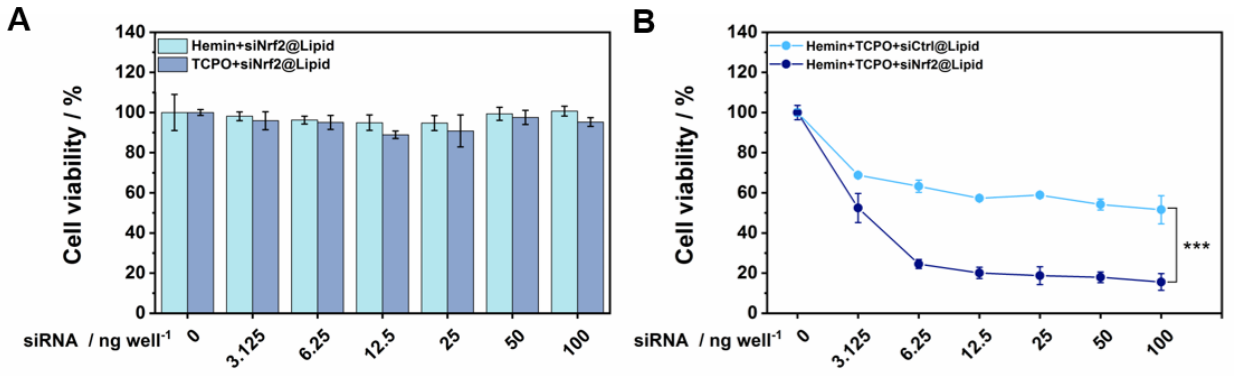

Figure 37. (A) Assessment of KB cell viability following exposure to various concentrations of Hemin+siNrf2@Lipid and TCPO+siNrf2@Lipid. Incubation time was 48 h. (B) siNrf2-based LNPs for killing KB cell. TCPO amount was 8 µg well^{-1} and hemin amount was 130 ng well^{-1}. Statistical significances were calculated by Student's *t*-test. *p < 0.05, **p < 0.01, ***p < 0.001.

After co-culturing cancer cells with Hemin+siNrf2@Lipid or TCPO+siNrf2@Lipid for 48 h, the excellent biocompatibility of the prepared siNrf2-synergized CET system was validated (**Figure 37A**). Opposite to the control groups, after integrating hemin and TCPO, more than 80% of cells were dead at 8 µg well^{-1} TCPO, 130 ng well^{-1} hemin, and 12.5 ng siRNA doses, and 39% reduction was demonstrated compared to Hemin+TCPO+siCtrl@Lipid (**Figure 37B**). Consistent with the conclusion in **Figure 34D**, after replacing siCtrl with siNrf2, the CET system maintains good biosafety to normal cells (**Figure 38**).

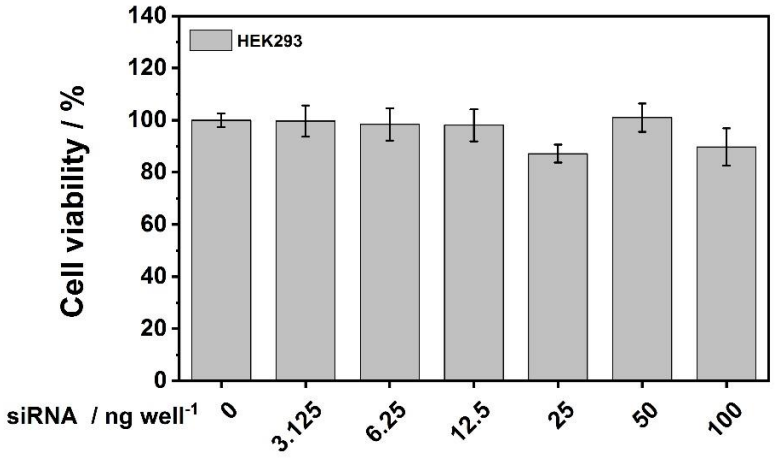

Figure 38. Cytocompatibility of Hemin+TCPO+siNrf2@Lipid in H_2O_2 low producing cells (HEK293). The TCPO amount was 8 μg well^{-1} and the hemin amount were 130 ng well^{-1}. Incubation time was 48 h.

Next, with the help of Annexin V-FITC and PI, the apoptosis rate of KB cells incubated with various formulations was determined *via* flow cytometry (**Figure 39**). The apoptosis level of cells incubated with the CET group in the presence of siNrf2 was around 60%, significantly surpassing that of the CET group alone (36%).

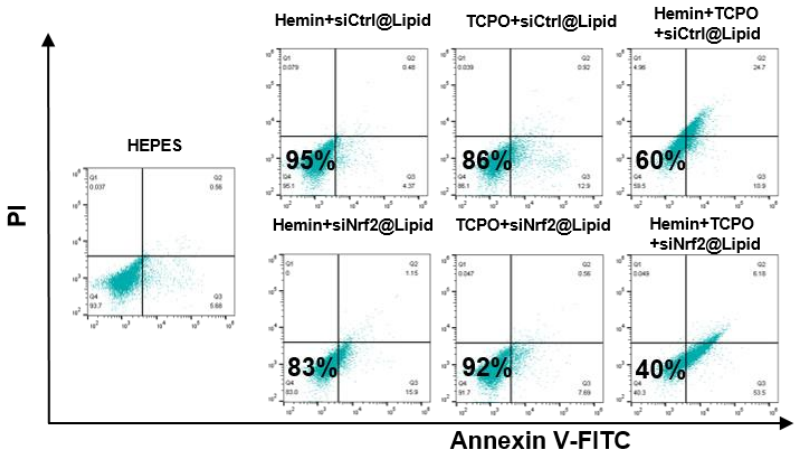

Figure 39. Annexin V-FITC/PI cell apoptosis analysis of KB cells after different treatments. siRNA amount was 1.88 μg well^{-1}; TCPO amount was 60 μg well^{-1}; hemin amount was 975 ng well^{-1}; incubation time was 48 h.

Further evolution of Nrf2 gene silencing at the mRNA level was done through RT-qPCR assay. As shown in **Figure 40**, treatments with all LNPs including siNrf2 induced significant knockdown of Nrf2 mRNA (46% by Hemin+siNrf2@Lipid, 51% by TCPO+siNrf2@Lipid, and 87% by Hemin+TCPO+siNrf2@Lipid); conversely, siCtrl groups remained expression levels comparable to the HEPES (20 mM, pH 7.4) group. Moreover, the Nrf2 mRNA expression level of the CET group was much lower than that of the corresponding control groups. These results proved that the CET involvement results in improved gene silencing efficacy at the mRNA expression level.

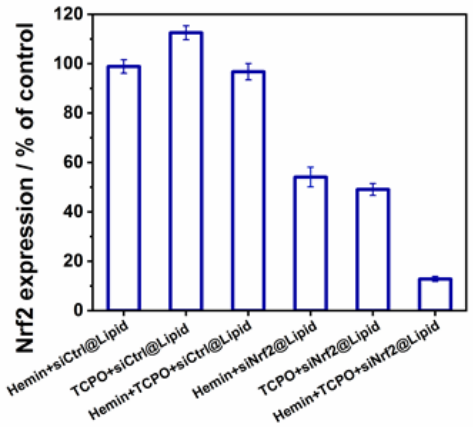

Figure 40. mRNA expression in KB cells (120,000 cells/well) after Hemin+TCPO+siNrf2@Lipid incubation for 48 h. siRNA dose was 2 μg, TCPO dose was 400 μg, and hemin dose was 6.5 μg. Cells treated with Hemin+siCtrl@Lipid, TCPO+siCtrl@Lipid, and Hemin+TCPO+siCtrl@Lipid served as negative controls.

3.2.10 Evaluation of siEG5-based LNPs-correlated cancer cell killing effect

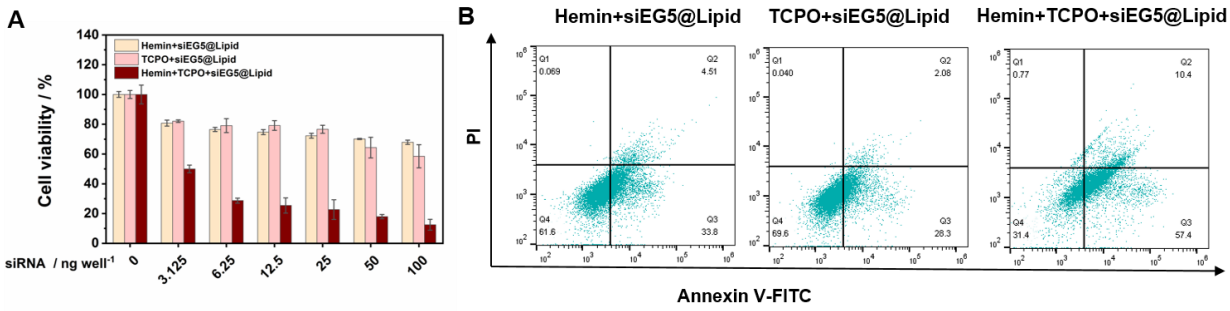

Figure 41. (A) Dose titration of CET system-assistant siEG5 LNPs. TCPO amount was 8 μg well^{-1} and hemin amount was 130 ng well^{-1}. Incubation time was 48 h. (B) Annexin V-

FITC/PI cell apoptosis analysis of KB cells after different treatments. The incubation time was 48 h.

In addition, we underscored the CET-enhanced RNAi using an alternative type of siRNA. EG5, a motor protein that provides a crucial role in cellular mitosis, can be silenced to impede the organization of the mitotic spindle apparatus, leading to cell-cycle arrest; therefore, initiating programmed cellular apoptosis in tumor cells [139,140]. As shown in **Figure 41A**, the survival rate of cells incubated with siEG5 was obviously decreased, in comparison with Hemin+siEG5@Lipid and TCPO+siEG5@Lipid. Notably, the highest cell-killing efficacy, around 87 %, was achieved at a dose of 100 ng siEG5, 8 µg TCPO, and 130 ng hemin. The apoptosis assay also proved superior CET-improved siEG5 cell killing with a total apoptotic cell percentage of 68%, much higher than those for a single treatment (**Figure 41B**). The improvement of gene silencing by CET was also demonstrated at the mRNA level (**Figure 42**). The results demonstrated that the incorporation of CET into the LNP amplified the effectiveness of therapeutic gene silencing.

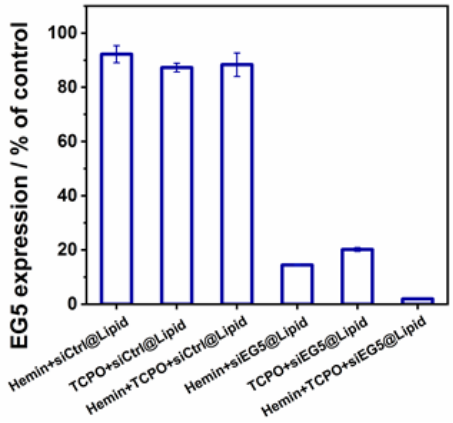

Figure 42. mRNA expression in KB cells (120,000 cells/well) Hemin+TCPO+siEG5@Lipid incubation for 48 h. siRNA dose was 2 µg, TCPO dose was 400 µg, and hemin dose was 6.5 µg. Cells treated with Hemin+siCtrl@Lipid, TCPO+siCtrl@Lipid, and Hemin+TCPO+siCtrl@Lipid served as negative controls.

4 Summary

In the first part, a novel concept of self-exciting chemical internalization is proposed for improving RNAi therapeutics, emphasizing promoting endosomal escape of nucleic acids. This strategy relies on a CET-based lipopolyplex, in which GNs act as effective receptors, and TCPO reacts with intratumorally over-expressed H_2O_2 to realize the receptors' chemical excitation and $^1O_2$ generation. A chemically sequence-defined cationic oligomer serves as a molecular glue to electrostatically attract negatively charged nucleic acids as well as GNs. In the direction of resolving endosomal escape hurdle, the CET and lipopolyplex are introduced into the siRNA delivery system. As expected, the lipopolyplex facilitated endosomal membrane rupture through lipid peroxidation, the combination of GNs and TCPO in this strategy dramatically boosted the formations of Gal8 spots with 51-fold and 9-fold compare to the HEPES group and GNs+siRNA@Lipid group, respectively. More generally, the CET not only increased tumor-related gene silencing efficacy *via* enhanced endosomal disruption, but also triggered cancer cell apoptosis and necrosis through direct cell killing, tumor vascular damage, and a cascade of the immune response. Here, taking EG5 as an example, which is a crucial motor protein for cellular mitosis. Obviously, significant cell death induced by siEG5-mediated mitotic arrest *via* inhibiting organization of spindle apparatus was observed, and this effect was promoted through incorporating the CET effect.

In the second part, inspired by the photochemical internalization technology for enhanced cytosolic nucleic acid delivery, we first design a novel LNP containing siRNA and CET components (Hemin+TCPO+siRNA@Lipid) for enhanced chemical internalization excited by H_2O_2 within the tumor environment. Co-encapsulating the hydrophobic CET donor TCPO and acceptor hemin facilitated their energy transfer, subsequently exciting O_2 to produce $^1O_2$. Our investigation aimed to answer the following questions: *i)* Can CET-triggered ROS generation enhance the endosomal escape of siRNA@Lipid? *ii)* Can the ROS also directly damage cancer cells? *iii)* Can combined silencing of tumor-protective-Nrf2 enhance ROS-induced cancer cell killing? All the three questions were answered. The CET process boosted endosomal disruption as measured by a Gal8 sensor. Three distinct types of siRNA, siGFP, siEG5, and siNrf2, were employed to verify CET-assisted

gene silencing. A relatively high RNAi efficacy was attained at a low siGFP at around 3–6 ng per well. For siEG5, induction of apoptosis of cancer cells was demonstrated, achieving cell-killing efficacy of approximately 75% at 12.5 ng. Moreover, a 24% improvement in apoptosis level was observed through the regulation of endogenous oxidative stress by siNrf2. Our research underscores the great promise of CET-enhanced LNPs for advancing antitumoral nucleic acid therapeutics.

Taken together, a new direction for enhancing RNAi is proposed. Compared with traditional photochemical internalization, lipid-based CET delivery systems hold the advantages of improving endosomal escape without external assistance and minimizing unnecessary damage, which shows great prospects for advancing antitumoral nucleic acid therapy.

5 Abbreviations

CET	Chemical electron transfer
CLSM	Confocal laser scanning microscopy
CRET	Chemiluminescence resonance energy transfer
DAPI	4’,6-Diamidino-2-phenylindole
DLS	Dynamic light scattering
DMEM	Dulbecco’s modified Eagle’s medium
DMSO	Dimethyl sulfoxide
DOPE	1,2-Di-(9Z-octadecenoyl)-*sn*-glycero-3-phosphoethanolamine
DOTAP	1,2-Dioleoyl-3-trimethylammonium propane
DPA	9,10-Diphenanthraquinone
DSPC	1,2-Dioctadecanoyl-*sn*-glycero-3-phosphocholine
EG5	Eglin 5
eGFP	Enhanced green fluorescent protein
FBS	Fetal bovine serum
FDA	United States Food and Drug Administration
FITC	Fluorescein isothiocyanate
Gal8	Galectin-8
GNs	Gold nanoparticles
HEPES	*N*-2-Hydroxyethylpiperazine-*N'*-2-ethanesulfonic acid
H_2O_2	Hydrogen peroxide
JC-1	5,5,6',6'-Tetrachloro-1,1',3,3'-tetraethyl-imidacarbocyanine

LDL	Low-density lipoprotein
LNP	Lipid nanoparticle
MTT	Methyl thiazolyl tetrazolium
MβCD	Methyl-β-cyclodextrin
NAC	*N*-acetylcysteine
NIR-II	Second near-infrared
NMR	Nuclear magnetic resonance
Nrf2	Nuclear factor erythroid 2-related factor 2
$^1O_2$	Singlet oxygen
PBS	Phosphate-buffered saline
PCSK9	Proprotein convertase subtilisin/kexin type 9
PDI	Polydispersity index
PEG	Poly(ethylene glycol)
PEG-DMG	1,2-Dimyristoyl-rac-glycero-3-methoxypolyethylene glycol-2000
PEI	Polyethyleneimine
PFA	Paraformaldehyde
PI	Propidium iodide
PSs	Photosensitizers
RNAi	RNA interference
ROS	Reactive oxygen species
RPMI-1640	Roswell Park Memorial Institute-1640 medium
RT-qPCR	Reverse transcription-quantitative real-time PCR
siRNA	Small interfering RNA

SPPS	Solid-phase supported peptide synthesis
Stp	Succinyl-tetraethylene-pentamine
TEM	Transmission electron microscope
TCPO	Bis(2,4,6-trichlorophenyl) oxalate
TOTL-Stp	Tetra-oleoyl tri-lysino succinoyl tetraethylene pentamine

6 References

1. Ecker, J.R.; Davis, R.W. Inhibition of Gene Expression in Plant Cells by Expression of Antisense RNA. *Proc. Natl. Acad. Sci.* **1986**, *83*, 5372–5376.

2. Napoli, C.; Lemieux, C.; Jorgensen, R. Introduction of a Chimeric Chalcone Synthase Gene into Petunia Results in Reversible Co-Suppression of Homologous Genes in Trans. *Plant Cell* **1990**, *2*, 279.

3. Hu, B.; Zhong, L.; Weng, Y.; Peng, L.; Huang, Y.; Zhao, Y.; Liang, X.-J. Therapeutic siRNA: State of the Art. *Signal Transduct. Target. Ther.* **2020**, *5*, 101.

4. Setten, R.L.; Rossi, J.J.; Han, S. The Current State and Future Directions of RNAi-Based Therapeutics. *Nat. Rev. Drug Discov.* **2019**, *18*, 421–446.

5. Elbashir, S.M.; Harborth, J.; Lendeckel, W.; Yalcin, A.; Weber, K.; Tuschl, T. Duplexes of 21-Nucleotide RNAs Mediate RNA Interference in Cultured Mammalian Cells. *Nature* **2001**, *411*, 494–498.

6. McCaffrey, A.P.; Meuse, L.; Pham, T.-T.T.; Conklin, D.S.; Hannon, G.J.; Kay, M.A. RNA Interference in Adult Mice. *Nature* **2002**, *418*, 38–39.

7. Wang, Z.; Song, L.; Liu, Q.; Tian, R.; Shang, Y.; Liu, F.; Liu, S.; Zhao, S.; Han, Z.; Sun, J.; et al. A Tubular DNA Nanodevice as a siRNA/Chemo- Drug Co- delivery Vehicle for Combined Cancer Therapy. *Angew. Chem. Int. Ed.* **2021**, *60*, 2594–2598.

8. Guo, Y.; Zhang, Q.; Zhu, Q.; Gao, J.; Zhu, X.; Yu, H.; Li, Y.; Zhang, C. Copackaging Photosensitizer and PD-L1 siRNA in a Nucleic Acid Nanogel for Synergistic Cancer Photoimmunotherapy. *Sci. Adv.* **2022**, *8*, 1–13.

9. Qiu, J.; Fan, Q.; Xu, S.; Wang, D.; Chen, J.; Wang, S.; Hu, T.; Ma, X.; Cheng, Y.; Xu, L. A Fluorinated Peptide with High Serum- and Lipid-Tolerence for the Delivery of siRNA Drugs to Treat Obesity and Metabolic Dysfunction. *Biomaterials* **2022**, *285*, 121541.

10. Baran-Rachwalska, P.; Torabi-Pour, N.; Sutera, F.M.; Ahmed, M.; Thomas, K.; Nesbit, M.A.; Welsh, M.; Moore, C.B.T.; Saffie-Siebert, S.R. Topical siRNA

Delivery to the Cornea and Anterior Eye by Hybrid Silicon-Lipid Nanoparticles. *J. Control. Release* **2020**, *326*, 192–202.

11. Kleinman, M.E.; Yamada, K.; Takeda, A.; Chandrasekaran, V.; Nozaki, M.; Baffi, J.Z.; Albuquerque, R.J.C.; Yamasaki, S.; Itaya, M.; Pan, Y.; et al. Sequence- and Target-Independent Angiogenesis Suppression by siRNA via TLR3. *Nature* **2008**, *452*, 591–597.

12. DeVincenzo, J.; Lambkin-Williams, R.; Wilkinson, T.; Cehelsky, J.; Nochur, S.; Walsh, E.; Meyers, R.; Gollob, J.; Vaishnaw, A. A Randomized, Double-Blind, Placebo-Controlled Study of an RNAi-Based Therapy Directed against Respiratory Syncytial Virus. *Proc. Natl. Acad. Sci.* **2010**, *107*, 8800–8805.

13. Kaiser, P.K.; Symons, R.C.A.; Shah, S.M.; Quinlan, E.J.; Tabandeh, H.; Do, D. V.; Reisen, G.; Lockridge, J.A.; Short, B.; Guerciolini, R.; et al. RNAi-Based Treatment for Neovascular Age-Related Macular Degeneration by siRNA. *Am. J. Ophthalmol.* **2010**, *150*, 33–39.

14. Garba, A.O.; Mousa, S.A. Bevasiranib for the Treatment of Wet, Age-Related Macular Degeneration. *Ophthalmol. Eye Dis.* **2010**, *2*, 75–83.

15. Schlee, M.; Hornung, V.; Hartmann, G. siRNA and isRNA: Two Edges of One Sword. *Mol. Ther.* **2006**, *14*, 463–470.

16. Luo, J.; Höhn, M.; Reinhard, S.; Loy, D.M.; Klein, P.M.; Wagner, E. IL4-Receptor-Targeted Dual Antitumoral Apoptotic Peptide–siRNA Conjugate Lipoplexes. *Adv. Funct. Mater.* **2019**, *29*, 1900697.

17. Krohn-Grimberghe, M.; Mitchell, M.J.; Schloss, M.J.; Khan, O.F.; Courties, G.; Guimaraes, P.P.G.; Rohde, D.; Cremer, S.; Kowalski, P.S.; Sun, Y.; et al. Nanoparticle-Encapsulated siRNAs for Gene Silencing in the Haematopoietic Stem-Cell Niche. *Nat. Biomed. Eng.* **2020**, *4*, 1076–1089.

18. Heyes, J.; Palmer, L.; Bremner, K.; MacLachlan, I. Cationic Lipid Saturation Influences Intracellular Delivery of Encapsulated Nucleic Acids. *J. Control. Release* **2005**, *107*, 276–287.

19. Miao, L.; Lin, J.; Huang, Y.; Li, L.; Delcassian, D.; Ge, Y.; Shi, Y.; Anderson, D.G.

Synergistic Lipid Compositions for Albumin Receptor Mediated Delivery of mRNA to the Liver. *Nat. Commun.* **2020**, *11*. 2424.

20. Hou, X.; Zaks, T.; Langer, R.; Dong, Y. Lipid Nanoparticles for mRNA Delivery. *Nat. Rev. Mater.* 2021, *6*, 1078–1094.

21. Filipczak, N.; Pan, J.; Yalamarty, S.S.K.; Torchilin, V.P. Recent Advancements in Liposome Technology. *Adv. Drug Deliv. Rev.* **2020**, *156*, 4–22.

22. Kaddah, S.; Khreich, N.; Kaddah, F.; Charcosset, C.; Greige-Gerges, H. Cholesterol Modulates the Liposome Membrane Fluidity and Permeability for a Hydrophilic Molecule. *Food Chem. Toxicol.* **2018**, *113*, 40–48.

23. Zhang, Y.; Li, Q.; Dong, M.; Han, X. Effect of Cholesterol on the Fluidity of Supported Lipid Bilayers. *Colloids Surfaces B Biointerfaces* **2020**, *196*, 111353.

24. Ahn, I.; Kang, C.S.; Han, J. Where Should siRNAs Go: Applicable Organs for siRNA Drugs. *Exp. Mol. Med.* **2023**, *55*, 1283–1292.

25. Bangham, A.D.; Standish, M.M.; Watkins, J.C. Diffusion of Univalent Ions across the Lamellae of Swollen Phospholipids. *J. Mol. Biol.* **1965**, *13*, 238–252.

26. Kotelianski, V.; Zatsepin, T.; Kotelevtsev, Y. Lipid Nanoparticles for Targeted siRNA Delivery–Going from Bench to Bedside. *Int. J. Nanomedicine* **2016**, *11*, 3077–3086.

27. Nikam, R.R.; Gore, K.R. Journey of siRNA: Clinical Developments and Targeted Delivery. *Nucleic Acid Ther.* **2018**, *28*, 209–224.

28. Boussif, O.; Lezoualc'h, F.; Zanta, M.A.; Mergny, M.D.; Scherman, D.; Demeneix, B.; Behr, J.P. A Versatile Vector for Gene and Oligonucleotide Transfer into Cells in Culture and in Vivo: Polyethylenimine. *Proc. Natl. Acad. Sci.* **1995**, *92*, 7297–7301.

29. Pinnapireddy, S.R.; Duse, L.; Strehlow, B.; Schäfer, J.; Bakowsky, U. Composite Liposome-PEI/Nucleic Acid Lipopolyplexes for Safe and Efficient Gene Delivery and Gene Knockdown. *Colloids Surf. B* **2017**, *158*, 93–101.

30. Schaffert, D.; Troiber, C.; Salcher, E.E.; Fröhlich, T.; Martin, I.; Badgujar, N.;

Dohmen, C.; Edinger, D.; Kläger, R.; Maiwald, G.; et al. Solid-Phase Synthesis of Sequence-Defined T- , i- , and U-Shape Polymers for pDNA and siRNA Delivery. *Angew. Chem. Int. Ed.* **2011**, *50*, 8986–8989.

31. Satterlee, A.B.; Huang, L. Current and Future Theranostic Applications of the Lipid-Calcium-Phosphate Nanoparticle Platform. *Theranostics* **2016**, *6*, 918–929.

32. Yeh, C.H.; Chen, J.; Zheng, G.; Huang, L.; Hsu, Y.C. Novel Pyropheophorbide Phosphatydic Acids Photosensitizer Combined Egfr sirna Gene Therapy for Head and Neck Cancer Treatment. *Pharmaceutics* **2021**, *13*. 1435.

33. Huang, J.-L.; Chen, H.-Z.; Gao, X.-L. Lipid-Coated Calcium Phosphate Nanoparticle and beyond: A Versatile Platform for Drug Delivery. *J. Drug Target.* **2018**, *26*, 398–406.

34. Li, J.; Chen, Y.-C.; Tseng, Y.-C.; Mozumdar, S.; Huang, L. Biodegradable Calcium Phosphate Nanoparticle with Lipid Coating for Systemic siRNA Delivery. *J. Control. Release* **2010**, *142*, 416–421.

35. Tang, J.; Li, L.; Howard, C.B.; Mahler, S.M.; Huang, L.; Xu, Z.P. Preparation of Optimized Lipid-Coated Calcium Phosphate Nanoparticles for Enhanced in Vitro Gene Delivery to Breast Cancer Cells. *J. Mater. Chem. B* **2015**, *3*, 6805–6812.

36. Chatterjee, S.; Kon, E.; Sharma, P.; Peer, D. Endosomal Escape: A Bottleneck for LNP-Mediated Therapeutics. *Proc. Natl. Acad. Sci.* **2024**, *121*, e2307800120.

37. Yameen, B.; Choi, W. Il; Vilos, C.; Swami, A.; Shi, J.; Farokhzad, O.C. Insight into Nanoparticle Cellular Uptake and Intracellular Targeting. *J. Control. Release* 2014, *190*, 485–499.

38. Gilleron, J.; Querbes, W.; Zeigerer, A.; Borodovsky, A.; Marsico, G.; Schubert, U.; Manygoats, K.; Seifert, S.; Andree, C.; Stöter, M.; et al. Image-Based Analysis of Lipid Nanoparticle–Mediated siRNA Delivery, Intracellular Trafficking and Endosomal Escape. *Nat. Biotechnol.* **2013**, *31*, 638–646.

39. Lee, J.; Kim, D.; Byun, J.; Wu, Y.; Park, J.; Oh, Y.K. In Vivo Fate and Intracellular Trafficking of Vaccine Delivery Systems. *Adv. Drug Deliv. Rev.* **2022**, *186*, 114325.

40. Kim, M.; Jeong, M.; Hur, S.; Cho, Y.; Park, J.; Jung, H.; Seo, Y.; Woo, H.A.; Nam, K.T.; Lee, K.; et al. Engineered Ionizable Lipid Nanoparticles for Targeted Delivery of RNA Therapeutics into Different Types of Cells in the Liver. *Sci. Adv.* **2021**, *7*, eabf4398.

41. Tsoi, K.M.; MacParland, S.A.; Ma, X.-Z.; Spetzler, V.N.; Echeverri, J.; Ouyang, B.; Fadel, S.M.; Sykes, E.A.; Goldaracena, N.; Kaths, J.M.; et al. Mechanism of Hard-Nanomaterial Clearance by the Liver. *Nat. Mater.* **2016**, *15*, 1212–1221.

42. Abu Lila, A.S.; Kiwada, H.; Ishida, T. The Accelerated Blood Clearance (ABC) Phenomenon: Clinical Challenge and Approaches to Manage. *J. Control. Release* **2013**, *172*, 38–47.

43. Dézsi, L.; Fülöp, T.; Mészáros, T.; Szénási, G.; Urbanics, R.; Vázsonyi, C.; Őrfi, E.; Rosivall, L.; Nemes, R.; Kok, R.J.; et al. Features of Complement Activation-Related Pseudoallergy to Liposomes with Different Surface Charge and PEGylation: Comparison of the Porcine and Rat Responses. *J. Control. Release* **2014**, *195*, 2–10.

44. Kozma, G.T.; Mészáros, T.; Vashegyi, I.; Fülöp, T.; Örfi, E.; Dézsi, L.; Rosivall, L.; Bavli, Y.; Urbanics, R.; Mollnes, T.E.; et al. Pseudo-Anaphylaxis to Polyethylene Glycol (PEG)-Coated Liposomes: Roles of Anti-PEG IgM and Complement Activation in a Porcine Model of Human Infusion Reactions. *ACS Nano* **2019**, *13*, 9315–9324.

45. Tahtinen, S.; Tong, A.-J.; Himmels, P.; Oh, J.; Paler-Martinez, A.; Kim, L.; Wichner, S.; Oei, Y.; McCarron, M.J.; Freund, E.C.; et al. IL-1 and IL-1ra Are Key Regulators of the Inflammatory Response to RNA Vaccines. *Nat. Immunol.* **2022**, *23*, 532–542.

46. Alameh, M.-G.; Tombácz, I.; Bettini, E.; Lederer, K.; Ndeupen, S.; Sittplangkoon, C.; Wilmore, J.R.; Gaudette, B.T.; Soliman, O.Y.; Pine, M.; et al. Lipid Nanoparticles Enhance the Efficacy of mRNA and Protein Subunit Vaccines by Inducing Robust T Follicular Helper Cell and Humoral Responses. *Immunity* **2021**, *54*, 2877–2892.

47. Douglas, K.L. Toward Development of Artificial Viruses for Gene Therapy: A

Comparative Evaluation of Viral and Non-Viral Transfection. *Biotechnol. Prog.* **2008**, *24*, 871–883.

48. Hoekstra, D.; Rejman, J.; Wasungu, L.; Shi, F.; Zuhorn, I. Gene Delivery by Cationic Lipids: In and out of an Endosome. *Biochem. Soc. Trans.* **2007**, *35*, 68–71.

49. Wasungu, L.; Hoekstra, D. Cationic Lipids, Lipoplexes and Intracellular Delivery of Genes. *J. Control. Release* **2006**, *116*, 255–264.

50. Zheng, L.; Bandara, S.R.; Tan, Z.; Leal, C. Lipid Nanoparticle Topology Regulates Endosomal Escape and Delivery of RNA to the Cytoplasm. *Proc. Natl. Acad. Sci.* **2023**, *120*, e2301067120.

51. Maxfield, F.R.; McGraw, T.E. Endocytic Recycling. *Nat. Rev. Mol. Cell Biol.* **2004**, *5*, 121–132.

52. Jayaraman, M.; Ansell, S.M.; Mui, B.L.; Tam, Y.K.; Chen, J.; Du, X.; Butler, D.; Eltepu, L.; Matsuda, S.; Narayanannair, J.K.; et al. Maximizing the Potency of siRNA Lipid Nanoparticles for Hepatic Gene Silencing In Vivo. *Angew. Chem. Int. Ed.* **2012**, *124*, 8657–8661.

53. Ormond, A.B.; Freeman, H.S. Dye Sensitizers for Photodynamic Therapy. *Materials (Basel).* **2013**, *6*, 817–840.

54. Yang, T.; Liu, L.; Deng, Y.; Guo, Z.; Zhang, G.; Ge, Z.; Ke, H.; Chen, H. Ultrastable Near-Infrared Conjugated-Polymer Nanoparticles for Dually Photoactive Tumor Inhibition. *Adv. Mater.* **2017**, *29*. 1700487.

55. Deng, S.; Li, X.; Liu, S.; Chen, J.; Li, M.; Chew, S.Y.; Leong, K.W.; Cheng, D. Codelivery of CRISPR-Cas9 and Chlorin E6 for Spatially Controlled Tumor-Specific Gene Editing with Synergistic Drug Effects. *Sci. Adv.* **2020**, *6*, eabb4005.

56. Yang, B.; Chen, Y.; Shi, J. Reactive Oxygen Species (ROS)-Based Nanomedicine. *Chem. Rev.* **2019**, *119*, 4881–4985.

57. Wang, C.; Shi, Y.; Dan, Y.Y.; Nie, X.G.; Li, J.; Xia, X.H. Enhanced Peroxidase-Like Performance of Gold Nanoparticles by Hot Electrons. *Chem.-Eur. J.* **2017**, *23*, 6717–6723.

58. Lou, Z.; Fujitsuka, M.; Majima, T. Pt-Au Triangular Nanoprisms with Strong Dipole Plasmon Resonance for Hydrogen Generation Studied by Single-Particle Spectroscopy. *ACS Nano* **2016**, *10*, 6299–6305.

59. El-Beltagi, H.S.; Mohamed, H.I. Reactive Oxygen Species, Lipid Peroxidation and Antioxidative Defense Mechanism. *Not. Bot. Horti Agrobot. Cluj-Napoca* **2013**, *41*, 44.

60. Fromain, A.; Perez, J.E.; Van de Walle, A.; Lalatonne, Y.; Wilhelm, C. Photothermia at the Nanoscale Induces Ferroptosis via Nanoparticle Degradation. *Nat. Commun.* **2023**, *14*. 4637.

61. de Bruin, K.G.; Fella, C.; Ogris, M.; Wagner, E.; Ruthardt, N.; Bräuchle, C. Dynamics of Photoinduced Endosomal Release of Polyplexes. *J. Control. Release* **2008**, *130*, 175–182.

62. Lovell, J.F.; Jin, C.S.; Huynh, E.; Jin, H.; Kim, C.; Rubinstein, J.L.; Chan, W.C.W.; Cao, W.; Wang, L. V.; Zheng, G. Porphysome Nanovesicles Generated by Porphyrin Bilayers for Use as Multimodal Biophotonic Contrast Agents. *Nat. Mater.* **2011**, *10*, 324–332.

63. Mo, Y.; Cheng, M.H.Y.; D'Elia, A.; Doran, K.; Ding, L.; Chen, J.; Cullis, P.R.; Zheng, G. Light-Activated siRNA Endosomal Release (LASER) by Porphyrin Lipid Nanoparticles. *ACS Nano* **2023**, *17*, 4688–4703.

64. Jin, C.S.; Lovell, J.F.; Chen, J.; Zheng, G. Ablation of Hypoxic Tumors with Dose-Equivalent Photothermal, but Not Photodynamic, Therapy Using a Nanostructured Porphyrin Assembly. *ACS Nano* **2013**, *7*, 2541–2550.

65. Gao, M.; Zhu, L.; Peh, C.K.; Ho, G.W. Solar Absorber Material and System Designs for Photothermal Water Vaporization towards Clean Water and Energy Production. *Energy Environ. Sci.* **2019**, *12*, 841–864.

66. Wang, Z.; Yu, L.; Wang, Y.; Wang, C.; Mu, Q.; Liu, X.; Yu, M.; Wang, K.; Yao, G.; Yu, Z. Dynamic Adjust of Non-Radiative and Radiative Attenuation of AIE Molecules Reinforces NIR-II Imaging Mediated Photothermal Therapy and Immunotherapy. *Adv. Sci.* **2022**, *9*, 2104793.

67. Zhao, Z.; Chen, C.; Wu, W.; Wang, F.; Du, L.; Zhang, X.; Xiong, Y.; He, X.; Cai, Y.; Kwok, R.T.K.; et al. Highly Efficient Photothermal Nanoagent Achieved by Harvesting Energy via Excited-State Intramolecular Motion within Nanoparticles. *Nat. Commun.* **2019**, *10*, 768.

68. Zhang, F.; Han, X.; Hu, Y.; Wang, S.; Liu, S.; Pan, X.; Wang, H.; Ma, J.; Wang, W.; Li, S.; et al. Interventional Photothermal Therapy Enhanced Brachytherapy: A New Strategy to Fight Deep Pancreatic Cancer. *Adv. Sci.* **2019**, *6*, 1801507.

69. Cheng, L.; Zhang, F.; Wang, S.; Pan, X.; Han, S.; Liu, S.; Ma, J.; Wang, H.; Shen, H.; Liu, H.; et al. Activation of Prodrugs by NIR-Triggered Release of Exogenous Enzymes for Locoregional Chemo-Photothermal Therapy. *Angew. Chem. Int. Ed.* **2019**, *58*, 7728–7732.

70. Cheng, Y.; Chang, Y.; Feng, Y.; Jian, H.; Tang, Z.; Zhang, H. Deep-Level Defect Enhanced Photothermal Performance of Bismuth Sulfide–Gold Heterojunction Nanorods for Photothermal Therapy of Cancer Guided by Computed Tomography Imaging. *Angew. Chem. Int. Ed.* **2018**, *57*, 246–251.

71. Shen, S.; Chao, Y.; Dong, Z.; Wang, G.; Yi, X.; Song, G.; Yang, K.; Liu, Z.; Cheng, L. Bottom-Up Preparation of Uniform Ultrathin Rhenium Disulfide Nanosheets for Image-Guided Photothermal Radiotherapy. *Adv. Funct. Mater.* **2017**, *27*.1700250.

72. Zhang, F.; Liu, Y.; Lei, J.; Wang, S.; Ji, X.; Liu, H.; Yang, Q. Metal–Organic-Framework-Derived Carbon Nanostructures for Site- Specific Dual-Modality Photothermal/Photodynamic Thrombus Therapy. *Adv. Sci.* **2019**, *6*, 1901378.

73. Wang, C.; Xu, L.; Liang, C.; Xiang, J.; Peng, R.; Liu, Z. Immunological Responses Triggered by Photothermal Therapy with Carbon Nanotubes in Combination with Anti-CTLA-4 Therapy to Inhibit Cancer Metastasis. *Adv. Mater.* **2014**, *26*, 8154–8162.

74. Chen, W.; Ouyang, J.; Liu, H.; Chen, M.; Zeng, K.; Sheng, J.; Liu, Z.; Han, Y.; Wang, L.; Li, J.; et al. Black Phosphorus Nanosheet-Based Drug Delivery System for Synergistic Photodynamic/Photothermal/Chemotherapy of Cancer. *Adv. Mater.* **2017**, *29*. 1603864.

75. Wang, J.; Zhang, G.; Zhang, P. Graphene-Assisted Photothermal Effect on Promoting Catalytic Activity of Layered MnO_2 for Gaseous Formaldehyde Oxidation. *Appl. Catal. B Environ.* **2018**, *239*, 77–85.

76. Wang, M.; He, F.; Li, H.; Yang, S.; Zhang, J.; Ghosh, P.; Wang, H.-H.; Nie, Z. Near-Infrared Light-Activated DNA-Agonist Nanodevice for Nongenetically and Remotely Controlled Cellular Signaling and Behaviors in Live Animals. *Nano Lett.* **2019**, *19*, 2603–2613.

77. Huang, P.; Lin, J.; Li, W.; Rong, P.; Wang, Z.; Wang, S.; Wang, X.; Sun, X.; Aronova, M.; Niu, G.; et al. Biodegradable Gold Nanovesicles with an Ultrastrong Plasmonic Coupling Effect for Photoacoustic Imaging and Photothermal Therapy. *Angew. Chem. Int. Ed.* **2013**, *125*, 14208–14214.

78. Kim, J.; Kim, J.; Jeong, C.; Kim, W.J. Synergistic Nanomedicine by Combined Gene and Photothermal Therapy. *Adv. Drug Deliv. Rev.* **2016**, *98*, 99–112.

79. Li, B.; Zhao, M.; Lai, W.; Zhang, X.; Yang, B.; Chen, X.; Ni, Q. Activatable NIR-II Photothermal Lipid Nanoparticles for Improved Messenger RNA Delivery. *Angew. Chem. Int. Ed.* **2023**, *62*, 3–9.

80. Wu, Q.; Zhang, F.; Pan, X.; Huang, Z.; Zeng, Z.; Wang, H.; Jiao, J.; Xiong, X.; Bai, L.; Zhou, D.; et al. Surface Wettability of Nanoparticle Modulated Sonothrombolysis. *Adv. Mater.* **2021**, *33*, 2007073.

81. Pan, X.; Wang, W.; Huang, Z.; Liu, S.; Guo, J.; Zhang, F.; Yuan, H.; Li, X.; Liu, F.; Liu, H. MOF-Derived Double-Layer Hollow Nanoparticles with Oxygen Generation Ability for Multimodal Imaging-Guided Sonodynamic Therapy. *Angew. Chem. Int. Ed.* **2020**, *59*, 13557–13561.

82. Tachibana, K.; Feril, L.B.; Ikeda-Dantsuji, Y. Sonodynamic Therapy. *Ultrasonics* **2008**, *48*, 253–259.

83. Pavlíčková, V.; Škubník, J.; Jurášek, M.; Rimpelová, S. Advances in Purpurin 18 Research: On Cancer Therapy. *Appl. Sci.* **2021**, *11*, 2254.

84. Li, G.; Zhang, Y.; Li, J. A Hybrid Nanoassembly for Ultrasound-Inducible Cytosolic siRNA Delivery and Cancer Sono-Gene Therapy. *Ultrason. Sonochem.* **2023**, *92*,

106262.

85. Sies, H.; Jones, D.P. Reactive Oxygen Species (ROS) as Pleiotropic Physiological Signalling Agents. *Nat. Rev. Mol. Cell Biol.* **2020**, *21*, 363–383.

86. Shi, S.; Wang, Y.; Wang, B.; Chen, Q.; Wan, G.; Yang, X.; Zhang, J.; Zhang, L.; Li, C.; Wang, Y. Homologous-Targeting Biomimetic Nanoparticles for Photothermal Therapy and Nrf2-siRNA Amplified Photodynamic Therapy against Oral Tongue Squamous Cell Carcinoma. *Chem. Eng. J.* **2020**, *388*, 124268.

87. Wan, G.; Chen, X.; Wang, H.; Hou, S.; Wang, Q.; Cheng, Y.; Chen, Q.; Lv, Y.; Chen, H.; Zhang, Q. Gene Augmented Nuclear-Targeting Sonodynamic Therapy via Nrf2 Pathway-Based Redox Balance Adjustment Boosts Peptide-Based Anti-PD-L1 Therapy on Colorectal Cancer. *J. Nanobiotechnology* **2021**, *19*, 347.

88. Cervia, L.D.; Yuan, F. Current Progress in Electrotransfection as a Nonviral Method for Gene Delivery. *Mol. Pharm.* **2018**, *15*, 3617–3624.

89. Perrier, D.L.; Rems, L.; Boukany, P.E. Lipid Vesicles in Pulsed Electric Fields: Fundamental Principles of the Membrane Response and Its Biomedical Applications. *Adv. Colloid Interface Sci.* **2017**, *249*, 248–271.

90. Yusupov, M.; Van der Paal, J.; Neyts, E.C.; Bogaerts, A. Synergistic Effect of Electric Field and Lipid Oxidation on the Permeability of Cell Membranes. *Biochim. Biophys. Acta-Gen. Subj.* **2017**, *1861*, 839–847.

91. Chang, C.-C.; Wu, M.; Yuan, F. Role of Specific Endocytic Pathways in Electrotransfection of Cells. *Mol. Ther.-Methods Clin. Dev.* **2014**, *1*, 14058.

92. Daud, A.I.; DeConti, R.C.; Andrews, S.; Urbas, P.; Riker, A.I.; Sondak, V.K.; Munster, P.N.; Sullivan, D.M.; Ugen, K.E.; Messina, J.L.; et al. Phase I Trial of Interleukin-12 Plasmid Electroporation in Patients With Metastatic Melanoma. *J. Clin. Oncol.* **2008**, *26*, 5896–5903.

93. Jensen, K.; Anderson, J.A.; Glass, E.J. Comparison of Small Interfering RNA (siRNA) Delivery into Bovine Monocyte-Derived Macrophages by Transfection and Electroporation. *Vet. Immunol. Immunopathol.* **2014**, *158*, 224–232.

94. Cristofolini, T.; Dalmina, M.; Sierra, J.A.; Silva, A.H.; Pasa, A.A.; Pittella, F.;

Creczynski-Pasa, T.B. Multifunctional Hybrid Nanoparticles as Magnetic Delivery Systems for siRNA Targeting the HER2 Gene in Breast Cancer Cells. *Mater. Sci. Eng. C* **2020**, *109*, 110555.

95. Qiu, Y.; Tong, S.; Zhang, L.; Sakurai, Y.; Myers, D.R.; Hong, L.; Lam, W.A.; Bao, G. Magnetic Forces Enable Controlled Drug Delivery by Disrupting Endothelial Cell-Cell Junctions. *Nat. Commun.* **2017**, *8*.15594.

96. Xiong, L.; Bi, J.; Tang, Y.; Qiao, S. Magnetic Core–Shell Silica Nanoparticles with Large Radial Mesopores for siRNA Delivery. *Small* **2016**, *12*, 4735–4742.

97. Kang, M.A.; Fang, J.; Paragodaarachchi, A.; Kodama, K.; Yakobashvili, D.; Ichiyanagi, Y.; Matsui, H. Magnetically Induced Brownian Motion of Iron Oxide Nanocages in Alternating Magnetic Fields and Their Application for Efficient siRNA Delivery. *Nano Lett.* **2022**, *22*, 8852–8859.

98. Yang, Y.; Gao, N.; Hu, Y.; Jia, C.; Chou, T.; Du, H.; Wang, H. Gold Nanoparticle-Enhanced Photodynamic Therapy: Effects of Surface Charge and Mitochondrial Targeting. *Ther. Deliv.* **2015**, *6*, 307–321.

99. Lächelt, U.; Kos, P.; Mickler, F.M.; Herrmann, A.; Salcher, E.E.; Rödl, W.; Badgujar, N.; Bräuchle, C.; Wagner, E. Fine-Tuning of Proton Sponges by Precise Diaminoethanes and Histidines in pDNA Polyplexes. *Nanomedicine Nanotechnology, Biol. Med.* **2014**, *10*, 35–44.

100. Kulkarni, J.A.; Darjuan, M.M.; Mercer, J.E.; Chen, S.; Van Der Meel, R.; Thewalt, J.L.; Tam, Y.Y.C.; Cullis, P.R. On the Formation and Morphology of Lipid Nanoparticles Containing Ionizable Cationic Lipids and siRNA. *ACS Nano* **2018**, *12*, 4787–4795.

101. Schaffert, D.; Badgujar, N.; Wagner, E. Novel Fmoc-Polyamino Acids for Solid-Phase Synthesis of Defined Polyamidoamines. *Org. Lett.* **2011**, *13*, 1586–1589.

102. Fröhlich, T.; Edinger, D.; Kläger, R.; Troiber, C.; Salcher, E.; Badgujar, N.; Martin, I.; Schaffert, D.; Cengizeroglu, A.; Hadwiger, P.; et al. Structure-Activity Relationships of siRNA Carriers Based on Sequence-Defined Oligo (Ethane Amino) Amides. *J. Control. Release* **2012**, *160*, 532–541.

103. Dohmen, C.; Edinger, D.; Fröhlich, T.; Schreiner, L.; Lächelt, U.; Troiber, C.; Rädler, J.; Hadwiger, P.; Vornlocher, H.P.; Wagner, E. Nanosized Multifunctional Polyplexes for Receptor-Mediated siRNA Delivery. *ACS Nano* **2012**, *6*, 5198–5208.

104. Lin, Y.; Wilk, U.; Pöhmerer, J.; Hörterer, E.; Höhn, M.; Luo, X.; Mai, H.; Wagner, E.; Lächelt, U. Folate Receptor-Mediated Delivery of Cas9 RNP for Enhanced Immune Checkpoint Disruption in Cancer Cells. *Small* **2023**, *19*, 2205318.

105. Rui, Y.; Wilson, D.R.; Tzeng, S.Y.; Yamagata, H.M.; Sudhakar, D.; Conge, M.; Berlinicke, C.A.; Zack, D.J.; Tuesca, A.; Green, J.J. High-Throughput and High-Content Bioassay Enables Tuning of Polyester Nanoparticles for Cellular Uptake, Endosomal Escape, and Systemic in Vivo Delivery of mRNA. *Sci. Adv.* **2022**, *8*, eabk2855.

106. Lin, Y.; Wilk, U.; Pöhmerer, J.; Hörterer, E.; Höhn, M.; Luo, X.; Mai, H.; Wagner, E.; Lächelt, U. Folate Receptor-Mediated Delivery of Cas9 RNP for Enhanced Immune Checkpoint Disruption in Cancer Cells. *Small* **2022**, 2205318.

107. Wang, F.; Zuroske, T.; Watts, J.K. RNA Therapeutics on the Rise. *Nat. Rev. Drug Discov.* **2020**, *19*, 441–442.

108. Akinc, A.; Maier, M.A.; Manoharan, M.; Fitzgerald, K.; Jayaraman, M.; Barros, S.; Ansell, S.; Du, X.; Hope, M.J.; Madden, T.D.; et al. The Onpattro Story and the Clinical Translation of Nanomedicines Containing Nucleic Acid-Based Drugs. *Nat. Nanotechnol.* **2019**, *14*, 1084–1087.

109. Teplensky, M.H.; Fantham, M.; Poudel, C.; Hockings, C.; Lu, M.; Guna, A.; Aragones-Anglada, M.; Moghadam, P.Z.; Li, P.; Farha, O.K.; et al. A Highly Porous Metal-Organic Framework System to Deliver Payloads for Gene Knockdown. *Chem* **2019**, *5*, 2926–2941.

110. Maugeri, M.; Nawaz, M.; Papadimitriou, A.; Angerfors, A.; Camponeschi, A.; Na, M.; Hölttä, M.; Skantze, P.; Johansson, S.; Sundqvist, M.; et al. Linkage between Endosomal Escape of LNP-mRNA and Loading into EVs for Transport to Other Cells. *Nat. Commun.* **2019**, *10*, 4333.

111. Zhang, T.; Guo, S.; Li, F.; Lan, X.; Jia, Y.; Zhang, J.; Huang, Y.; Liang, X.-J. Imaging-Guided/Improved Diseases Management for Immune-Strategies and Beyond. *Adv. Drug Deliv. Rev.* **2022**, *188*, 114446.

112. Kubiatowicz, L.J.; Mohapatra, A.; Krishnan, N.; Fang, R.H.; Zhang, L. mRNA Nanomedicine: Design and Recent Applications. *Exploration* **2022**, *2*, 20210217.

113. Zhang, F.; Liu, Y.; Lei, J.; Wang, S.; Ji, X.; Liu, H.; Yang, Q. Metal–Organic-Framework-Derived Carbon Nanostructures for Site-Specific Dual-Modality Photothermal/Photodynamic Thrombus Therapy. *Adv. Sci.* **2019**, *6*. 1901378.

114. Ruskowitz, E.R.; DeForest, C.A. Photoresponsive Biomaterials for Targeted Drug Delivery and 4D Cell Culture. *Nat. Rev. Mater.* **2018**, *3*, 17087.

115. Berg, K.; Folini, M.; Prasmickaite, L.; Selbo, P.; Bonsted, A.; Engesaeter, B.; Zaffaroni, N.; Weyergang, A.; Dietzea, A.; Maelandsmo, G.; et al. Photochemical Internalization: A New Tool for Drug Delivery. *Curr. Pharm. Biotechnol.* **2007**, *8*, 362–372.

116. Nomoto, T.; Fukushima, S.; Kumagai, M.; Machitani, K.; Arnida; Matsumoto, Y.; Oba, M.; Miyata, K.; Osada, K.; Nishiyama, N.; et al. Three-Layered Polyplex Micelle as a Multifunctional Nanocarrier Platform for Light-Induced Systemic Gene Transfer. *Nat. Commun.* **2014**, *5*, 3545.

117. Zhang, F.; Han, X.; Hu, Y.; Wang, S.; Liu, S.; Pan, X.; Wang, H.; Ma, J.; Wang, W.; Li, S.; et al. Interventional Photothermal Therapy Enhanced Brachytherapy: A New Strategy to Fight Deep Pancreatic Cancer. *Adv. Sci.* **2019**, *6*. 1801507.

118. Ding, J.; Lu, G.; Nie, W.; Huang, L.; Zhang, Y.; Fan, W.; Wu, G.; Liu, H.; Xie, H. Self-Activatable Photo-Extracellular Vesicle for Synergistic Trimodal Anticancer Therapy. *Adv. Mater.* **2021**, *33*, 2005562.

119. Hörner, M.; Jerez-Longres, C.; Hudek, A.; Hook, S.; Yousefi, O.S.; Schamel, W.W.A.; Hörner, C.; Zurbriggen, M.D.; Ye, H.; Wagner, H.J.; et al. Spatiotemporally Confined Red Light-Controlled Gene Delivery at Single-Cell Resolution Using Adeno-Associated Viral Vectors. *Sci. Adv.* **2021**, *7*, eabf0797.

120. Wu, M.; Wu, L.; Li, J.; Zhang, D.; Lan, S.; Zhang, X.; Lin, X.; Liu, G.; Liu, X.; Liu, J.

Self-Luminescing Theranostic Nanoreactors with Intraparticle Relayed Energy Transfer for Tumor Microenvironment Activated Imaging and Photodynamic Therapy. *Theranostics* **2019**, *9*, 20–33.

121. Jeon, J.; You, D.G.; Um, W.; Lee, J.; Kim, C.H.; Shin, S.; Kwon, S.; Park, J.H. Chemiluminescence Resonance Energy Transfer–Based Nanoparticles for Quantum Yield–Enhanced Cancer Phototheranostics. *Sci. Adv.* **2020**, *6*, eaaz8400.

122. Wu, W.; Mao, D.; Xu, S.; Kenry; Hu, F.; Li, X.; Kong, D.; Liu, B. Polymerization-Enhanced Photosensitization. *Chem* **2018**, *4*, 1937–1951.

123. Zheng, B.; Zhong, D.; Xie, T.; Zhou, J.; Li, W.; Ilyas, A.; Lu, Y.; Zhou, M.; Deng, R. Near-Infrared Photosensitization via Direct Triplet Energy Transfer from Lanthanide Nanoparticles. *Chem* **2021**, *7*, 1615–1625.

124. Jiang, L.; Bai, H.; Liu, L.; Lv, F.; Ren, X.; Wang, S. Luminescent, Oxygen-Supplying, Hemoglobin-Linked Conjugated Polymer Nanoparticles for Photodynamic Therapy. *Angew. Chem., Int. Ed.* **2019**, *58*, 10660–10665.

125. Valentine, M.T.; Fordyce, P.M.; Block, S.M. Eg5 Steps It Up! *Cell Div.* **2006**, *1*, 1–8.

126. Cheng, Q.; Wei, T.; Farbiak, L.; Johnson, L.T.; Dilliard, S.A.; Siegwart, D.J. Selective Organ Targeting (SORT) Nanoparticles for Tissue-Specific mRNA Delivery and CRISPR–Cas Gene Editing. *Nat. Nanotechnol.* **2020**, *15*, 313–320.

127. Miao, L.; Li, L.; Huang, Y.; Delcassian, D.; Chahal, J.; Han, J.; Shi, Y.; Sadtler, K.; Gao, W.; Lin, J.; et al. Delivery of mRNA Vaccines with Heterocyclic Lipids Increases Anti-Tumor Efficacy by STING-Mediated Immune Cell Activation. *Nat. Biotechnol.* **2019**, *37*, 1174–1185.

128. Du, F.; Liu, L.; Wu, Z.; Zhao, Z.; Geng, W.; Zhu, B.; Ma, T.; Xiang, X.; Ma, L.; Cheng, C.; et al. Pd-Single-Atom Coordinated Biocatalysts for Chem-/Sono-/Photo-Trimodal Tumor Therapies. *Adv. Mater.* **2021**, *33*, 2101095.

129. Yu, C.Y.Y.; Xu, H.; Ji, S.; Kwok, R.T.K.; Lam, J.W.Y.; Li, X.; Krishnan, S.; Ding, D.; Tang, B.Z. Mitochondrion-Anchoring Photosensitizer with Aggregation-Induced

Emission Characteristics Synergistically Boosts the Radiosensitivity of Cancer Cells to Ionizing Radiation. *Adv. Mater.* **2017**, *29*, 1606167.

130. Wu, F.; Chi, Y.; Jiang, Z.; Xu, Y.; Xie, L.; Huang, F.; Wan, D.; Ni, J.; Yuan, F.; Wu, X.; et al. Hydrogen Peroxide Sensor HPCA1 is an LRR Receptor Kinase in Arabidopsis. *Nature* **2020**, *578*, 577–581.

131. Lu, G.; Wang, X.; Li, F.; Wang, S.; Zhao, J.; Wang, J.; Liu, J.; Lyu, C.; Ye, P.; Tan, H.; et al. Engineered Biomimetic Nanoparticles Achieve Targeted Delivery and Efficient Metabolism-Based Synergistic Therapy against Glioblastoma. *Nat. Commun.* **2022**, *13*, 4214.

132. Maher, P.; Currais, A.; Schubert, D. Using the Oxytosis/Ferroptosis Pathway to Understand and Treat Age-Associated Neurodegenerative Diseases. *Cell Chem. Biol.* **2020**, *27*, 1456–1471.

133. Zhao, Q.; Liu, J.; Deng, H.; Ma, R.; Liao, J.-Y.; Liang, H.; Hu, J.; Li, J.; Guo, Z.; Cai, J.; et al. Targeting Mitochondria-Located CircRNA SCAR Alleviates NASH via Reducing MROS Output. *Cell* **2020**, *183*, 76–93.

134. Rennick, J.J.; Johnston, A.P.R.; Parton, R.G. Key Principles and Methods for Studying the Endocytosis of Biological and Nanoparticle Therapeutics. *Nat. Nanotechnol.* **2021**, *16*, 266–276.

135. Hatit, M.Z.C.; Lokugamage, M.P.; Dobrowolski, C.N.; Paunovska, K.; Ni, H.; Zhao, K.; Vanover, D.; Beyersdorf, J.; Peck, H.E.; Loughrey, D.; et al. Species-Dependent in Vivo mRNA Delivery and Cellular Responses to Nanoparticles. *Nat. Nanotechnol.* **2022**, *17*, 310–318.

136. Hu, B.; Kong, S.; Weng, Y.; Zhao, D.; Hussain, A.; Jiao, Q.; Zhan, S.; Qiu, L.; Lin, J.; Xie, M.; et al. Lipid-Conjugated siRNA Hitchhikes Endogenous Albumin for Tumor Immunotherapy. *Chinese Chem. Lett.* **2023**, *34*, 108210.

137. Abánades Lázaro, I.; Haddad, S.; Sacca, S.; Orellana-Tavra, C.; Fairen-Jimenez, D.; Forgan, R.S. Selective Surface PEGylation of UiO-66 Nanoparticles for Enhanced Stability, Cell Uptake, and pH-Responsive Drug Delivery. *Chem* **2017**, *2*, 561–578.

138. Xu, Y.; Li, C.; Lu, S.; Wang, Z.; Liu, S.; Yu, X.; Li, X.; Sun, Y. Construction of Emissive Ruthenium(II) Metallacycle over 1000 nm Wavelength for in Vivo Biomedical Applications. *Nat. Commun.* **2022**, *13*, 2009.

139. Smith, R.; Wafa, E.I.; Geary, S.M.; Ebeid, K.; Alhaj-Suliman, S.O.; Salem, A.K. Cationic Nanoparticles Enhance T Cell Tumor Infiltration and Antitumor Immune Responses to a Melanoma Vaccine. *Sci. Adv.* **2022**, *8*, eabk3150.

140. Truebenbach, I.; Zhang, W.; Wang, Y.; Kern, S.; Höhn, M.; Reinhard, S.; Gorges, J.; Kazmaier, U.; Wagner, E. Co-Delivery of Pretubulysin and siEG5 to EGFR Overexpressing Carcinoma Cells. *Int. J. Pharm.* **2019**, *569*, 118570.

141. Ni, H.; Hatit, M.Z.C.; Zhao, K.; Loughrey, D.; Lokugamage, M.P.; Peck, H.E.; Cid, A. Del; Muralidharan, A.; Kim, Y.; Santangelo, P.J.; et al. Piperazine-Derived Lipid Nanoparticles Deliver mRNA to Immune Cells in Vivo. *Nat. Commun.* **2022**, *13*, 4766.

142. Liu, S.; Cheng, Q.; Wei, T.; Yu, X.; Johnson, L.T.; Farbiak, L.; Siegwart, D.J. Membrane-Destabilizing Ionizable Phospholipids for Organ-Selective mRNA Delivery and CRISPR–Cas Gene Editing. *Nat. Mater.* **2021**, *20*, 701–710.

143. Dammes, N.; Goldsmith, M.; Ramishetti, S.; Dearling, J.L.J.; Veiga, N.; Packard, A.B.; Peer, D. Conformation-Sensitive Targeting of Lipid Nanoparticles for RNA Therapeutics. *Nat. Nanotechnol.* **2021**, *16*, 1030–1038.

144. Cullis, P.R.; Hope, M.J. Lipid Nanoparticle Systems for Enabling Gene Therapies. *Mol. Ther.* **2017**, *25*, 1467–1475.

145. Miao, L.; Zhang, Y.; Huang, L. mRNA Vaccine for Cancer Immunotherapy. *Mol. Cancer* **2021**, *20*, 41.

146. Riley, R.S.; Kashyap, M. V.; Billingsley, M.M.; White, B.; Alameh, M.-G.; Bose, S.K.; Zoltick, P.W.; Li, H.; Zhang, R.; Cheng, A.Y.; et al. Ionizable Lipid Nanoparticles for in Utero mRNA Delivery. *Sci. Adv.* **2021**, *7*, eaba1028.

147. Palanki, R.; Bose, S.K.; Dave, A.; White, B.M.; Berkowitz, C.; Luks, V.; Yaqoob, F.; Han, E.; Swingle, K.L.; Menon, P.; et al. Ionizable Lipid Nanoparticles for Therapeutic Base Editing of Congenital Brain Disease. *ACS Nano* **2023**, *17*,

13594–13610.

148. Li, B.; Jiang, A.Y.; Raji, I.; Atyeo, C.; Raimondo, T.M.; Gordon, A.G.R.; Rhym, L.H.; Samad, T.; MacIsaac, C.; Witten, J.; et al. Enhancing the Immunogenicity of Lipid-Nanoparticle mRNA Vaccines by Adjuvanting the Ionizable Lipid and the mRNA. *Nat. Biomed. Eng.* **2023**, doi:10.1038/s41551-023-01082-6.

149. Melamed, J.R.; Yerneni, S.S.; Arral, M.L.; LoPresti, S.T.; Chaudhary, N.; Sehrawat, A.; Muramatsu, H.; Alameh, M.-G.; Pardi, N.; Weissman, D.; et al. Ionizable Lipid Nanoparticles Deliver mRNA to Pancreatic β Cells via Macrophage-Mediated Gene Transfer. *Sci. Adv.* **2023**, *9*, eade1444.

150. Meulewaeter, S.; Nuytten, G.; Cheng, M.H.Y.; De Smedt, S.C.; Cullis, P.R.; De Beer, T.; Lentacker, I.; Verbeke, R. Continuous Freeze-Drying of Messenger RNA Lipid Nanoparticles Enables Storage at Higher Temperatures. *J. Controlled Release* **2023**, *357*, 149–160.

151. Hammel, M.; Fan, Y.; Sarode, A.; Byrnes, A.E.; Zang, N.; Kou, P.; Nagapudi, K.; Leung, D.; Hoogenraad, C.C.; Chen, T.; et al. Correlating the Structure and Gene Silencing Activity of Oligonucleotide-Loaded Lipid Nanoparticles Using Small-Angle X-Ray Scattering. *ACS Nano* **2023**, *17*, 11454–11465.

152. Schoenmaker, L.; Witzigmann, D.; Kulkarni, J.A.; Verbeke, R.; Kersten, G.; Jiskoot, W.; Crommelin, D.J.A. mRNA-Lipid Nanoparticle COVID-19 Vaccines: Structure and Stability. *Int. J. Pharm.* **2021**, *601*, 120586.

153. Blersch, J.; Francisco, V.; Rebelo, C.; Jiménez-Balsa, A.; Antunes, H.; Gonzato, C.; Pinto, S.; Simões, S.; Liedl, K.; Haupt, K.; et al. A Light-Triggerable Nanoparticle Library for the Controlled Release of Non-Coding RNAs. *Angew. Chem. Int. Ed.* **2020**, *59*, 1985–1991.

154. Dowdy, S.F. Endosomal Escape of RNA Therapeutics: How Do We Solve This Rate-Limiting Problem? *RNA* **2023**, *29*, 396–401.

155. Martens, T.F.; Remaut, K.; Demeester, J.; De Smedt, S.C.; Braeckmans, K. Intracellular Delivery of Nanomaterials: How to Catch Endosomal Escape in the Act. *Nano Today* **2014**, *9*, 344–364.

156. Vermeulen, L.M.P.; De Smedt, S.C.; Remaut, K.; Braeckmans, K. The Proton Sponge Hypothesis: Fable or Fact? *Eur. J. Pharm. Biopharm.* **2018**, *129*, 184–190.

157. Herrera-Barrera, M.; Ryals, R.C.; Gautam, M.; Jozic, A.; Landry, M.; Korzun, T.; Gupta, M.; Acosta, C.; Stoddard, J.; Reynaga, R.; et al. Peptide-Guided Lipid Nanoparticles Deliver mRNA to the Neural Retina of Rodents and Nonhuman Primates. *Sci. Adv.* **2023**, *9*, eadd4623.

158. Nakamura, T.; Nakade, T.; Yamada, K.; Sato, Y.; Harashima, H. The Hydrophobic Tail of a pH-Sensitive Cationic Lipid Influences siRNA Transfection Activity and Toxicity in Human NK Cell Lines. *Int. J. Pharm.* **2021**, *609*, 121140.

159. Winkeljann, B.; Keul, D.C.; Merkel, O.M. Engineering Poly- and Micelleplexes for Nucleic Acid Delivery–A Reflection on Their Endosomal Escape. *J. Control. Release* **2023**, *353*, 518–534.

160. Liu, S.; Wang, X.; Yu, X.; Cheng, Q.; Johnson, L.T.; Chatterjee, S.; Zhang, D.; Lee, S.M.; Sun, Y.; Lin, T.-C.; et al. Zwitterionic Phospholipidation of Cationic Polymers Facilitates Systemic mRNA Delivery to Spleen and Lymph Nodes. *J. Am. Chem. Soc.* **2021**, *143*, 21321–21330.

161. Klipp, A.; Burger, M.; Leroux, J.-C. Get out or Die Trying: Peptide- and Protein-Based Endosomal Escape of RNA Therapeutics. *Adv. Drug Deliv. Rev.* **2023**, *200*, 115047.

162. Zhang, X.; Zhao, W.; Nguyen, G.N.; Zhang, C.; Zeng, C.; Yan, J.; Du, S.; Hou, X.; Li, W.; Jiang, J.; et al. Functionalized Lipid-like Nanoparticles for in Vivo mRNA Delivery and Base Editing. *Sci. Adv.* **2020**, *6*, eabc2315.

163. Carrasco, M.J.; Alishetty, S.; Alameh, M.-G.; Said, H.; Wright, L.; Paige, M.; Soliman, O.; Weissman, D.; Cleveland, T.E.; Grishaev, A.; et al. Ionization and Structural Properties of mRNA Lipid Nanoparticles Influence Expression in Intramuscular and Intravascular Administration. *Commun. Biol.* **2021**, *4*, 956.

164. Ndeupen, S.; Qin, Z.; Jacobsen, S.; Bouteau, A.; Estanbouli, H.; Igyártó, B.Z. The mRNA-LNP Platform's Lipid Nanoparticle Component Used in Preclinical Vaccine

Studies Is Highly Inflammatory. *iScience* **2021**, *24*, 103479.

165. Li, Y.; Su, Z.; Zhao, W.; Zhang, X.; Momin, N.; Zhang, C.; Wittrup, K.D.; Dong, Y.; Irvine, D.J.; Weiss, R. Multifunctional Oncolytic Nanoparticles Deliver Self-Replicating IL-12 RNA to Eliminate Established Tumors and Prime Systemic Immunity. *Nat. Cancer* **2020**, *1*, 882–893.

166. Zhang, Q.; Kuang, G.; He, S.; Lu, H.; Cheng, Y.; Zhou, D.; Huang, Y. Photoactivatable Prodrug-Backboned Polymeric Nanoparticles for Efficient Light-Controlled Gene Delivery and Synergistic Treatment of Platinum-Resistant Ovarian Cancer. *Nano Lett.* **2020**, *20*, 3039–3049.

167. Rebelo, C.; Reis, T.; Guedes, J.; Saraiva, C.; Rodrigues, A.F.; Simões, S.; Bernardino, L.; Peça, J.; Pinho, S.L.C.; Ferreira, L. Efficient Spatially Targeted Gene Editing Using a Near-Infrared Activatable Protein-Conjugated Nanoparticle for Brain Applications. *Nat. Commun.* **2022**, *13*, 4135.

168. Chen, X.; Chen, Y.; Xin, H.; Wan, T.; Ping, Y. Near-Infrared Optogenetic Engineering of Photothermal NanoCRISPR for Programmable Genome Editing. *Proc. Natl. Acad. Sci.* **2020**, *117*, 2395–2405.

169. Chen, X.; Wang, S.; Chen, Y.; Xin, H.; Zhang, S.; Wu, D.; Xue, Y.; Zha, M.; Li, H.; Li, K.; et al. Non-Invasive Activation of Intratumoural Gene Editing for Improved Adoptive T-Cell Therapy in Solid Tumours. *Nat. Nanotechnol.* **2023**, *18*, 933–944.

170. Mo, Y.; Cheng, M.H.Y.; D'Elia, A.; Doran, K.; Ding, L.; Chen, J.; Cullis, P.R.; Zheng, G. Light-Activated siRNA Endosomal Release (LASER) by Porphyrin Lipid Nanoparticles. *ACS Nano* **2023**, *17*, 4688–4703.

171. Zhang, F.; Lin, Y.; Höhn, M.; Wagner, E. Chemical-Electron-Transfer-Based Lipopolyplexes for Enhanced siRNA Delivery. *Cell Reports Phys. Sci.* **2023**, *4*, 101444.

172. Stamenkovic, A.; Pierce, G.N.; Ravandi, A. Phospholipid Oxidation Products in Ferroptotic Myocardial Cell Death. *Am. J. Physiol. Circ. Physiol.* **2019**, *317*, H156–H163.

173. Li, W.; Zhang, X.; Zhang, C.; Yan, J.; Hou, X.; Du, S.; Zeng, C.; Zhao, W.; Deng,

B.; McComb, D.W.; et al. Biomimetic Nanoparticles Deliver mRNAs Encoding Costimulatory Receptors and Enhance T Cell Mediated Cancer Immunotherapy. *Nat. Commun.* **2021**, *12*, 7264.

174. Lee, K.; Conboy, M.; Park, H.M.; Jiang, F.; Kim, H.J.; Dewitt, M.A.; Mackley, V.A.; Chang, K.; Rao, A.; Skinner, C.; et al. Nanoparticle Delivery of Cas9 Ribonucleoprotein and Donor DNA in Vivo Induces Homology-Directed DNA Repair. *Nat. Biomed. Eng.* **2017**, *1*, 889–901.

175. Ulasov, A. V.; Rosenkranz, A.A.; Georgiev, G.P.; Sobolev, A.S. Nrf2/Keap1/ARE Signaling: Towards Specific Regulation. *Life Sci.* **2022**, *291*, 120111.

176. Vomund, S.; Schäfer, A.; Parnham, M.J.; Brüne, B.; Von Knethen, A. Nrf2, the Master Regulator of Anti-Oxidative Responses. *Int. J. Mol. Sci.* **2017**, *18*, 2772.

177. Li, R.; Jia, Z.; Zhu, H. Regulation of Nrf2 Signaling. *React. Oxyg. Species (Apex, N.C.)* **2019**, *8*, 312–322.

7 Publications

1. **Fengrong Zhang***, Yi Lin, Miriam Höhn, and Ernst Wagner*, Chemical-Electron-Transfer-Based Lipopolyplexes for Enhanced siRNA Delivery, *Cell Rep. Phys. Sci.*, **2023**. *4*, 101444.

2. **Fengrong Zhang**, Teoman Benli-Hoppe, Wei Guo, Johanna Seidl, Yi Wang. Rongqin Huang, and Ernst Wagner*, Receptor-Targeted Carbon Nanodot Delivery Through Polymer Caging and Click Chemistry-Supported LRP1 Ligand Attachment, *Polymers*, **2023**, *15*, 4039.

3. **Fengrong Zhang***, Tobias Burghardt, Miriam Höhn, and Ernst Wagner*. Dual Effect by Chemical Electron Transfer LNPs: ROS-Triggered Tumor Cell Killing Aggravated by Nrf2 Gene Silencing, *Pharmaceutics*, **2024**. *16*, 779.

8 Acknowledgements

Three years ago, I came to LMU filled with hope and curiosity, during my doctoral time, I have reaped a great harvest in both knowledge and friendship. Looking back on my doctoral life, many beautiful moments occurred, with occasional ups and downs, just like the ebb and flow of clouds.

I have been deeply influenced by the serious, innovative, and curious scientific sprits of Germany, which emphasize the importance of performance and efficacy, and encourage scientists to continuously pursue technological advancement. Moreover, in my spare time, I have experienced the customs of different cultural backgrounds.

Although it with great reluctance, it's time to part ways, as this is an inevitable truth of life. Herein, I would like to thank my doctoral supervisor Prof. Dr. Ernst Wagner, who gives me the opportunity to finish my PhD study. I greatly appreciate his professional suggestions.

I would like to express gratitude to my parents for bringing me to this beautiful world and for supporting and encouraging me to pursue scientific research. My brother, sister, my boyfriend, and other family members always accompany me in spirit.

I am thankful to Dr. Yi Lin, Dr. Teoman Benli-Hoppe, Tobias Burghardt, Wei Guo, Johanna Seidl, Paul Folda, Dr. Lun Peng, Dr. Franziska Haase, Mina Yazdi, Dr. Anna-Lina Lessl, and Wenshuai Li for practice support and helpful discussion about my projects, Wolfgang Rödl, Melinda Kiss, and Olga Brück for skillful assistance, and Miriam for instructions on cell culture and confocal laser scanning microscopy measurement. I would like to thank Susanne Kempter for TEM measurement and Melina Grau for performing matrix-assisted laser desorption ionization time-of-flight mass spectrometry measurement. Many thanks to my friends, Dr. Meng Lyu, Dr. Faqian Shen, Dr. Jie Luo, Dr. Hongchen Mai, Xianjin Luo, Ming Jiang, Jiayi Zhu, Yunhan Xie, Siyu Chen, Lukai Zhen, Jinke Tu, and others, for sharing moments of life with me. Specially gratitude to Johanna and Paul, my closest German friends, who kindly helped me all the time and took me to experience local life in Bavaria, and made me feel the sincere warmth in a foreign country.

Finally, thanks to the China Scholarship Council for supporting my study and life in Germany.

Science exploration is a long journey, the research is far from over, I am committed to continuing it until the end of my life.